Numerical Simulation of Self-Interacting Dark Matter Halos with central Black Holes

Masterarbeit

zur Erlangung des akademischen Grades
Master of Science (M.Sc.) in Physik
am Institut für Theoretische Physik (ITP)
der Goethe-Universität Frankfurt am Main

vorgelegt von Alexander Daniel Dreichner

Matrikelnr.: 6916884

Erstgutachterin: Prof. Dr. Laura Sagunski

Zweitgutachter: Prof. Dr. Jürgen Schaffner-Bielich

eingereicht am 17. Juli 2025

Selbstständigkeitserklärung

Hiermit erkläre ich, dass ich die Arbeit selbstständig und ohne Benutzung anderer als der angegebenen Quellen und Hilfsmittel verfasst habe. Alle Stellen der Arbeit, die wörtlich oder sinngemäß aus Veröffentlichungen oder aus anderen fremden Texten entnommen wurden, sind von mir als solche kenntlich gemacht worden. Ferner erkläre ich, dass die Arbeit nicht – auch nicht auszugsweise – für eine andere Prüfung verwendet wurde.

Frankfurt, den 17. Juli 2025

_____

Alexander Daniel Dreichner

Acknowledgment

First of all, I would like to thank Prof. Dr. Laura Sagunski for giving me the opportunity to immerse myself in current research on dark matter once again and for allowing me to fix the lingering issues from my bachelor's.
I am also grateful to Dr. Moritz Fischer, Prof. Dr. Rainer Spurzem, Prof. Dr. Hai-Bo Yu, and Dr. Yiming Zhong for their guidance during our meetings and for making time to meet even at very early or very late hours. I would like to thank Prof. Dr. Stuart Shapiro for sharing key insights into his approach. A big thank-you goes to the entire DMGW group for being such a welcoming and helpful team.
Special thanks to Matthias and Melanie for proofreading; without your help, this thesis would be riddled with errors and would likely be much harder to follow.
I gratefully acknowledge the support of the Deutschlandstipendium, which helped me to pursue my master's studies.
Finally, I want to thank my family, who made it possible for me to follow my passion for physics and complete my master's degree, and my girlfriend Leo, for your constant support and encouragement, and for keeping me grounded through the inevitable thesis chaos.

Zusammenfassung

In dieser Masterarbeit wird die Entwicklung eines selbst-wechselwirkenden dunkle Materie (SIDM) Halos um ein Schwarzes Loch (BH) mittels des *Gravothermal fluid* Modells numerisch untersucht.
Der Kern dieser Arbeit ist es, den *GravothermalSIDM* Code durch die Auswirkungen des BHs auf den Halo, insbesondere durch Akkretion, zu erweitern und die Entwicklung des Systems zum Gleichgewicht zu untersuchen. Während der Implementierung hat sich gezeigt, dass die Simulation empfindlich auf rein numerische Parameter reagiert. Diese Probleme wurden allerdings behoben und der richtige Steigungsindex wird im Gleichgewicht erreicht. Es wurden verschiedene Geschwindigkeitsabhängigkeiten des Selbstwechselwirkungsquerschnitts der Dunklen Materie (DM) untersucht.
Die Ergebnisse zeigen, dass das finale Dichteprofil unabhängig von den Anfangsbedingungen ist, sofern die Dichte bei großen Radien identisch ist. Ein Vergleich mit Dichteprofilen wo BH Effekte künstlich eingebaut wurden (dies ist eine übliche Näherung) zeigt eine gute Übereinstimmung mit der vollständigen Simulation. Auf Grundlage dieser Ergebnisse wird eine Änderung der Skalenhöhe um den Einflussradius des BH vorgeschlagen, um eine bessere Übereinstimmung mit reinen SIDM-Simulationen zu erreichen.
Der resultierende Code ist ein hilfreiches Werkzeug, um die dynamische Entwicklung von SIDM-Halos um BHs zu untersuchen.

Abstract

This thesis presents a numerical study of self-interacting dark matter (SIDM) halos containing a central black hole (BH), using the gravothermal fluid model. The work focuses on extending the GravothermalSIDM code by including accretion, in order to incorporate the effects of a central BH, and study the system's evolution toward equilibrium.
During the implementation, the simulation was found to be sensitive to numerical parameters, but these challenges were successfully addressed, and the correct slope index is recovered at equilibrium. Various velocity dependencies of the dark matter (DM) self-interaction cross-section were investigated.
The results show that the final density profile is independent of the initial conditions, provided the density is identical at large radii. A comparison with artificially spiked density profiles, commonly used as an approximation, shows good agreement with the full simulation. Based on these results, a modification of the scale height around the BH's radius of influence is proposed to improve a better agreement with SIDM-only simulations.
The resulting code provides a powerful tool for studying the dynamical evolution of SIDM halos with central BHs.

Contents

1. Introduction

To understand the nature of this work, a historical overview of the discovery of dark matter (DM) is given first. Fritz Zwicky, who called it *dunkle materie*, examined the Coma galaxy cluster in 1933 [1]. While doing so he noticed an irregularity - some galaxies were moving at speeds much larger than could be explained by the gravity of the visible objects. This led to four possibilities: either the system was not in equilibrium (i.e., it does not follow the expected relation between kinetic and potential energy), the observed velocities were changed due to redshift, these galaxies were not bound to the system or there exists some sort of matter that is not visible. The effects of the first two options were found to be not strong enough. Additionally, the third option was discarded, because it would imply that other galaxies moving at similar speeds should be observed in other systems, which is not the case. Hence, the conclusion was that additional mass is present in this system, surpassing the visible mass by a factor of 400. [1] However, this result was not left unquestioned with some scientists considering it "unlikely" (see [3] for a history in the discovery of DM).
Decades later, observations of the Andromeda galaxy showed further evidence for the presence of invisible matter. Rubin and Ford measured the orbital velocities of stars in the Andromeda galaxy and constructed so-called rotation curves that showed that the velocities increase in the inner regions, and then stay roughly constant throughout the halo [4]. In contrast to this, observations of visible mass show that it is concentrated in a central region, so that based on Kepler's law,

$$v = \sqrt{\frac{2GM(r)}{r}}, \tag{1}$$

for large radii, r, when the mass, M, is mostly constant, the velocity, v, should decrease as $1/r$. Thus, there are two options to explain the discrepancy with observations. Either the orbital dynamics is wrong, giving rise to theories of modified gravity, [2] or (and this is the widely accepted solution) the gravitational mass consists partly of some invisible matter that is not confined to the central region; DM.
Figure 1 shows the rotation curve of another galaxy (M33), along with the contributions of its individual components. The velocity increases with higher radii, and this phenomenon cannot be explained by the contributions from the stellar disk and gas alone [8]. Hence, the existence of DM is inferred, giving a major contribution to the matter in the system.
While many possible candidates for DM were proposed [3, 9], observations of the Bullet Cluster further supported the idea that DM consists of individual particles, as opposed to explaining the observed effects through a modification of gravity. [3] The Bullet cluster consists of two galaxy clusters that have collided. Figure 2 shows that the individual components of the system were separated in the collision and can be observed individually.

[1] A more recent study finds a slightly lower ratio, with 85% of the mass being in form of DM [2].
[2] These include *Modified Newtonian dynamics* which alters the gravitational force and can thereby explain galaxy rotation curves [5] but struggles to explain some phenomena on larger scales [6], as well as more complicated models [7].
[3] Nevertheless, as is frequently the case, divergent opinions are present as well [10].

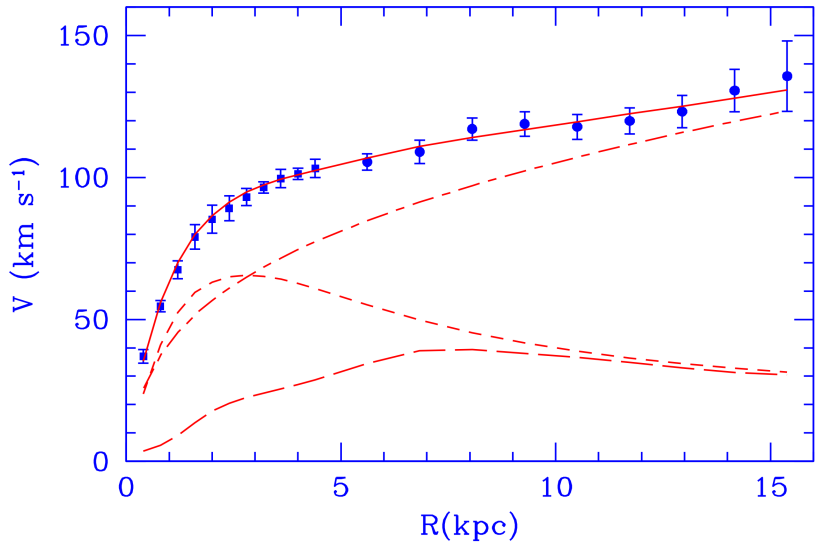

Figure 1: Galaxy rotation curve for M33 taken from [8]. Shown are the measured velocities (points), the best-fit model (solid), contributions from the stellar disk (short dashed), gas (long dashed) and DM (dashed-dotted).

The hot gas that was previously filling the space between galaxies in the cluster, was separated from the remaining cluster and remains close to the point of collision. This is because stars and galaxies can only interact very weakly through gravity, causing them to pass by each other during a collision without decelerating significantly. In contrast to this, the hot gas, consisting mostly of ionized hydrogen and helium, interacts electromagnetically (a strong force compared to gravity), thus scattering significantly during a collision and being slowed down. This separation of the collisional plasma and collisionless galaxies is consistent with observations [12]. Furthermore, Clowe et al. were also able to show that the center of mass of these galaxy clusters is separated from the dominant baryonic component, which is the plasma [12]. Gravitational lensing reveals instead, that the center of mass is close to the location of the galaxies, far from the point of collision. This leads to two conclusions: first, there is a significant amount of DM present in this system and second, DM must behave like (almost) collisionless particles.
Our current standard model of the universe, called ΛCDM, incorporates these findings. It assumes that on large scales *general relativity* (GR) is the correct theory to describe the universe, that the universe is flat on large scales, and that there are three main components of the universe: Dark Energy (Λ) that drives the current expansion of the universe, baryonic matter, [4] and finally cold *collisionless Dark Matter* (CDM) [13]. Here, *cold* refers to the fact that the movement of CDM is slow compared to the speed of light, and *dark* to the fact that it does not interact with photons and is thus not visible. While CDM (or DM in general) has not been directly observed yet, some constraints on its properties have still been found [9]. In addition to being cold, dark and collisionless, it is dissipationless, i.e.,

[4] In cosmology baryonic matter refers to everything that makes up stars, galaxies, etc., i.e., everything made from protons, neutrons and electrons.

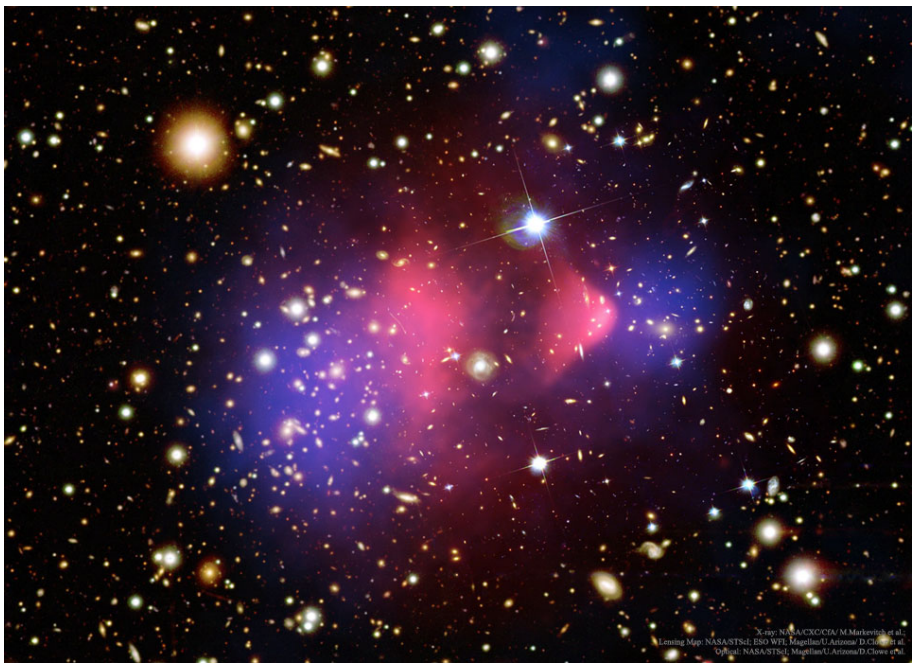

Figure 2: X-ray image of the Bullet cluster (pink, showing hot gas) superimposed over a visible light image (showing galaxies) [11]. The matter distribution obtained from gravitational lensing (blue) shows a need for the existence of CDM.

it cannot lose energy by emitting radiation. ΛCDM predicts that dark energy constitutes about 70% of the energy content of the universe, DM 25% and only the remaining 5% can be attributed to baryonic matter [14, 15].
Navarro, Frenk, and White studied the distribution of collisionless CDM in galaxies using N-body simulations [16]. They found that the resulting density profiles are well described by the NFW profile

$$\rho_{NFW} = \frac{\rho_s}{\frac{r}{r_s}\left(1+\frac{r}{r_s}\right)^2}, \tag{2}$$

with ρ_s and r_s being a characteristic density and radius. The DM contained in such a DM *halo* is distributed spherically symmetrical and results in a *cusp* with $\rho \propto 1/r$ for small radii.
Despite the fact that this DM model is successful at explaining the DM presence in galaxy clusters [17], central regions of dwarf galaxies favor shallower profiles with constant densities, called a *core* [18, 19]. This is known as the *core-cusp problem* and is illustrated in fig. 3. An examination of the rotation curve reveals that baryonic matter alone cannot fully explain the velocity distribution and the presence of DM is significant in explaining the data. However, while the NFW profile successfully predicts the observed velocities for radii larger than about 3kpc, for smaller radii the velocities are overestimated. The employment of a cored profile is able to solve this issue and better match observations.
For large distances to the center both profiles have a similar shape, while looking at the innermost region, the differences become evident: the NFW profile features a cusp and has a much higher central density in comparison to the cored profile.

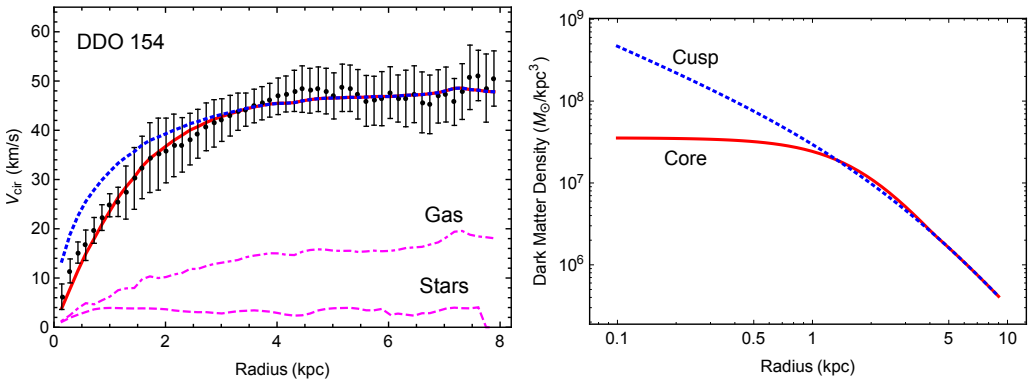

Figure 3: *Left:* Rotation curve of DDO 154. Observational data (black points) in comparison to models with a NFW profile (dotted blue) and a cored profile (red). Stellar and gas contributions are shown in pink. *Right:* DM densities corresponding to the fits. For the NFW profile, $r_s \approx 3.4$kpc and $\rho_s \approx 1.5 \cdot 10^7 \mathrm{M}_\odot/\mathrm{kpc}^3$. Reprinted from [9].

In addition to this, a multitude of other issues have surfaced with the assumptions underlying CDM [9]. For instance, the *diversity problem* demonstrates that the diversity exhibited by galaxies far exceeds what can be explained by the two halo parameters featured in the NFW profile. The *missing satellites problem* states that CDM halos should host a substantial number of subhalos, yet this is not observed. The *too big to fail* hypothesis suggests that the most massive subhalos appear to fail to host light-emitting objects. However, the opposite would be expected, as the mass of the DM halo should encourage gas clouds to collapse and form stars.
An elegant solution to this plethora of challenges is to allow for DM-DM self-interactions, thereby giving rise to a new model of DM: *Self-Interacting Dark Matter* (SIDM). These self-interactions, described by cross-section per unit mass σ/m, [5] cause particles to exchange energy and momentum, thereby "kicking" particles out from regions where the density is highest. Over time, this generally leads to a flattening of the inner region and the formation of a core, thus resolving these issues [9].
For SIDM halos with sufficiently high cross-sections a process can occur where the evolution of the halo is reverted resulting in a drastic increase of the central density and temperature [20]. This is known as the *gravothermal collapse* and is thought to be a possible candidate for the origin of SMBHs [21, 22].

Considering a wide range of astronomical objects (e.g., dwarf galaxies, galaxies, and galaxy clusters) allows to investigate the cross-section of SIDM in various environments. In light of the fact that the typical velocity of DM particles varies across these systems, [6] the possibility of a velocity-dependent cross-section is testable and has been observed in [23]; the cross-section varies from $2\mathrm{cm}^2/\mathrm{g}$ on galactic scales to $0.1\mathrm{cm}^2/\mathrm{g}$ on the scale of galaxy clusters. [7] This behavior is illustrated in fig. 4; for larger halo masses (larger velocities),

[5] For brevity, σ/m will hereafter be referred to simply as σ.
[6] The mean particle velocity of DM is higher in larger objects as can be seen in fig. 4.
[7] It appears that SIDM acts more similar to CDM on larger scales. A similar behavior is seen when

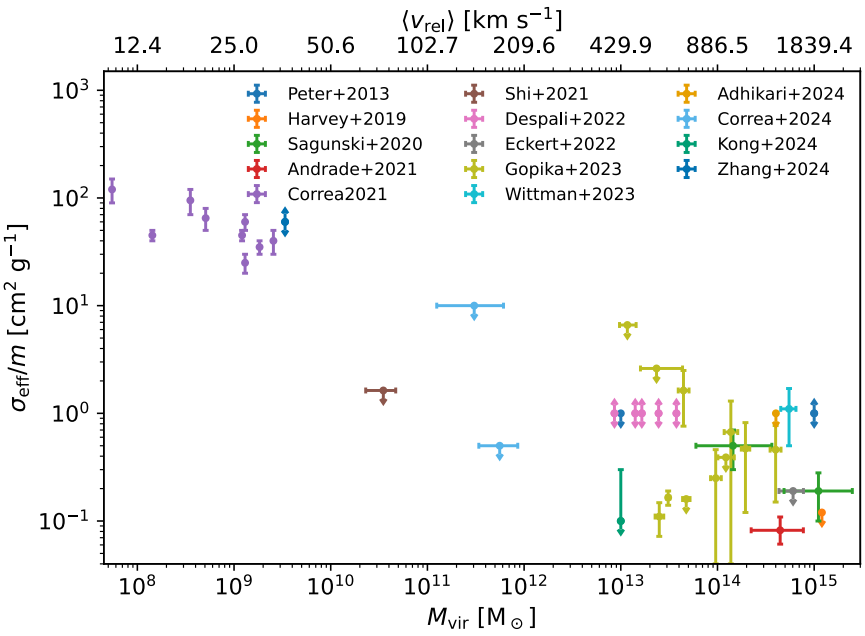

Figure 4: Constraints on the effective SIDM cross-section, shown as a function of system mass and relative velocity [24].

the effective cross-section is decreasing.

Most galaxies are thought to host supermassive BHs (SMBHs) at their centers [25, 26]. Therefore, the question arises as to how the presence of a central BH alters the DM density distribution. Gondolo and Silk investigated CDM distribution around such SMBHs and found that if SMBHs grow adiabatically, they transform the DM in their environment resulting in a stark increase of the density, so-called DM (density) *spikes* [27]. The relation between the initial density distribution and the final DM spike is given by

$$\rho_{DM} \propto r^{-\alpha_{sp}}, \qquad \alpha_{sp} = \frac{9-2\alpha}{4-\alpha}, \tag{3}$$

where the density distribution of the isolated CDM halo scales with $r^{-\alpha}$. Hence, an overall increase of the central density is expected. A NFW halo ($\alpha = 1$) is thus be expected to have $\alpha_{sp} = 7/3$ near a BH.
In contrast to CDM halos, SIDM halos undergo some sort of evolution, and their density is subject to a constant change. Hence, the relation between the spike index of the density (α_{sp}) in the vicinity of a BH does not follow the simple relation that was derived for CDM. Instead, equilibrium solutions can be found when there is a constant flux of matter onto the BH [28]. The final α_{sp} then depends on the underlying particle model (see section 2.7). For the choice of $\sigma \propto v^{-4}$, commonly found in the literature [28–30], the resulting density is expected to scale with $r^{-7/4}$ - shallower than for $\alpha_{sp} = 7/3$ in the CDM case.

looking at rotation curves; for large radii, the SIDM and CDM density profiles show similar behavior.

To numerically simulate SIDM halos, two major approaches are commonly used: **N-body simulations** model dark matter as a collection of discrete particles (typically $N > 10^5$), where the gravitational interactions between particles are calculated directly. For SIDM, self-interactions are usually accounted for via Monte Carlo scattering methods that stochastically model collisions [29]. While this approach resolves single particle interactions and is widely used, it is computationally expensive due to the large number of particles and interaction calculations involved.
An alternative approach treats DM as a **collisional fluid** [20–22], described by continuous fields. [8] In this framework, the evolution of the system is governed by hydrodynamic equations, typically derived from the Boltzmann equation under certain assumptions [28]. This method allows for faster simulations and allows the exploration of a wide range of interaction models and parameter spaces.
However, fluid models involve simplifying assumptions (e.g., thermal equilibrium, isotropy) and often require calibration against N-body simulations to ensure accuracy [20]. [9]

The aim of this thesis is to examine the evolution of SIDM halos containing central BHs, using a fluid model approach. The primary objective is to observe the convergence of the spike index to the expected equilibrium solutions. Additionally, simulations with a central BH are compared to SIDM-only simulations to study the influence of the BH on the halo's evolution. The final goal is to explore how the impact of BHs can be incorporated into the results of SIDM-only simulations.
The thesis is structured as follows. First, the theoretical framework for modeling SIDM halo evolution is introduced in section 2.1, followed by a brief overview of the typical evolution of a SIDM-only halo in section 2.2. Additional relevant physical concepts and quantities, such as spike index, spike radius, accretion and the cross-section, are then discussed in sections 2.3 to 2.6. In section 2.7, the equilibrium solutions for the DM density profiles are derived. After this, the general numerical approach for solving the equations governing the evolution is described in section 3, along with the specific modifications central to this work that are necessary to include a central BH (sections 3.2 and 3.3) Finally, the results of the simulations are presented and discussed in section 4.

Throughout this work, I use the first-person form ("I") to distinguish my own contributions from established theory or concepts taken from the literature.

[8] In a particle based model, each particle i has a position $\vec{r}_i$, velocity $\vec{v}_i$ and other properties. In contrast, fluid models describe macroscopic quantities like density $\rho(\vec{r})$ and corresponding fluid velocity $\vec{v}(\vec{r})$.
[9] E.g. the "C" in eq. (11) is such a calibration parameter.

2. Theory

This section provides the theoretical foundation necessary to understand the physics relevant to this study. The first part introduces the *gravothermal fluid model* [31], which is the basis to describe the evolution of SIDM halos. This is followed by definitions of specific physical quantities relevant to the analysis, such as the spike radius and spike index, the self-interaction cross-section, and the treatment of accretion onto a central BH. In the last part of the section, equilibrium solutions in different regimes are derived, which serve as benchmarks for comparison with the results of numerical simulations presented later.

2.1. Gravothermal fluid

To model the DM halo surrounding a massive BH the *gravothermal fluid model* first developed by Lynden-Bell and Eggleton in 1980 is used. Originally, it was introduced to study the dynamics in globular clusters, in particular the evolution of their core density. However, this model can also be applied to SIDM halos [21].
In the gravothermal fluid model the DM halo is described as a fluid of particles that can thermally interact with a certain self-interaction cross section and thus exchange heat.
To reduce the number of independent variables and connect the properties of the DM particles, the equation of state of an ideal gas is defined as

$$pV = Nk_bT. \tag{4}$$

This relates the pressure of the fluid, p, its volume, V, the number of particles, N, Boltzmann's constant, k_b and the temperature, T. Additionally, an internal energy per particle mass, m, is defined as

$$u = \frac{3}{2m}k_bT = \frac{1}{2}\vec{v}^2 = \frac{3}{2}\nu^2, \tag{5}$$

where in the last step the the one-dimensional velocity dispersion ν is introduced as

$$\nu^2 \equiv \langle v_x^2\rangle = \langle v_y^2\rangle = \langle v_z^2\rangle = \frac{1}{3}\langle\vec{v}^2\rangle. \tag{6}$$

For the sake of brevity, I might also simply refer to ν as the velocity and to u as the energy.

In the following, the equations used are only described very briefly. A more detailed treatment of these can be found in [22, 32].
After applying spherical symmetry, the problem effectively reduces to one spatial dimension. This assumption is physically motivated, as SIDM halos tend to lose their ellipticity quickly due to self-interactions [9].

Conservation of mass: The differential equation for the mass of a spherical DM halo can be written as:

$$\frac{\partial M}{\partial r} = 4\pi\rho r^2. \tag{7}$$

Here, M is the halo mass, r the radius and ρ the DM density.

Hydrostatic equilibrium: Hydrostatic equilibrium is assumed with no net flow of particles so that for a Newtonian potential one can derive the condition on the gradient of the pressure, p,

$$\frac{\partial p}{\partial r} = -\frac{GM\rho}{r^2}, \tag{8}$$

with G denoting Newton's gravitational constant [22].

Heat conduction: The luminosity, L, describes how the heat in the DM halo is flowing, i.e., how a gradient of the temperature of the DM particles changes their internal energy. To derive an expression for the luminosity, a particle flux, $n\lambda/\tau$ causing the flow of energy through a surface is considered. In terms of the mean free path, λ, and the time between collisions, τ, the luminosity is then given by:

$$L = -4\pi r^2 \frac{3\rho\lambda^2 b}{2\tau}\frac{\partial \nu^2}{\partial r}, \tag{9}$$

where $b \approx 1.385$ is an effective impact parameter [20].
For the mean free path two regimes are considered, depending on its relation to the gravitational scale height, H, also called Jeans length, r_J [33]:

$$H = \sqrt{\frac{\nu^2}{4\pi G\rho}}. \tag{10}$$

In the short mean free path (**SMFP**) limit, it is assumed that the mean free path is much smaller than the gravitational scale height $\lambda \ll H$. In this case ordinary particle scattering can be assumed with the mean free path being $\lambda = 1/\rho\sigma$ [10] and the time between interactions simply being the mean free path over the velocity, $\tau = \lambda/\nu$. Here, a cross-section per unit mass σ was defined that serves to model different particle interactions.
If on the other hand, $\lambda \gg H$, then the long mean free path (**LMFP**) limit is considered [34]. The mean free path then becomes comparable to the gravitational scale height $\lambda \to H$ and the time between interactions becomes the relaxation time $\tau = 1/a\sigma\rho\nu$ with $a \approx 2.257$ [22]. Finally, to get a limiting behavior in either case, the luminosity is written in the following way:

$$\frac{L}{4\pi r^2} = -\frac{3\rho b\nu}{2}\left[\rho\sigma + \frac{b}{a\rho\sigma C H^2}\right]^{-1}\frac{\partial \nu^2}{\partial r}. \tag{11}$$

Hence, the first term in the bracket stems from the expression in the SMFP and the second one from the LMFP and $C \approx 0.75$ is a calibration constant between the two regimes [20, 22, 35].

Laws of Thermodynamics: From the Second Law of Thermodynamics, an equation can be derived that governs the time evolution of the DM halo. The entropy per unit mass,

[10] $\rho\sigma\lambda$ gives the average number of hits a particle is expected to make when traveling a length λ through a medium with density ρ and with cross-section per unit mass σ. Hence, when one scattering occurs the mean free path is $\lambda = 1/\rho\sigma$.

$s = \ln\left(v^3/\rho\right)$, is introduced that causes the halo to evolve:

$$\frac{\partial L}{\partial r} = -4\pi\rho r^2 v^2 \left(\frac{\partial}{\partial t}\ln\left(\frac{v^3}{\rho}\right)\right)_M . \tag{12}$$

The subscript M on the bracket indicates that the mass is kept constant when taking the time derivative.

Addition of BH effects: In order to simulate a SIDM halo surrounding a central BH, the influence of the BH on the halo has to be considered.
The BH is taken to be a point mass with mass M_{bh} situated at the center of the halo. This leads to two changes in the equations discussed above. First, eq. (8) gains an additional mass term:

$$\frac{\partial p}{\partial r} = -G\rho\frac{M + M_{bh}}{r^2}. \tag{13}$$

With the BH at the center of the halo, the inner regions are dominated by the pull of the BH and not the enclosed DM mass. Consequently, for sufficiently small radii, the DM mass can be neglected and the scaling of the pressure analytically derived (eq. (15)). Additionally, instead of the Jeans length r_J, the gravitational scale height H is now determined by the position r following the work in [28]. Hence, H is taken to be

$$H = \min(r, r_J). \tag{14}$$

This modifies the scale height in the heat conduction (eq. (11)) in the LMFP regime.

2.2. Evolution of SIDM halos

In this section, it is assumed that the halo initially follows a NFW profile and is then left to evolve.
Considering a SIDM halo without a central BH first, the evolution is characterized by three distinct phases, illustrated by fig. 5:
Initially (at $t = 0$), the internal energy decreases toward the center, resulting in a negative luminosity. This corresponds to an outflow of matter from the central region. During this stage, the density in the inner region of the halo gradually relaxes and forms a flat profile, called a *core* (seen in fig. 5b at $t = 1.9 \cdot 10^{-4}$Gyr). The internal energy at the center continuously increases over time, while the outer halo remains largely unaffected.
In the intermediate phase, the central internal energy continues to rise until it eventually levels off, forming a constant plateau (seen at $t = 3.5 \cdot 10^{-2}$Gyr in fig. 5a). Because of this, at this stage the inner region of the density profile is also referred to as *isothermal* core. As a result, the luminosity approaches zero in the central region and the matter outflow halts. When this happens, the central density stabilizes temporarily.
Finally, in the *gravothermal collapse* phase (for $t \geq 1.4 \cdot 10^{-1}$Gyr), the direction of energy and mass flow reverses. The internal energy continues to increase at the center, but now the luminosity is positive throughout the whole halo (fig. 5c) causing mass to flow inwards. The central density and temperature begin to rise rapidly, reaching increasing large values.

With the introduction of a BH into the system, the evolution described here is altered. By looking at eq. (13) and considering the inner region where the BH dominates it becomes evident that close to the BH $M_{bh} \gg M$, so that $M + M_{bh} \approx M_{bh} = \text{const}$. Additionally assuming a power-law ansatz with $\rho \propto r^{-\alpha}$, this yields:

$$\begin{aligned} p = \rho v^2 &= \int -\rho \frac{M_{bh}}{r^2} \mathrm{dr} = \int -r^{-\alpha} \frac{M_{bh}}{r^2} \mathrm{dr} \\ &= \frac{1}{1+\alpha} r^{-\alpha-1} M_{bh} \\ \Rightarrow v^2 &= \frac{1}{1+\alpha} \frac{M_{bh}}{r} \propto r^{-1}. \end{aligned} \tag{15}$$

Hence, the internal energy shows an increase towards the center and the luminosity is positive, leading to the expectation that matter flows inwards instantaneously. This gives rise to the need of modeling *accretion* when the particles reach the BH at the center.
The further evolution of the halo is more complicated to predict and is the goal of this work.

2.3. Spike radius

Since the mass of a BH in the simulations is surpassed by the total DM halo mass by many orders of magnitude,[11] the evolution in the outer parts of the halo is expected to continue unaltered when a central BH is introduced.
The area of the halo influenced by the inclusion of a central BH can be described by introducing the radius of influence of the BH, r_h. Similarly, the transition from the power-law solutions of the DM spikes in the inner regions to the shallower power-law solutions (or cores) further outside is described by a transition radius, also known as the spike radius, r_{sp}.
A commonly used definition for the former is based on the work in [37] where the effects of adiabatic BH growth on CDM halos were studied. It was found that the radius of influence, $r_{h,m}$,[12] can be defined in terms of the BH mass, M_{bh}:

$$M\left(r < r_{h,m}\right) = 4\pi \int_0^{r_{h,m}} \rho r^2 dr \stackrel{!}{=} 2M_{bh}. \tag{16}$$

Using this, the spike radius is directly related to the radius of influence:

$$r_{sp} \approx 0.2 r_{h,m}. \tag{17}$$

However, this relation between r_{sp} and $r_{h,m}$ is specific to CDM halos. For SIDM, self-interactions modify the inner density profile and shift the location of the transition region, rendering this definition inaccurate (see my results in section 4.5). An alternative definition,

[11] Observations indicate a correlation between the mass of the central BH and the surrounding DM halo. Typically, the BH mass is about five orders of magnitude smaller than the halo mass [36].
[12] The subscript m indicates that this expression for the radius of influence is defined in term of mass.

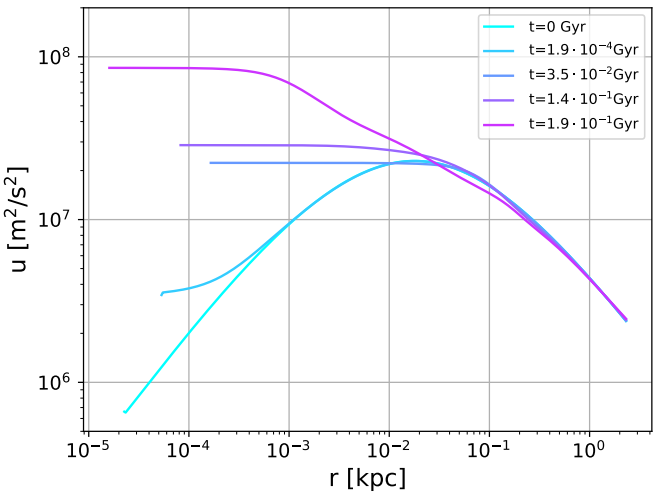

(a) Internal energy as a function of radius.

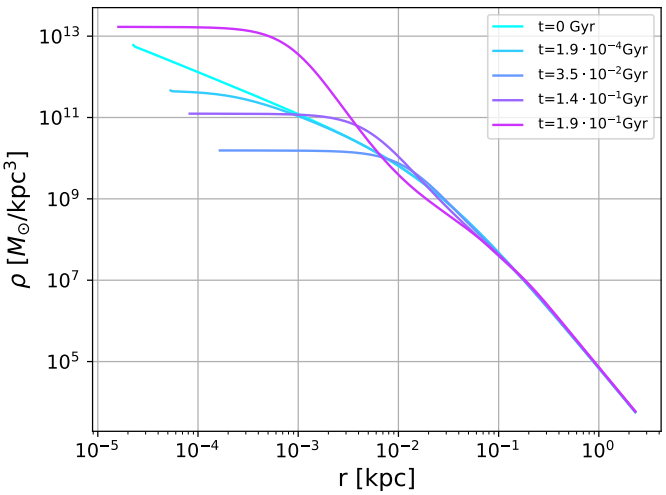

(b) Density as a function of radius.

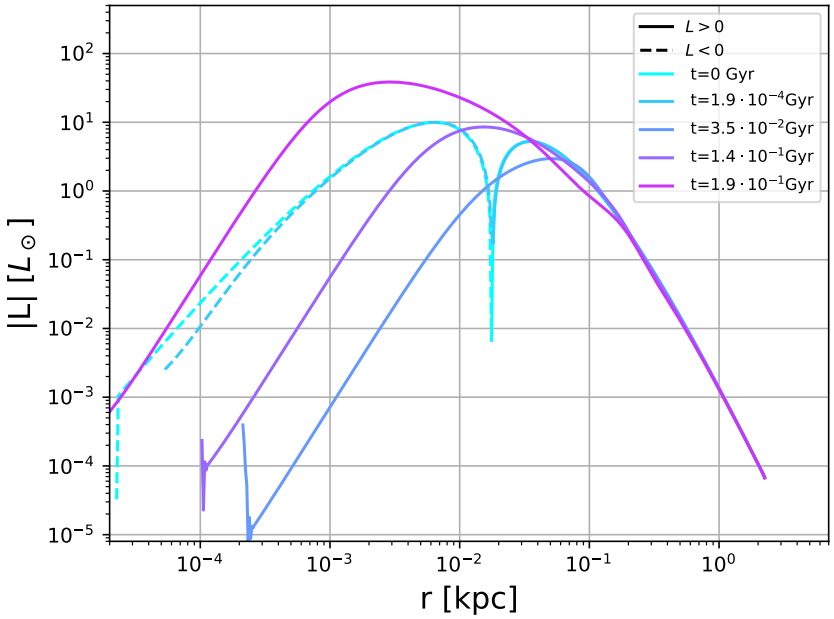

(c) Luminosity as a function of radius. Negative luminosity is shown in dashed lines, positive in solid. Some numerical artifacts are visible for the smallest radii.

Figure 5: SIDM halo evolution with $r_s = 23.1\text{pc}$, $\rho_s = 5.615\text{M}_\odot/\text{pc}^3$ and $\sigma = 100\text{cm}^2/\text{g}$. Initially a NFW profile is present ($t = 0$). As time progresses and central energy increases, first a core forms ($t = 1.9 \cdot 10^{-4}\text{Gyr}$). Once the energy is constant throughout the whole center and the luminosity is strictly positive ($t = 3.5 \cdot 10^{-2}\text{Gyr}$), an isothermal core forms. The evolution then reverses and the density increases again to much higher values during the gravothermal collapse ($t = 1.4 \cdot 10^{-1}\text{Gyr}$ and $t = 1.9 \cdot 10^{-1}\text{Gyr}$).

which I find to be more suitable for SIDM, is also proposed i n[37]. [13] Here, the radius of influence, $r_{h,v}$, is defined in terms the velocity, such that

$$v^2(r_{h,v}) = \frac{GM_{bh}}{r_{h,v}}. \tag{18}$$

This places it such that the velocity dispersion of the DM particles is dominated by the BH potential, i.e., the particle's orbit is defined by the mass of the BH and not the enclosed mass of the DM halo.
For an isothermal core, seen for example in the later phase of SIDM-only halo evolution and also expected outside the radius of influence of a central BH, the velocity dispersion is mostly independent of the radius, so that the above definition results in

$$r_{h,v} = \frac{GM_{bh}}{v_0^2} \tag{19}$$

when taking v_0 outside the radius of influence but within core.
As is shown in section 4.5, this definition better captures the evolution of the transition region when the spike radius is set to be $r_{sp} \approx r_{h,v}$.
In practice, differences between SIDM halos with and without a central BH are expected to appear only at radii $r \lesssim r_{sp}$, while the outer regions remain largely unaffected.

2.4. Spike index

The spike index, α, is used to describe a power-law distribution of DM density. By definition, it is the slope of the logarithmic density:

$$\alpha = -\frac{d\ln\rho}{d\ln r} \tag{20}$$

Thus, if $\rho \propto r^{-\alpha}$ the spike index is simply the exponent α.
Certain values of α are of particular physical meaning. For example, the NFW profile features $\alpha = 1$ at the center and $\alpha = 3$ for large radii. As the halo evolves and a core forms, the slope decreases and reaches $\alpha \approx 0$ in the central region. In halos hosting a central BH, DM tends to form a steeper profile at the center compared to DM-only halos. CDM spikes around central BHs are characterized by a spike index $\alpha = 7/3$ when the halo is in equilibrium [27]. With the introduction of DM self-interactions, the spike index is generally altered. The precise solution at equilibrium depends on the model of the heat conduction and DM self-interaction cross-section. Further details are discussed in section 2.7. A commonly cited value for the spike index is $\alpha = 7/4$, a value which is derived from the cross-section for a Coulomb-like interaction given by $\sigma \propto v^{-4}$ [28].

[13] Note that although Merritt presents both definitions, the author ultimately favors the mass-based version ($r_{h,m}$) due to its simpler computation.

2.5. Accretion onto a Black Hole

To understand accretion onto a BH, it is useful to start with the Schwarzschild metric, which describes the spacetime around a spherically symmetric, non-rotating, and uncharged BH:

$$ds^2 = -\left(1 - \frac{2GM}{rc^2}\right)dt^2 + \left(1 - \frac{2GM}{rc^2}\right)^{-1}dr^2 + r^2 d\Omega^2, \tag{21}$$

where G denotes Newton's constant, M is the mass of the BH, c the speed of light, and $d\Omega^2$ the angular part of the metric.
The *Schwarzschild radius*, $r = 2GM/c^2$, marks the outer location at which the metric diverges. This defines the *event horizon*; a region from which no information or particle can escape. Any particle crossing this radius is inevitably accreted by the BH [38].
However, the BH alters trajectories well beyond the event horizon. For massive particles on circular orbits, there exists an *innermost stable circular orbit* (ISCO) at $r_{ISCO} = 6GM/c^2$. Inside this region, circular orbits become unstable.
However, for particles on unstable circular or more general orbits a boundary between the Schwarzschild radius and the ISCO exists. The *marginally bound orbit* at $r = 4GM/c^2$ marks the smallest radius at which a particle with zero velocity at infinity can still escape [38]. This effectively sets the limit of how close to BHs bound massive particles can orbit without being captured.
It has been shown that in a Schwarzschild spacetime, the DM density profile vanishes at this radius [39], which motivates its use in the modeling of BH accretion within DM halos [28, 40].

2.6. Particle cross-section

The particle cross-section quantifies the probability of a specific interaction occurring between two particles.
The perhaps most intuitive example is the collision of two hard, inelastic spheres - such as two billiard balls of radius R. In this case, the cross-section has a very intuitive geometric interpretation; a collision occurs if the separation between the center of both spheres is less than $2R$, yielding a cross-sectional area of

$$\sigma = \pi \left(2R\right)^2, \tag{22}$$

corresponding to the cross-section for this interaction.
More generally, the cross-section is not necessarily related to the physical size of a particle. Instead, it can be larger if there is a force acting between the colliding particles and depend on various different experimental parameters. A classical example of this is the Rutherford cross-section, which describes the angular distribution of a charged point particle being deflected at an angle θ when colliding with another charged point particle,

$$\frac{d\sigma}{d\Omega} = \left(\frac{qQ}{16\pi\varepsilon_0 E \sin^2\left(\theta/2\right)}\right)^2, \tag{23}$$

where q and Q describe the two charges, E is the energy of the incident particle in the center of mass frame and $\frac{d\sigma}{d\Omega}$ is the differential cross-section for this interaction. The total cross-section can then be recovered by integrating over the full solid angle $d\Omega$: [14]

$$\sigma = \int \frac{d\sigma}{d\Omega} d\Omega. \tag{24}$$

It is important to note, that when the Rutherford cross-section is being used this expression diverges for small angles.
To draw the line back to the simulation of DM halos, it should be recalled that with the fluid model used in this work and with spherical symmetry assumed, the particles are not modeled individually. Instead, the fluid elements are only described by their radial position. Consequently, the total cross-section is used for two main reasons.
First, from a practical standpoint, incorporating angle-dependent scattering (such as in eq. (23)) is impractical with a one-dimensional fluid, given that there is only one variable describing the position of fluid elements. Some N-body simulations address this issue by sampling the scattering angle for each particle [41]. However, this approach requires a large number of particles and samples to reduce statistical noise, which significantly increases the computational cost.
Second, the aim of this work is to study the macroscopic effects of self-interactions, rather than to simulate the detailed particle physics. While the microphysics is important because it determines the scattering rate, for the current purposes the total cross-section is sufficient to capture the relevant behavior.

Some constraints on the cross-section of DM have already been obtained. Observations of the Bullet cluster with gravitational lensing have revealed a separation of the collisional and collisionless components, indicating that DM is positioned with effectively collisionless galaxies. [42] showed that using this data, the cross-section is constrained by $\sigma < 1.25\text{cm}^2/\text{g}$ for a DM with a constant cross-section.[15]
Furthermore, observational data suggest that the cross-section of DM particles may depend on the relative velocity of the interacting particles (fig. 4). A common approach is to model the cross-section as a power-law in the velocity dispersion [40],

$$\sigma = \sigma_0 \left(v/v_0\right)^{-\beta}, \tag{25}$$

where σ_0 is a characteristic cross-section at a reference velocity v_0 and β describes velocity-dependence. This provides a useful approximation in the limit of low and high velocity, despite the fact that the underlying particle models generally predict behaviors that are more complicated; often a constant cross-section at low velocities and a decreasing one at high velocities [45].

[14] Alternative definitions exist in which the differential cross-section is weighted by angular factors. For example, including a factor of $(1 - \cos\theta)$ yields the transfer cross-section, which emphasizes particles that have lost their forward momentum. Similarly, a weighting of $(1 - \cos^2\theta)$ gives the viscosity cross-section, which places greater emphasis on perpendicular scatterings [9].

[15] For comparison, typical cross-sections for baryonic reactions can be much larger, e.g., $\sigma \geq 10^8\text{cm}^2/\text{g}$ for electron scattering in plasma [43], while the collision of two Milky-way-like galaxies results in a much smaller geometric cross-section of $\sigma \approx 10\text{cm}^2/\text{g}$ [44].

The simple example from eq. (22) then reduces to setting $\beta = 0$, while the more complicated Rutherford cross-section is equivalent to $\beta = 4$ after integrating eq. (23). [16] While the particle physics of DM is still unknown, proposed models feature a relation $\sigma \propto 1/v^4$ for large v motivated by a "dark" photon exchange [46, 47].

2.7. Equilibrium solutions

It is thought that permitting a halo to evolve for a sufficiently large time, allows it to settle in an equilibrium. In this work, I am particularly interested in correctly determining such equilibrium solutions. A precise prediction of these will help to determine the structure of present-day DM halos.
The derivation of these steady-state solutions presented in this work is based on the arguments presented in [40].

To derive the equilibrium solutions it is necessary to consider eq. (12). Here, one can immediately see that the halo does not change if $\frac{\partial L}{\partial r} = 0$ since in this case $\frac{\partial s}{\partial t} = 0$. To determine when the luminosity becomes constant eq. (11) is rewritten in the slightly more convenient form:

$$L = -4\pi r^2 \frac{3\rho b \nu}{2} \left[\rho\sigma + \frac{b}{a\rho\sigma C H^2} \right]^{-1} \frac{\partial \nu^2}{\partial r}. \tag{26}$$

As was shown in eq. (15), ν^2 scales like r^{-1} close to the BH. Thus, the trivial solution to $L = \text{const}$, $\frac{\partial \nu^2}{\partial r} = 0 = \frac{\partial T}{\partial r}$, can be immediately ruled out and it can be concluded that the equilibrium of the halo solution is not due to a thermal equilibrium.
Instead, the equilibrium arises when the luminosity is constant but non-zero; that is when the energy flux, which in turn is supported by a matter flux, remains constant. In this case, the term in the brackets of eq. (26) can now be examined, allowing three scenarios to be determined; the halo can be in the LMFP, the SMFP regime, or in a combination of both.
In the following, a power-law solution for ρ and for the velocity dependence of the cross-section $\sigma \propto \nu^{-\beta}$ is assumed. Furthermore, since the part of the halo close to the BH is considered, $H^2 \propto r^2$ and $\nu \propto r^{-1/2}$.

2.7.1. Equilibrium in LMFP

In the LMFP regime, only the right term in the bracket of eq. (26) is relevant, giving

$$L = -4\pi r^2 \frac{3\rho\nu}{2} a\rho\sigma C H^2 \frac{\partial \nu^2}{\partial r} \propto r^2 \rho^2 \nu \sigma H^2 \frac{\partial \nu^2}{\partial r}. \tag{27}$$

[16] $E \propto v^2$ so that $1/E^2 \propto 1/v^4$.

Collecting everything gives:

$$\begin{aligned} L &\propto r^2 r^{-2\alpha} r^{-1/2} r^{\beta/2} r^2 r^{-2} = r^{3/2-2\alpha+\beta/2} \stackrel{!}{=} \text{const} \\ &\Leftrightarrow 3/2 - 2\alpha + \beta/2 = 0 \Leftrightarrow \alpha = \frac{3+\beta}{4}. \end{aligned} \tag{28}$$

Therefore, for $\beta = 4$ the known value $\alpha = 7/4$ for the *Bahcall Wolf cusp* when looking at the distribution of stars around a BH [48] or the common literature value found for SIDM [9, 28, 30] is recovered.

2.7.2. Equilibrium in SMFP

Considering the SMFP regime, only the left term in the bracket of eq. (26) is used, giving:

$$L = -4\pi r^2 \frac{3b\rho\nu}{2\rho\sigma} \frac{\partial \nu^2}{\partial r} \propto r^2 \nu \sigma^{-1} \frac{\partial \nu^2}{\partial r}. \tag{29}$$

By collecting everything, the following equation is obtained:

$$\begin{aligned} L &\propto r^2 r^{-1/2} r^{-\beta/2} r^{-2} = r^{-(\beta+1)/2} \stackrel{!}{=} \text{const} \\ &\Leftrightarrow \beta + 1 = 0 \Leftrightarrow \beta = -1. \end{aligned} \tag{30}$$

This means that in the SMFP there is only an equilibrium solution if $\sigma \propto v$. The power-law index of the density does not seem to play a role here!

However, I note that in [40] a different result is stated if the halo is in the SMFP regime:

$$\rho \propto 1 + \chi \, (r_h/r)^{3/2}, \quad \chi \sim \mathcal{O}(1). \tag{31}$$

There, it is assumed that the BH accretes particles via a constant and spherical Bondi flow

$$\frac{\mathrm{d}M}{\mathrm{d}t} \propto r^2 \rho v, \tag{32}$$

so that when $v \propto r^{-1/2}$ and $\frac{\mathrm{d}M}{\mathrm{d}t} = \text{const}$, $\rho \propto r^{-3/2}$ is recovered.
Physically, setting the accretion rate constant implies that a fixed number of particles flow through a surface per unit time. Conversely, in the fluid model a constant luminosity corresponds to a constant energy per unit time flowing through a surface. Since particles can carry different amounts of energy, the number of particles crossing a shell can vary even when the total energy flux remains constant.
This distinction implies that these two approaches - constant accretion rate vs. constant luminosity - are not expected to yield the same density scaling of the DM halo.

2.7.3. Equilibrium in a combined regime

Finally, in the combined regime, both terms in the brackets are taken into account. The difference to the two previous scenarios lies only in the bracketed terms and so it is sufficient

	LMFP	SMFP	LMFP+SMFP	LMFP+SMFP
β	any	-1	> -1	-1
α	$(3+\beta)/4$	any	$(3+\beta)/4$	$\geq 1/2$

Table 1: Slope index α at equilibrium, when velocity-dependence of cross-section is $\sigma \propto v^{-\beta}$ and halo is in either the SMFP, LMFP or a mixed regime. In the mixed regime, a distinction has to be made depending on whether $\beta = -1$ or $\beta > -1$.

to focus only on them. Dropping all constants in the equations, since the interest here lies only in the scaling of the luminosity rather than its absolute value, yields the following expression:

$$\left[\rho\sigma + \frac{1}{\rho\sigma r^2}\right]^{-1} = \left[\frac{\rho^2 r^2 \sigma^2 + 1}{\rho\sigma r^2}\right]^{-1} = \left[\frac{r^{-2\alpha} r^2 r^\beta + 1}{\rho\sigma r^2}\right]^{-1}. \tag{33}$$

Three cases can now be determined depending the term that dominates for small radii, $r \ll 1$:

$$\begin{aligned} r^{-2\alpha+2+\beta} &\ll 1, \text{ if } -2\alpha + 2 + \beta > 0 \Rightarrow \text{LMFP} \\ r^{-2\alpha+2+\beta} &\gg 1, \text{ if } -2\alpha + 2 + \beta < 0 \Rightarrow \text{SMFP} \\ r^{-2\alpha+2+\beta} &\approx 1, \text{ if } -2\alpha + 2 + \beta \approx 0 \Rightarrow \text{LMFP} \approx \text{SMFP} \end{aligned} \tag{34}$$

The first case applies if $\alpha < 1 + \beta/2$. Comparing this to the result for a constant luminosity in the purely LMFP regime (eq. (28)), gives a constraint on the possible a:

$$\frac{3+\beta}{4} < 1 + \frac{\beta}{2} \Leftrightarrow \beta > -1 \tag{35}$$

Hence, the solution in the mixed case reduces to that of the LMFP for $\beta > -1$.
On the other hand, the second case applies if $\alpha > 1 + \beta/2$. Once again looking at the equilibrium case in the SMFP, $\beta \overset{!}{=} -1$ so that

$$\alpha > 1 - 1/2 = 1/2, \tag{36}$$

giving a constraint on the possible power-law index of the density.
Finally, when $\alpha = 1 + \beta/2$, a truly new case appears where the equilibrium solution is different. Both the SMFP and LMFP regimes are of similar scaling which means that an equilibrium solution has to satisfy both regimes equally:

$$\alpha = \frac{3+\beta}{4} = 1 + \frac{\beta}{2} \overbrace{=}^{\beta=-1} 1/2. \tag{37}$$

To summarize: in the mixed regime, constraints are imposed on the possible velocity-dependencies of the cross-section, β, and the resulting spike indices, α. A summary of these findings can be found in table 1.
In the following, generally only the LMFP case is considered.

3. Numerical approach

This section outlines the numerical approach used to solve the gravothermal fluid equations (eqs. (7), (8), (11) and (12)). The methodology for solving these equations follows [22, 35], with several modifications introduced to address the specific challenges encountered. Key numerical issues encountered during the implementation are also discussed, along with the techniques I employed to resolve them.
The code I used in this work [17] is based on the `GravothermalSIDM` code, which was previously employed to study SIDM halos [49, 50].
To model the impact of the BH, I used ideas presented in [40]. However, the specific implementation of this approach is the result of my own research.

3.1. Simulation of SIDM halo

In order to solve the gravothermal fluid equations numerically, it is useful to convert all dimensional, x_i, variables into dimensionless, $\tilde{x}_i$, ones using fiducial variables, $x_{0,i}$:

$$\tilde{x}_i = \frac{x_i}{x_{0,i}}. \tag{38}$$

It is important to note that x_i and $x_{0,i}$ should be of similar scale, as different orders of magnitudes of these numbers might lead to unnecessary numerical errors. The following fiducial quantities that depend on the parameters of the initial DM halo ρ_s and r_s are used:

$$\begin{aligned} r_0 &= r_s & \rho_0 &= \rho_s \\ M_0 &= 4\pi\rho_s r_s^3 & \sigma_0 &= (\rho_s r_s)^{-1} \\ v_0 &= (4\pi G\rho_s)^{1/2} r_s & L_0 &= (4\pi)^{5/2} G^{3/2} \rho_s^{5/2} r_s^5 \\ t_0 &= (4\pi G\rho_s)^{-1/2}\,. \end{aligned} \tag{39}$$

Converting the gravothermal fluid equations into a dimensionless form, gives:

$$\frac{\partial \tilde{M}}{\partial \tilde{r}} = \tilde{r}^2 \tilde{\rho} \tag{40}$$

$$\frac{\partial\left(\tilde{\rho}\tilde{v}^2\right)}{\partial \tilde{r}} = -\tilde{\rho}\frac{\tilde{M} + \tilde{M}_{BH}}{\tilde{r}^2} \tag{41}$$

$$\frac{\partial \tilde{L}}{\partial \tilde{r}} = -\tilde{r}^2\tilde{\rho}\tilde{v}^2\left(\frac{\partial}{\partial \tilde{t}}\ln\left(\frac{\tilde{v}^3}{\tilde{\rho}}\right)\right) \tag{42}$$

$$\tilde{L} = -\frac{3}{2}\tilde{r}^2\left[\frac{\tilde{\sigma}}{b\tilde{v}} + \frac{1}{C}\frac{1}{\tilde{H}^2}\frac{1}{\tilde{\rho}^2\tilde{\sigma}\tilde{v}a}\right]^{-1}\frac{\partial \tilde{v}^2}{\partial \tilde{r}} \tag{43}$$

[17] The code can be found on GitHub (`https://github.com/Alex-Dreichner/GravothermalSIDM-BH/tree/master/my%20work`).

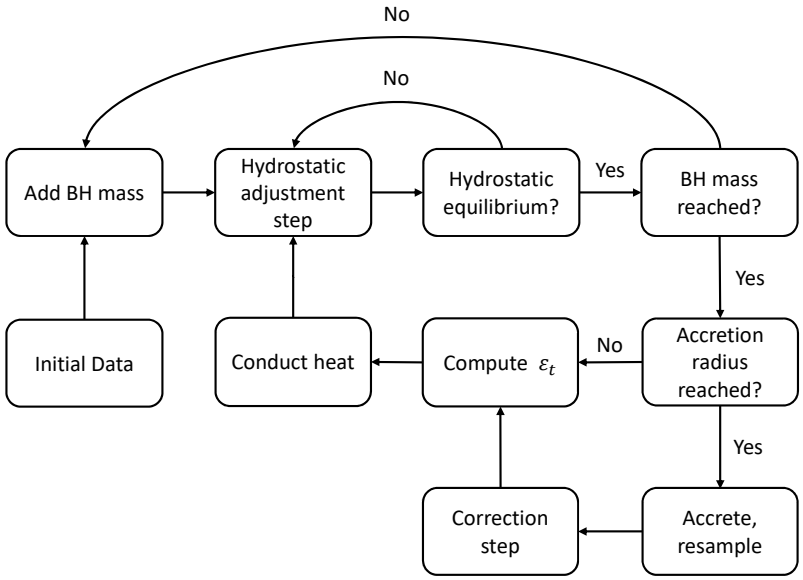

Figure 6: Flowchart of how the simulation of the SIDM halo is implemented in the code.

The process of how the simulation is conducted is explained in fig. 6. The simulation starts with the initial density, usually a NFW density profile, from which the remaining halo variables are calculated (see section 3.1.1).
In the next step of the process, the BH is incorporated iteratively, with the entire BH mass being added piece-by-piece. Choosing initial conditions where the BH is not grown adiabatically, but instead inserted from the beginning, this step is simply skipped.
After each increment in BH mass, the halo is brought back to a hydrostatic equilibrium through repeated hydrostatic adjustment steps (see section 3.1.3). Once the complete BH mass is reached, the heat conduction, and consequently, the temporal evolution can begin (see section 3.1.4).
I introduced the following three additional steps to this process:
In section 2.2 the need of modeling accretion was motivated. When a particle (or shell) reaches the vicinity of the BH, the particle has to be accreted; in the implementation presented here, this means it is in some way removed from the simulation (see section 3.2). In order to maintain a constant number of shells, I then choose to resample the remaining ones, restoring their number to its original value. Because this changes the mass grid, a

correction step is introduced where hydrostatic equilibrium equations with explicit mass and entropy conservation are used (I derive these equations in section 3.1.3).
Finally, the necessary time step is calculated before conducting heat (see sections 3.1.4 and 3.3), thereby perturbing the system and starting the next iteration of the process.

3.1.1. Initialization

To start the simulation some initial values for variables describing the DM halo, e.g., ρ, p, u, ν, M, have to be provided. A NFW density profile is used and all necessary parameters are derived from it:

$$\tilde{\rho}(\tilde{r}) = \frac{1}{\tilde{r}\,(1+\tilde{r})^2}. \tag{44}$$

This allows $\tilde{M}$ and $\tilde{p}$ to be computed directly:

$$\begin{aligned} \tilde{M}(\tilde{R}) &= \int_0^{\tilde{R}} \tilde{\rho}\tilde{r}^2 d\tilde{r} = \int_0^{\tilde{R}} \frac{\tilde{r}^2}{\tilde{r}\,(1+\tilde{r})^2} d\tilde{r} = \frac{-\tilde{R}}{1+\tilde{R}} + \ln(1+\tilde{R}) \\ \tilde{p}(\tilde{R}) &= \int_{\tilde{R}}^{\infty} \frac{\tilde{\rho}\tilde{M}}{\tilde{r}^2} d\tilde{r} = \int_{\tilde{R}}^{\infty} \frac{\frac{-\tilde{r}}{1+\tilde{r}} + \ln(1+\tilde{r})}{\tilde{r}^2 \cdot \tilde{r}\,(1+\tilde{r})^2} d\tilde{r}. \end{aligned} \tag{45}$$

After this, $\tilde{u} = \frac{3\tilde{p}}{2\tilde{\rho}}$ and $\tilde{\nu} = \sqrt{\frac{2\tilde{u}}{3}}$ can be computed. With all basic thermodynamic quantities now defined, more complex quantities, such as the luminosity, can be derived from them
In the following, the tilde is dropped again and dimensional quantities are stated with the correct unit.

3.1.2. Discretization of equations

Following [22, 32, 35], the differential equations (eqs. (40) to (43)) are solved on a numerical grid. What follows is merely a sketch of the key steps and some technical details are omitted. For a more comprehensive derivation, the following references can be consulted [22, 32, 35].
The halo is divided into N spherical shells, with corresponding radii $r_1, ..., r_N$ which initially are spaced evenly on a log scale. Extensive quantities are then defined at positions $r_1 ... r_N$, while intensive quantities are defined inside the shells at positions $(r_i + r_{i-1})/2$. Eg. M_i is defined at r_i, while ρ_i is defined at $(r_i + r_{i-1})/2$ for $i = 2, ..., N$. Throughout the evolution the mass of each shell is kept constant unless a shell is removed due to accretion.

3.1.3. Solving for hydrostatic equilibrium

Using these definitions, the equation for hydrostatic equilibrium (eq. (41)) reads:

$$\frac{p_{i+1} - p_i}{(r_{i+1} - r_{i-1})/2} = -\frac{M_i'}{r_i^2} \frac{\rho_{i+1} + \rho_i}{2}. \tag{46}$$

Here, M_i' is defined as the sum of the BH mass M_{bh} and the DM halo mass M_i. While executing the time evolution of the simulated DM halo some heat Δu is conducted, changing the properties of the halo. In order to ensure that hydrostatic equilibrium is maintained, perturbations in density, pressure and radius are introduced:

$$p_i \to p_i + \Delta p_i,\ \rho_i \to \rho_i + \Delta\rho_i \text{ and } r_i \to r_i + \Delta r_i. \tag{47}$$

To reduce the number of unknown variables to one, $\Delta\rho_i$ and Δp_i are expressed through changes in the volume [22]

$$\begin{aligned} \Delta\rho_i &= -\rho_i \frac{\Delta V_i}{V_i} = -\rho_i \frac{r_i^2 \Delta r_i - r_{i-1}^2 \Delta r_{i-1}}{\left(r_i^3 - r_{i-1}^3\right)/3}, \\ \Delta p_i &= -\frac{5}{3} p_i \frac{\Delta V_i}{V_i} = -5 p_i \frac{r_i^2 \Delta r_i - r_{i-1}^2 \Delta r_{i-1}}{r_i^3 - r_{i-1}^3}. \end{aligned} \tag{48}$$

The assumption that adjusting the halo into hydrostatic equilibrium is an adiabatic process was used here giving rise to an adiabatic invariant, $pV^{5/3} = const$, and equals the conservation of entropy.

What follows now is a slightly different approach in obtaining $\Delta\rho_i$ and Δp_i motivated by two issues that I have encountered:
For one, the equation for mass conservation (eq. (45)) is not explicitly used after initializing the halo parameters. In my studies I have found that over time this equation can fail to be fulfilled, i.e., $\frac{\partial M}{\partial r} \neq \rho r^2$. This issue particularly arises, when the mass of the shells is altered due to accretion and does not occur in a SIDM-only simulation.
As a result, instead of using $\Delta\rho_i$ in eq. (48) the discrete form of eq. (45) can be used to obtain $\Delta\rho_i$:

$$\begin{aligned} \frac{\partial M}{\partial r} &= r^2 \rho \\ \frac{M_{i+1} - M_i}{r_{i+1} + \Delta r_{i+1} - r_i - \Delta r_i} &= (r_i + \Delta r_i)^2 (\rho_i + \Delta\rho_i) \\ \Rightarrow \Delta\rho_i &= \frac{M_{i+1} - M_i}{r_{i+1} + \Delta r_{i+1} - r_i - \Delta r_i} \frac{1}{(r_i + \Delta r_i)^2} - \rho_i. \end{aligned} \tag{49}$$

The other issue is the way entropy is conserved. In the standard formulation, entropy conservation is implicitly used in deriving Δp_i. This approach conserves entropy at first order, but does not explicitly includes it in solving the equations.
However, I find that entropy can be used to completely replace p by ρ and s. The entropy on a discrete grid is given by $s_i = \ln v_i^3/\rho_i$. Since it is conserved during the hydrostatic adjustment, the term in the logarithm is as well and $s_i' = v_i^3/\rho_i$ can simply be taken as the conserved quantity instead. Additionally using $p = \rho v^2$ gives:

$$p_i = \rho_i^{5/3} s_i'^{2/3}\ ,\ \Delta p = \frac{5}{3} s'^{2/3} \rho^{2/3} \Delta\rho, \tag{50}$$

so that $p_i + \Delta p_i$ can be replaced by eq. (50) and $\Delta\rho_i$ can be replaced by eq. (49), transforming eq. (46) to an equation only in Δr_i as well as quantities that are known, e.g., ρ_i, p_i, s_i, r_i.

Solving the equations from here on progresses in the same way as described in [22, 32]. Equation (46) is multiplied by the denominators of both sides, all terms are moved to one side and only terms at first order in Δr are kept, which results in terms linear in Δr_i, Δr_{i+1}, Δr_{i-1}, and terms independent of Δr (see appendix A for the full expressions). Then, the following boundary conditions are assumed:

$$r_0 = 0 \ , \ \Delta r_0 = 0 \ , \ \Delta r_N = 0. \tag{51}$$

This results in a tridiagonal matrix equation for $i = 1, ..., N-1$,

$$\begin{pmatrix} b_1 & c_1 & & & \\ a_2 & b_2 & c_2 & & \\ & a_3 & b_3 & \ddots & \\ & & \ddots & \ddots & c_{N-2} \\ & & & a_{N-1} & b_{N-1} \end{pmatrix} \cdot \begin{pmatrix} \Delta r_1 \\ \Delta r_2 \\ \vdots \\ \Delta r_{N-2} \\ \Delta r_{N-1} \end{pmatrix} = - \begin{pmatrix} d_1 \\ d_2 \\ \vdots \\ d_{N-2} \\ d_{N-1}, \end{pmatrix} \tag{52}$$

which is particularly easy to solve and allows to compute Δr_i, thereby solving the hydrostatic adjustment equation.
After each iteration, the updated density and pressure can be obtained by employing either eq. (48) or eqs. (49) and (50). This process is repeated until $\Delta r/r$ is small enough; I used $\Delta r/r \overset{!}{<} 10^{-10}$.

3.1.4. Heat conduction

In the previous section, the amount of heat conducted Δu as well as the change in entropy Δs imposed by the temporal evolution were taken to be arbitrary. The section below specifies how Δu is obtained and explains how Δs is computed and affects the halo.

The time evolution through heat conduction is governed by eq. (42):

$$\frac{\partial L}{\partial r} = -r^2 \rho \nu^2 \left(\frac{\partial}{\partial t} \ln \left(\frac{\nu^3}{\rho} \right) \right)_M . \tag{53}$$

Following the approach in [35], it is assumed that heat conduction changes mainly the velocity dispersion, but leaves the density constant. One can then derive an equation for the change of internal energy [32, 35]:

$$\frac{\partial u}{\partial t} = -\frac{\partial L}{\partial M} \Rightarrow \Delta u_i = -\Delta t \left(\frac{L_i - L_{i-1}}{M_i - M_{i-1}} \right). \tag{54}$$

Using the definition of the entropy on the other hand, eq. (53) can immediately be rewritten into:

$$\frac{\partial s}{\partial t} = -\frac{1}{r^2 \rho \nu^2} \frac{\partial L}{\partial r}. \tag{55}$$

The RHS of this can be simplified using eq. (45):

$$\frac{1}{r^2\rho}\frac{\partial L}{\partial r} = \frac{1}{r^2\rho}\frac{\partial L}{\partial M}\frac{\partial M}{\partial r} = \frac{1}{r^2\rho}\rho r^2\frac{\partial L}{\partial M} = \frac{\partial L}{\partial M}, \tag{56}$$

so that a discrete equation for the entropy evolution is obtained:

$$\frac{\partial s}{\partial t} = -\frac{1}{v^2}\frac{\partial L}{\partial M} \Rightarrow \Delta s_i = -\Delta t\frac{1}{v_i^2}\frac{L_i - L_{i-i}}{M_i - M_{i-1}}. \tag{57}$$

In both cases the luminosity L can be directly obtained from eq. (43) and $L_0 = 0 = M_0$. The time step Δt is chosen in a way that keeps the changes small compared to the quantity changed. Specifically, this means that

$$\max\left(\left|\frac{\Delta u_i}{u_i}\right|\right) < \varepsilon_t = 10^{-4} > \max\left(\left|\frac{\Delta s_i}{s_i}\right|\right) \tag{58}$$

for the respective approach.

To evaluate the impact of heat conduction on the halo, consider first the approach where density is held fixed. In this case, a change in the internal energy directly implies a change in pressure, since $p \propto u\rho$ through the equation of state:

$$\frac{\Delta u}{u} = \frac{\Delta p}{p} \Rightarrow \Delta p_i = p_i\frac{\Delta u_i}{u_i}. \tag{59}$$

After heat is conducted, the pressure becomes $p_i + \Delta p_i$, which brings the halo out of hydrostatic equilibrium. To restore equilibrium p, ρ and r are perturbed using the method described in the previous section until the halo once again reaches a hydrostatic equilibrium. In the second approach, the entropy is explicitly changed. In this case, there is no need to adjust any other quantities initially. Instead, the entropy change enters directly with the entropy in the hydrostatic equilibrium equation (eq. (50)), causing p, ρ and r to be adjusted to new values, until the halo is once again in hydrostatic equilibrium.

Conceptually, both methods are equivalent: in the first, the perturbation is introduced via a change in internal energy (and hence pressure), while in the second, the perturbation is introduced through a change in entropy.

3.2. Accretion of DM onto a BH

As described in section 2.2, an inflow of matter towards the BH is expected. To model the accretion onto the BH, mass shells that cross the accretion radius r_{acc} need to be modified in some way.

3.2.1. Defining the accretion radius

First, a suitable accretion radius needs to be defined. The most straightforward choice here is to simply take the physical accretion radius for matter around a BH, $r_{acc} = 4GM_{bh}/c^2$ [39]. Generally speaking, it is very small compared to characteristic halo scales and so this is not a very practical choice if the innermost grid point is far away, i.e., $r_1 \gg r_{acc}$. I have observed in my simulation that if this accretion radius is chosen initially, the shell at r_1 tends to move inwards quickly while the other shells do so at a much slower speed (or might even be moving slightly outwards), creating an increasingly bigger distance to the next closest point until $r_1 \ll r_2$. This can cause numerical issues in the derivatives of quantities, as the spacing $r_i - r_{i-1}$ grows uneven. The code can then fail to return the system to hydrostatic equilibrium.
Figure 7 shows a zoom on the inner region in the early stages of the simulation. For $t < 10^{-12}$Gyr and the innermost grid points, the halo slightly relaxes with density decreasing as the shells move outwards, except for the innermost point that moves inwards and increases its density. In the last time step shown (at $t = 1.05 \cdot 10^{-12}$Gyr) the position of the innermost point quickly reduces significantly while at the same time the density rises by almost two orders of magnitude compared to the second to last time step ($t = 9.63 \cdot 10^{-13}$Gyr). Conversely, all other grid points remain at roughly the same position and density. At this point in time, the innermost grid point has moved too far inwards compared to its neighbor. Consequently, in the subsequent step during the hydrostatic adjustment, the code is unable to return the halo to hydrostatic equilibrium and is terminated after 500 iterations. The resulting density profile (gray) demonstrates a substantial change, with the innermost grid point shifting outward by two orders of magnitude and the corresponding density declining below the density of the halo at this position but in previous points in time. The aforementioned trend continues until negative values of the density are reached, if the code continues to run.
It is worth to note that between the two profiles for $t = 1.05 \cdot 10^{-12}$Gyr, no time has elapsed, and all observed differences appear as a result of the hydrostatic adjustment and are unphysical.
Because of this issue, I choose to iteratively reduce r_{acc} from a value that is reasonably close to the initial r_1, to its final value, $r_{acc} = 4GM_{BH}/c^2$; when a shell crosses the accretion radius, a new accretion radius $r_{acc} = 0.995 r_1$ is defined.

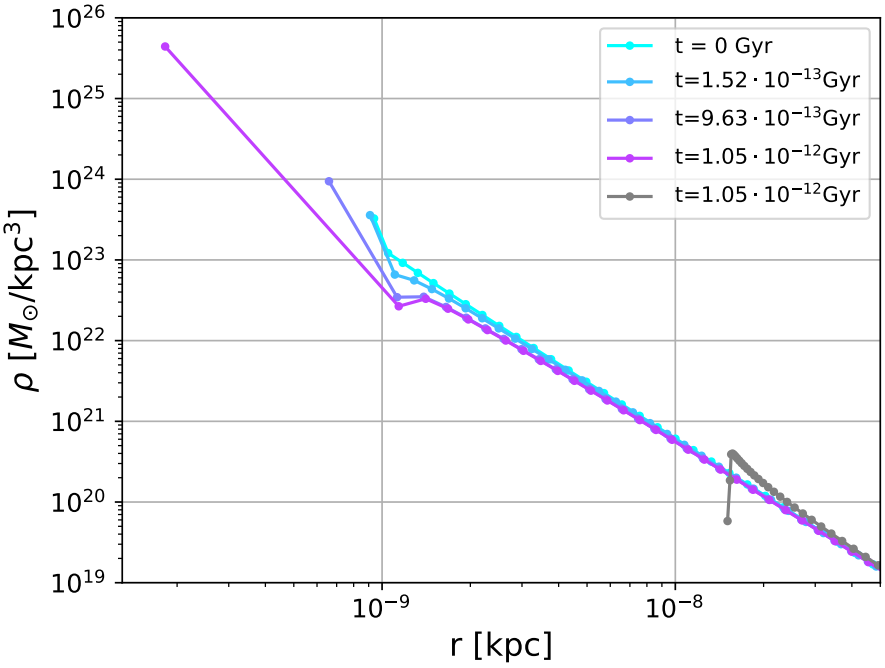

Figure 7: Zoom into inner region of the halo. Shown is the density as a function of the radius. Dots indicate positions of the grid points. Different colors indicate snapshots of different potions in time. At $t = 1.05 \cdot 10^{-12}$Gyr no hydrostatic equilibrium can be found and the code is halted after 500 iterations (gray).

3.2.2. Modeling the accretion

Once a shell crosses the accretion radius, its particles no longer contribute to the evolution of the halo. They stop participating in heat conduction; instead their, mass is subtracted from the halo and added to the BH.
The easiest way to achieve this is to simply remove the grid point, i.e., go from N grid points to $N-1$, and to add the mass of the innermost shell to the BH and subtract it from the remaining halo. However, many such crossings can occur during the whole simulation ($\gg 10^6$). Because the number of shells is much smaller than this (≤ 1000) this approach is not useful, as the shells in the center are depleted over time, causing the spatial resolution in the region that is most interesting to be lost.
Another approach was thus needed and I chose to simply resample shells as necessary. I pick the shell that is closest to the accretion radius but still outside and some n_{max}-th shell and interpolate n_{max} shells between those on a linear grid on a log scale. All thermodynamic quantities, e.g., ρ, p, M, are then taken at a new and slightly offset position with the number of accreted shells added in between. This ensures that the number of shells stays constant, maintaining as high of a degree of accuracy as possible.
Figure 8 shows the effect of this step on the 10 innermost halo grid points. Shown are the density versus radius for a halo with `test1_old` halo parameters (table 2) at $t = 0$ and $t = 8 \cdot 10^{-14}$Gyr. Compared to the initial distribution the density right before the accretion

step is slightly lower, with the innermost grid point moved over the accretion radius and showing a raised density. After accretion, the density follows the same distribution as before for $r \geq r_2$. In the subsequent adjustment, a general shift of all shells towards the center is observed. All points are now outside of r_{acc} and spread more evenly.

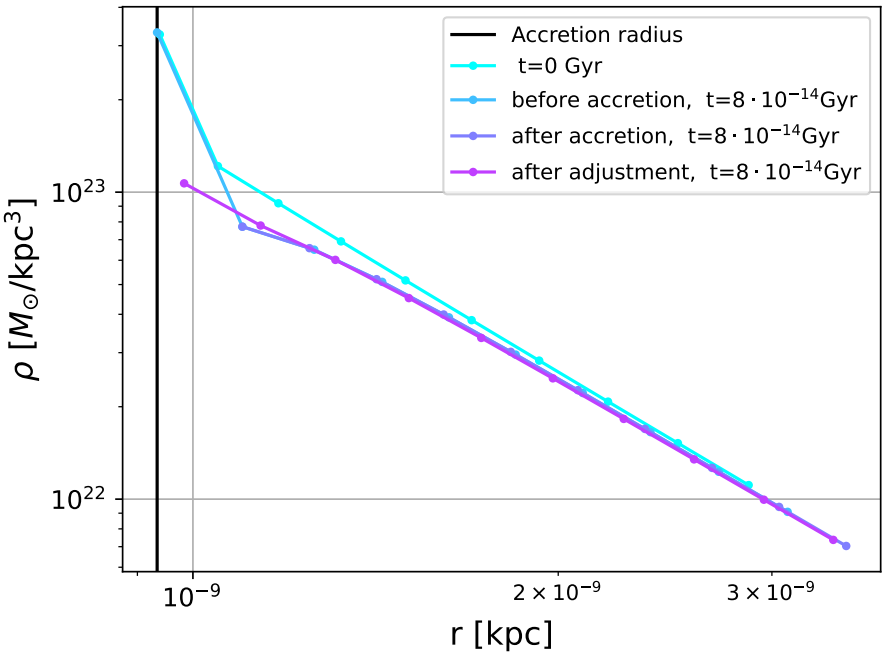

Figure 8: Density as a function of the radius. Dots indicate positions of the grid points. Black vertical line represents the accretion radius used at this stage. Plot shows one iteration with accretion and resampling and with subsequent return to hydrostatic equilibrium, as well as the initial density at $t = 0$.

3.2.3. Reintroducing mass conservation

The introduction of accretion presents an additional challenge to the original method of solving the gravothermal fluid equations. In their derivation, a Lagrangian framework is adopted, which assumes that the mass enclosed within each shell remains constant throughout the evolution. However, once a central BH is included and accretion is introduced, this assumption no longer hold. As a result, eq. (40) is increasingly violated. Because this equation is not actively enforced during the evolution, [18] the system cannot account for the changes in the mass grid. Over time, as mass is repeatedly removed from the halo and the shells are resampled, the error in this equation increases drastically - eventually reaching over 80% (fig. 9a).

[18] In the derivation of eq. (48) it is used implicitly with the assumption that the mass of the shells does not change.

To address this issue, a correction step can be introduced that uses the alternative formulation of solving the gravothermal equations, which gives rise to a change in density (eq. (49)) that explicitly depends on eq. (40).
Figure 9 shows the relative errors in eqs. (40) and (41) initially, after 1000 accretion steps, and after a subsequent correction step. It can be seen, that initially both equations are fulfilled well with relative errors generally just above 10% at most (with the exception of the innermost point that shows a much larger deviation).
After 1000 iterations where matter was accreted, fig. 9a shows that the relative error in eq. (40) is significantly increased for radii smaller than 10^{-7}kpc, with values exceeding 50% for $r \leq 5 \cdot 10^{-10}$kpc. The impact of the correction step is clearly visible; the relative error is significantly reduced and is below 5% for radii smaller than 10^{-4}kpc (again, with the exception of the innermost point). At this point, a sharp increase of the error can be seen compared to the initial profile. This is likely due to its position precisely at the edge of where the interpolation was applied, causing large changes in the area within this radius (see section 3.2.4 for more details).
The relative errors in the hydrostatic equilibrium equation paint a slightly different picture (fig. 9b). After 1000 accretion steps, the error has increased to about 25% for radii smaller than 10^{-4}kpc. [19] Compared to fig. 9a, this increase in the error is notably smaller. However, after the correction step, there is no overall decrease in the error; errors are reduced below their previous values only for radii between $2.5 \cdot 10^{-9}$kpc and $1.2 \cdot 10^{-6}$kpc, but increase at smaller radii and now reach over 60%. This suggests that the alternative approach initially perturbs the halo, driving it away from a hydrostatic equilibrium at first.
Even more concerning is the effect that this correction step has on the density of the halo. In the beginning, the slope index of the density shows a good agreement with the expected solution $\alpha = 7/3$ in the inner region (fig. 9c). Over time, a relaxation of the halo towards $\alpha = 7/4$ is expected and this trend can be confirmed when examining the halo at $t = 2 \cdot 10^{-10}$Gyr; the slope index shown is within 3% of the expected solution for radii smaller than $6 \cdot 10^{-9}$kpc before the correction. However, after the correction is applied, a significant shift of α can be seen for radii smaller than 10^{-6}kpc. The deviation from the expected value is much larger now; the innermost points show a reduction by about 0.2 in the slope index, down to $\alpha \approx 1.5$ - a decrease by about 10%.
Since the main goal of this work is to demonstrate agreement between numerical simulations and analytic predictions of the slope index, this poses a source for concern. It indicates that the correction proposed in this section may unintentionally lead to significant alterations of the halo beyond the intended effect if applied too frequently.
Because of this, I apply this correction to the halo only every 10^4 accretion steps. While this leads to larger errors in eq. (40), it ensures that there are sufficient unperturbed steps to allow the slope index to adjust back to the theoretical solution.

[19] The stark increase seen at $r = 10^{-4}$kpc, can be once again attributed to the choice of n_{max}.

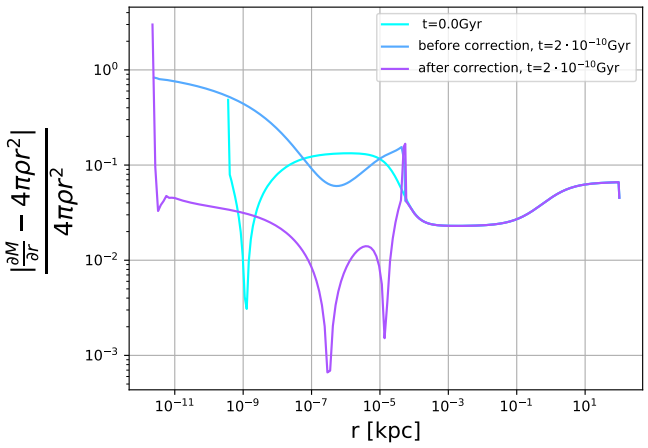

(a) Relative errors in eq. (40)

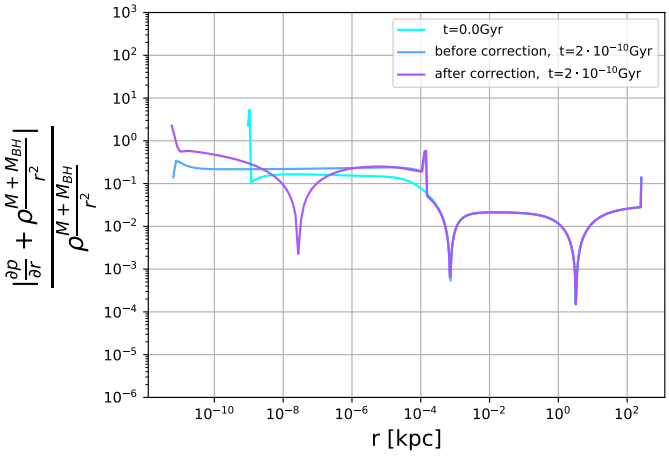

(b) Relative errors in eq. (41)

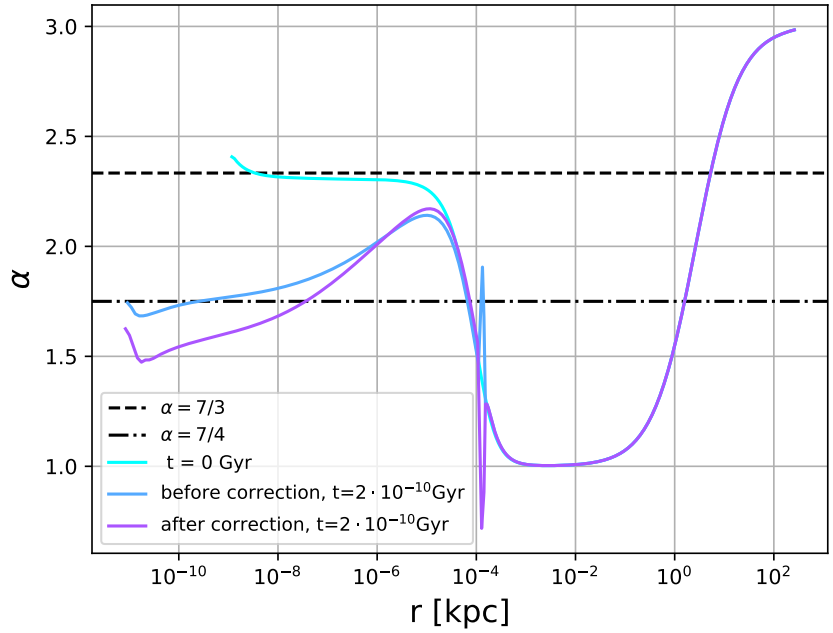

(c) Slope index α. Horizontal lines indicate the theoretical slope index at the beginning ($\alpha = 7/3$) and at equilibrium ($\alpha = 7/4$).

Figure 9: Effects of one correction step using eq. (49) on a halo after 1000 accretion steps. The initial profile is shown for comparison. Based on the discussion in section 3.3, the time step was adjusted.

3.2.4. Selecting the outer boundary for interpolation

In the previous section, the choice to keep the number of shells fixed resulted in the need of interpolation in a certain region. It is used during a key step; to redefine the positions and thermodynamic quantities of the halo during accretion. However, it is not trivial to determine the optimal outer boundary of the interpolation region, described by the index n_{max}, which also serves as the outer boundary of where I apply the correction step.
Using a large value reduces numerical errors in the mass conservation and hydrostatic equilibrium equations (eqs. (40) and (41)) by increasing the number of grid points in the inner regions, where these errors tend to be largest. In other words, with a larger n_{max}, the grid spacing at the center is finer, which results in a better fulfillment of these equations (see fig. 11).
On the other hand, the process of re-sampling introduces small deviations from the hydrostatic equilibrium solution because all quantities are recalculated at slightly moved positions. In the inner region, a dynamical evolution - caused by a physical process such as SIDM scattering - results in much shell movement and changes of thermodynamic variables and these physical changes can counteract occasional unphysical disturbances. However, further out in halo, the evolution is very slow and changes occur over much longer timescales. As a result, introducing even small unphysical perturbations in these regions, especially if these are repeated many times, can lead to unrealistic alterations of the halo. This is the result of simulations when n_{max} is taken to have a large value (see fig. 10 for $n_{max} = 300$).
An ideal choice for n_{max} would ensure that the natural halo evolution can compensate for these unphysical perturbations, i.e., the position is such that more than one scattering is expected before the next time step:

$$\rho\sigma v\Delta t \overset{!}{\geq} 1. \tag{60}$$

This guarantees that changes are imposed only in a region where there is some degree of dynamical evolution going on. However, in practice this is not a very useful approach, as in the cases I have studied generally $\rho\sigma v\Delta t \ll 1$.
Another consideration is that the range where a power-law solution for the density can exist is inherently limited. After all, a key assumption is that $M_{bh} \gg M_{DM}$ in this area, since only in this case does the velocity dispersion scale as $r^{-1/2}$. From studies of SIDM halos without a central BH, it is known that the internal energy initially decreases towards the center (see section 2.2), implying the existence of a local minimum. Consequently, the power-law solution can only be valid in the region inward of this minimum. Based on this, I choose to place n_{max} at precisely this point. [20] A physical flow of matter is expected here, (ideally) washing out numerical inaccuracies during the evolution. This position can shift slightly over the course of the simulation, and the correct choice of n_{max} must therefore be recalculated repeatedly. [21]
In practice this second condition with placing n_{max} at the minimum of the internal energy is working better compared to the first condition.

[20] For sufficiently early times, this choice roughly corresponds to setting n_{max} such that $r_{n_{max}} = r_{h,v}$. At late times, during gravothermal collapse, no local minimum in u exists.
[21] I found $n_{max} \approx 70 - 90$ for the halo parameters used in this work.

To better investigate the impact of a fixed choice of n_{max} on the halo evolution, three cases with $n_{max} = 100, 200$ and 300 are considered. These simulations use the `test1_old` parameters from table 2 and each halo is divided into 400 shells. The corresponding results are shown in fig. 10. The numerical artifacts observed in fig. 10b are caused by the interpolation boundary at n_{max}, so that their position can serve as a proxy for the chosen n_{max}. As a comparison, the variable choice is used, where n_{max} is set at the minimum in the internal energy.
Examining the slope index α (fig. 10b) at the first time step shown after initialization, at $t \approx 2 \cdot 10^{-9}$Gyr, shows that the curves for $n_{max} = 100$ and 200 (green and blue, respectively) are in very good agreement with each other for radii greater than 10^{-3}kpc. The interpolation edge for $n_{max} = 100$ occurs there causing them to deviate slightly for smaller radii. A good agreement can once again be seen for radii smaller than 10^{-5}kpc. Comparing the highest choice of n_{max} (orange) to these results, a noticeable difference for radii between $\approx 10^{-7} - 2$kpc can be seen. Conversely, the variable choice of n_{max} (magenta) is in very good agreement with the smaller choices of n_{max}.
This effect is further exaggerated for later times. At $t = 2.7$Gyr, both the two smallest ($n_{max} = 100, 200$) and the variable choice (green and blue, magenta) show very good agreement in the outer regions of the halo for $r > 10^{-1}$kpc. There it becomes clear, that a higher choice of n_{max} (blue) results in a bigger deviation from the physically expected solution. [22] While the lowest choice, $n_{max} = 100$, does show a formation of the core, the variable choice is able to better capture this; the slope is lower for a larger interval and the numerical artifact is smaller. Once again, the highest choice for n_{max} (orange) results in a significantly altered evolution, altering even the outermost regions of the halo. Despite these differences, all choices result in a similar slope index in the inner region. [23]
A similar result is seen when examining the corresponding density profiles (fig. 10a). At the earliest time step shown, and for radii larger than 10^{-4}kpc, there is good agreement between $n_{max} = 100, 200$ (green, blue) and the variable choice set at the minimum of the internal energy (magenta). Here, the larger numerical artifact seen in the green curve (also visible in fig. 10b just below 10^{-3}kpc) causes a slight deviation from the other two profiles. The largest choice of n_{max} (orange) results in a deviation from the others in a larger area once again. However, at this time step, the distinction between the different choices cannot be seen as clearly in the density profiles as when examining the slope index.
This changes when looking at the latest point in time shown, at $t = 2.7$Gyr. Here, it is very evident where the deviations occur and where the profiles follow the expected flattening of the curve in the middle regions of the halo. Once again, it can be seen that a smaller choice of n_{max} leads to a better agreement with the expected result and a smaller perturbation of the outer halo, where no change is expected.

[22] As explained in section 2.2, the expectation is that over time the halo forms a core with $\alpha = 0$ at the center. Here, $\alpha \approx 0.2$ is observed instead.
[23] The result in the inner region depends on the time step size (section 3.3). In this figure, the modified value is used, resulting in the expected solution, $\alpha = 7/4$, for $\beta = 4$.

When examining how well the numerical equations are fulfilled, a different result is observed.
Figure 11a shows how well the mass conservation is satisfied, i.e., whether M, ρ and r follow the relation specified in eq. (40). At the earliest time step shown, no clear distinction between the different choices can be made; only a slight trend suggests that higher choices of n_{max} lead to slightly higher relative errors. In the innermost regions a general trend can be seen where the errors rise dramatically, reaching values close to 100%. This can be explained by the repeated accretion of DM, causing changes in the mass grids; something that does not occur in the isolated SIDM case.[24] A correction step to mitigate some of these effects was introduced in the previous section.
At later times ($t = 2.7$Gyr), a clearer separation appears, particularly in the plateaus and for radii between 10^{-10}kpc and 10^{-3}kpc. Here, higher values of n_{max} lead to lower errors: for example, the error for $n_{max} = 300$ (orange) is only about one-third of the error of the variable choice (pink).
Looking at the relative errors in the hydrostatic equilibrium (fig. 11b), this effect becomes even clearer; larger choices of n_{max} result in smaller errors and a better fulfillment of eq. (40). The difference between the different choices is slightly more pronounced in this case, with the errors for the choice of $n_{max} = 300$ (orange) being roughly one-fifth of those of the variable choice (pink), which generally results in the smallest n_{max}.

The findings outlined in this chapter suggest that the numerical parameter n_{max} has to be chosen with care. The expected evolution of the spike index tends to favor smaller values of n_{max}, with large values resulting in a nonphysical "evolution" of the halo. However, an analysis of the relative errors indicates the opposite; choosing smaller values leads to greater violation of the governing equations.

[24] In the formulation of the gravothermal fluid model, a lagrangian derivative is used, forcing the mass of the shells to stay constant - something that cannot be done here because of accretion.

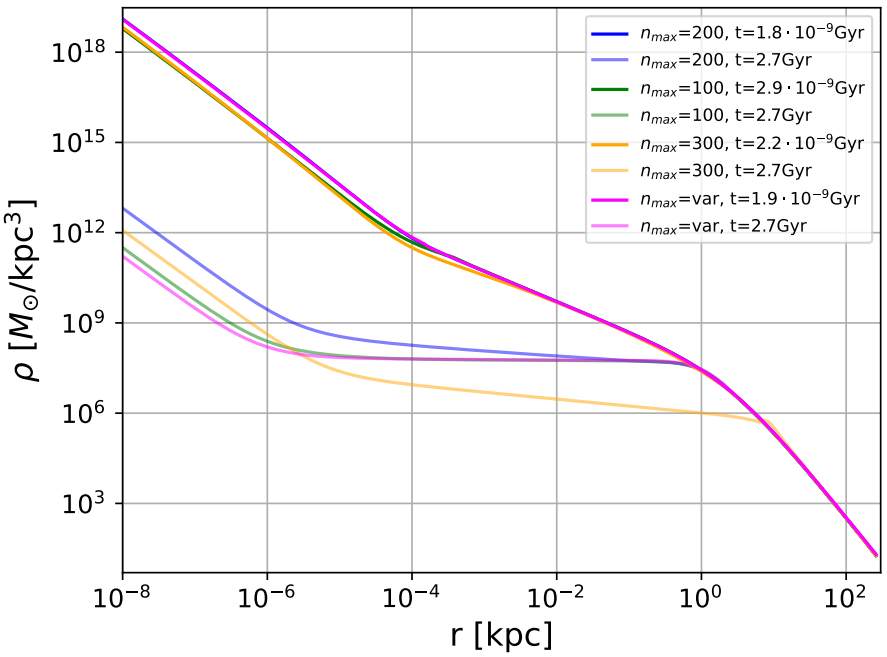

(a) Density

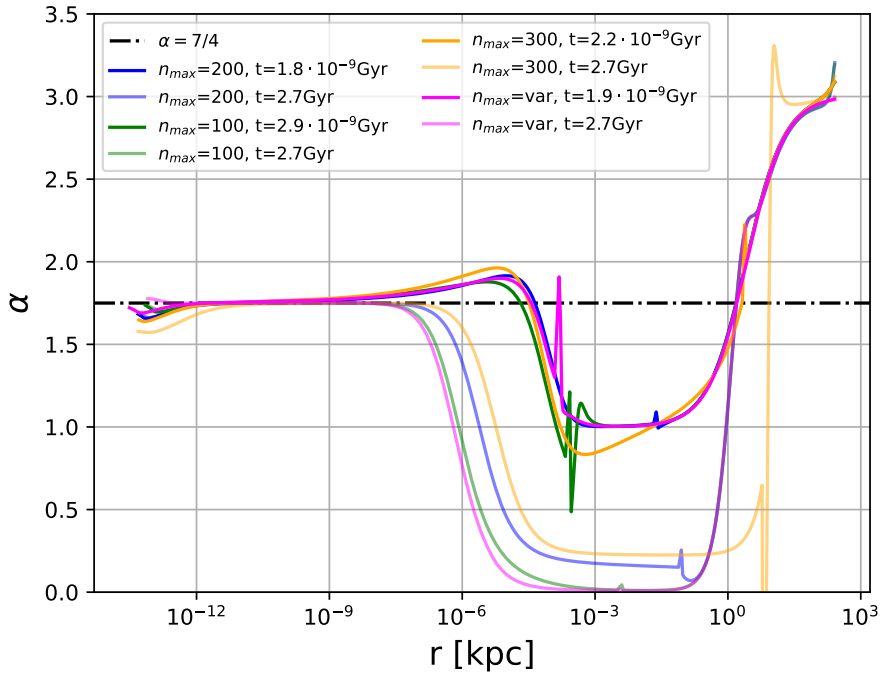

(b) Slope index α

Figure 10: Effect of different choices of n_{max} on halo evolution. Lighter shadings indicate later time steps. $n_{max} = 100, 200, 300$ (green, blue, yellow); otherwise a dynamic choice is taken, placing n_{max} at the minimum of the internal energy (magenta). Note that only when making the later choice, the halo forms a core. The time step size is adjusted according to section 3.3 to obtain the correct slope index at the center.

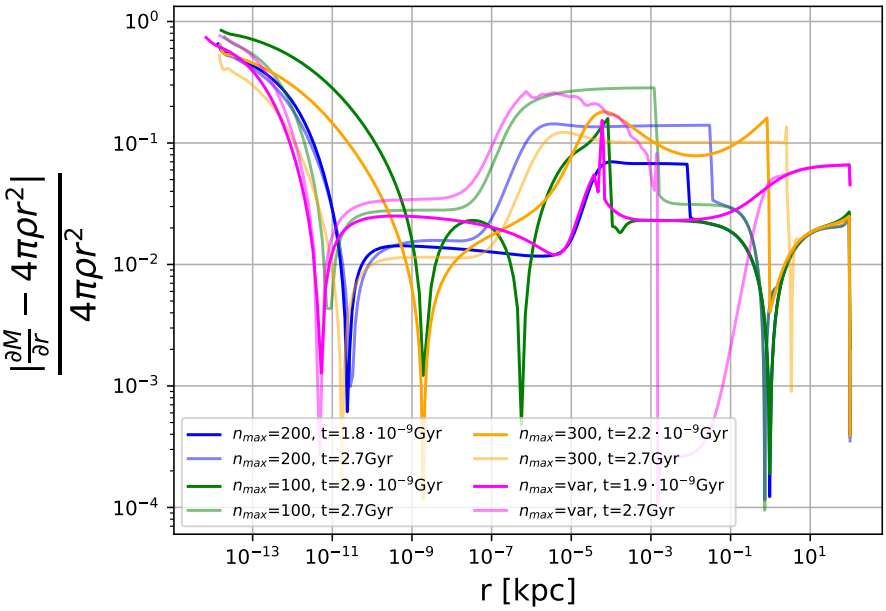

(a) Mass conservation (eq. (40))

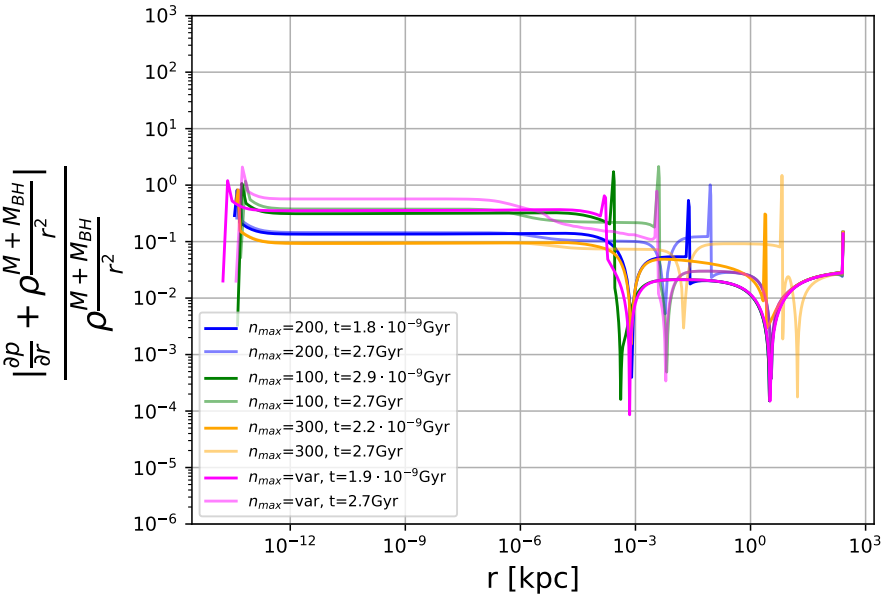

(b) Hydrostatic equilibrium (eq. (41))

Figure 11: Relative errors in the equations that are solved. Lighter shadings indicate later time steps. $n_{max} = 100, 200, 300$ (green, blue, yellow); otherwise a dynamic choice is taken, placing it at the minimum of the internal energy (magenta). Generally, larger n_{max} leads to smaller errors. The jumps in the errors indicate where n_{max} is. The time step size is adjusted according to section 3.3.

3.3. Numerical equilibrium

The approach used in simulating the DM halo in this work results in another option to achieve an equilibrium solution that is not apparent from the discussion in section 2.7 or from looking at the gravothermal equations.
In a physical system, heat conduction and hydrostatic adjustment happen simultaneously - all governing equations are fulfilled at all times. However, numerically, this is not possible and it is resorted to solve them separately. In particular the time evolution governed by eq. (42) and the equation to solve for the hydrostatic equilibrium (eq. (41)) are two distinct steps involved in simulating the SIDM halo. When the effects of both of these processes are of the same magnitude, an interesting phenomenon can arise: a "numerical" equilibrium, where the changes imposed by taking a heat conduction step are reverted by the subsequent hydrostatic adjustment.

To better understand this effect, it is useful to examine the evolution of the entropy. For simplicity, only the innermost region and the case $\sigma \propto \nu^{-4}$ are considered here, but the idea is valid in general.
As derived in eq. (15), initially the velocity dispersion follows $\nu \propto r^{-1/2}$, while adiabatic BH growth results in a density profile that follows a power-law with $\alpha = 7/3$ in the inner region. Therefore, the entropy decreases towards the center, with $s' = \nu^3/\rho \propto r^{5/6}$. Once the time evolution starts and heat is conducted, the entropy in the innermost region starts to increase. This increase, described by eq. (57), which I call Δs_{cond}, is proportional to $r^{-1/2}$. [25] It is therefore immediately clear that only the inner regions are affected and at a certain radius, this change becomes negligible.
In the subsequent hydrostatic adjustment, the position of the shells is adjusted, which generally makes them move inwards, while the entropy per shell remains constant. As a result, the whole profile is shifted inwards, changing the entropy profile as a function of the radius.
Depending on whether the entropy increases or decreases towards the center, two cases can be distinguished. In the first case, if the entropy at the center is larger than further out, then the inwards movement of shells during the hydrostatic adjustment step decreases the entropy as lower entropy shells shift to inner radii. In the second case, if the entropy at the center is smaller, this movement increases the entropy as higher entropy shells move to the inner radii. The second case is relevant initially, when starting with a spiked NFW profile, and when considering the equilibrium solution for $\beta = 4$, where $s' = \nu^3/\rho \propto r^{-3/2+7/4} = r^{1/4}$.
In either case, when any of the shells cross the accretion radius, they are removed from the simulation, effectively cutting the entropy off at the center. Consequently, the hydrostatic decreases the entropy in the first case, and increases it in the second. I call this change Δs_{hydro}.
If this effect is large enough compared to the physical change, Δs_{cond}, the entropy at the center increases until it reaches a flat profile, rather than the expected $s' \propto r^{1/4}$. Moreover,

[25] I assume the halo has evolved but is not yet in equilibrium as in section 2.7 and has a spike-index of $\alpha = 2$.

if the entropy happens to have an increasing profile towards the center, [26] the change introduced by the hydrostatic adjustment acts to reduce it to a flat profile. I find that this process creates a numerical equilibrium in which the entropy is constant at the center, and shows neither an increase nor a decrease.
Because the velocity dispersion scales like $r^{-1/2}$ near the BH, the scaling of the density under these circumstances can be determined to be

$$s = \ln\left(v^3/\rho\right) = \text{const} \Rightarrow v^3/\rho = \text{const} \Rightarrow \rho \propto v^3 \propto r^{-3/2}. \tag{61}$$

Interestingly, this also corresponds to the correct slope in the case $\beta = 3$. As a result, when this effect is not properly accounted for and an unsuitable time step is picked, the resulting density slope might be the same across all velocity dependencies. This is what I observed when using the method described so far.

To illustrate this effect, I consider a DM halo with $\sigma \propto v^{-4}$ after the simulation has run for some time. Figure 12a shows the entropy profile if the approach described so far is used with an increased time step parameter $\varepsilon_t = 0.01$. Shown are the entropy profiles before heat conduction (cyan), after one heat conduction step (red) and after the subsequent hydrostatic adjustment (green). The entropy profile remains constant in most of the halo for this step, and in the inner region only a slight change can be seen. This is expected, since by construction the changes of the entropy are kept small, and Δs_{cond} quickly decreases for larger radii. However, the 10 innermost grid points reveal a discrepancy between the results and the theoretical expectations.
Initially, the change due to heat conduction decreases the entropy in this case. Compared to the initial profile, this change is small. However, in the subsequent hydrostatic adjustment step, this change is reverted so that effectively the entropy is increased after this step. This does not happen through an increase in the value on the grid, [27] but instead the whole profile shifts and thus $s(r)$ increases; the result is a slightly flatter profile. Hence, in this step, the effects from the hydrostatic equilibrium and not the heat conduction dominate the evolution of the halo and if this continues over time, the entropy profile becomes flat at the center, independent of the cross-section.

3.3.1. Modifying the time step

To solve this issue, it is necessary to ensure that the changes imposed by heat conduction are larger than the changes imposed by the hydrostatic adjustment and subsequent accretion, i.e., $\Delta s_{cond}/\Delta s_{hydro} > 1$. While Δs_{cond} is given by eq. (57) and can easily be calculated ahead of conduction, Δs_{hydro} is not trivial to compute, as there is no equation giving the exact form of it. Instead, it (not only) depends on Δr and so can only be given *after* a hydrostatic adjustment step has been taken.
To increase the ratio of both changes and thereby ensure, that the changes in entropy are in fact predominantly caused by conduction, I consider the following. The hydrostatic adjustment restores hydrostatic equilibrium after the halo is perturbed; therefore, this

[26] This is relevant for the equilibrium solutions where $\beta < 3$, and for initial conditions where $\alpha < 3/2$.
[27] s_i cannot increase in this step, since the entropy per shell is kept constant during hydrostatic adjustment.

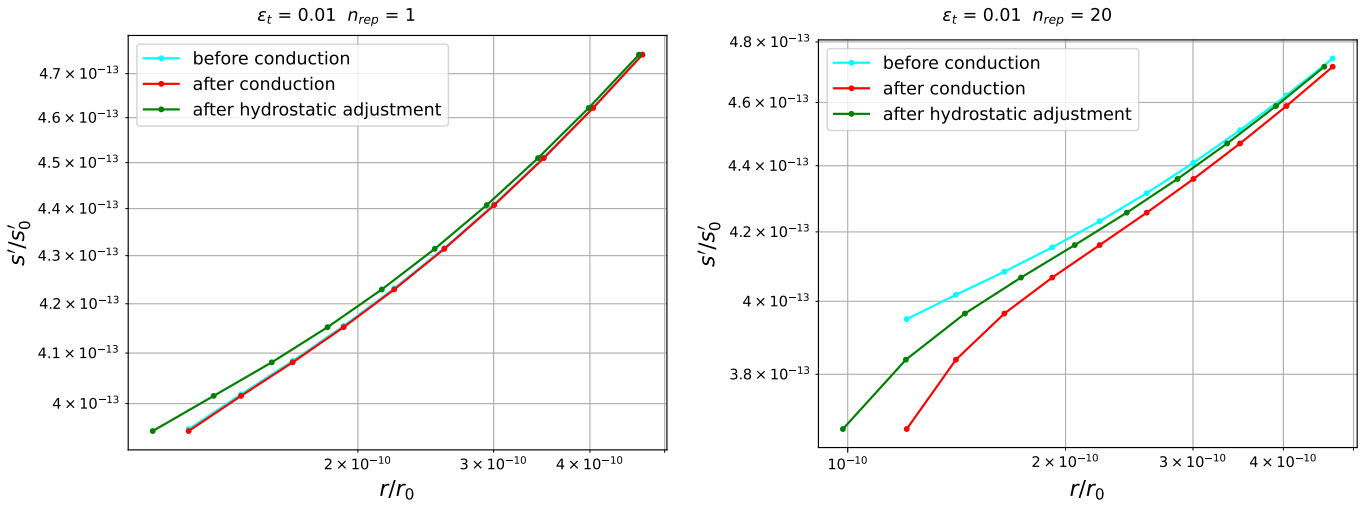

(a) $n_{rep} = 1$ (b) $n_{rep} = 20$

Figure 12: Entropy profiles ($s' = v^3/\rho$) before conduction (cyan), after heat conduction (red) and after hydrostatic adjustment (green). Zoom on the 10 innermost grid points. For larger radii, no difference is visible. The time step parameter, ε_t, and the number of heat conduction steps, n_{rep}, per hydrostatic adjustment need to be strongly increased in order to counteract a flatting of the halo.

step cannot be modified. Modifying it would imply either that the system cannot (fully) return to its hydrostatic equilibrium, or that some additional conditions would need to be introduced. In contrast, the time step in the heat conduction is a numerical parameter and can be chosen arbitrarily within certain bounds. If ε_t is increased, the result is simply a larger Δs_{cond}. The trade-off to this is a reduced numerical accuracy in the integration of eq. (42).

Figure 12b illustrates the result when the time step is effectively increased by a factor of 20. As in the previous case with a smaller ε_t, changes in the entropy remain minor throughout most of the halo and can only be seen in the inner regions. However, a clear difference is visible now: the change in the entropy due to heat conduction is amplified tenfold. As a result of this, after hydrostatic equilibrium is restored, the entropy profile follows the result post heat conduction more closely, and the overall increase and flattening of the profile is no longer observed. Instead, the entropy remains shifted in the direction specified by the heat conduction. [28]

In order to avoid decreasing the accuracy of the time integration too much, ε_t should also not be too large. I impose a maximum value of $\varepsilon_t = 0.01$, which I found to work well empirically. If a larger time step is necessary, multiple heat conduction steps are taken, without performing a hydrostatic adjustment in between. This results in approximately the same overall change as simply taking one larger time step, but since each step is smaller,

[28] I note that this solution does not entirely eliminate the issue and the impact on the spike index remains visible for the innermost few grid points.

the numerical accuracy of the time integration is improved.
While this can be repeated many times in principle, a maximum number of these repetitions, n_{rep}, must be imposed to preserve a good agreement with the boundary condition imposed by eq. (41). This is because the method described in section 3.1.3 assumes that the system remains close to equilibrium after being perturbed; if the deviation is too large, the approximations made to compute Δr break down. I find that a value of $n_{rep} \approx 5 - 10$ yields good results.
For some configurations, particularly when the luminosity is high, this proves to be insufficient - the ratio $\Delta s_{cond}/\Delta s_{hydro}$ remains too small. The simple selection of an even larger value for either ε_t or n_{rep} is not a viable option as it decreases numerical accuracy significantly. Despite this, it is nevertheless possible to increase the number of repetitions if simultaneously reducing ε_t. My findings indicate that $\varepsilon_t n_{rep}$ should not exceed ≈ 0.2, e.g., $\varepsilon_t = 0.002$ and $n_{rep} = 100$.

Finally, I specify the method to determine Δs_{hydro}. Instead of performing a heat conduction step and then comparing the resulting change to that caused by the subsequent hydrostatic adjustment, I choose to compare it with the *previous* hydrostatic adjustment step instead. Ideally, the comparison should be made with the subsequent step, as this is the hydrostatic adjustment physically linked to the conducted heat. However, given that the expected changes should not vary too much from one step to the next, given similar perturbations, this approach gives a reasonable approximation and has the added benefit of being easier to compute.
One final complication arises, because before the hydrostatic adjustment step, the shells are defined at radii r_i while afterwards they are defined at radii $r_i + \Delta r_i$. When computing Δs_{hydro} the entropy before the adjustment, $s_{i,b}$, and the entropy after adjustment, $s_{i,a}$, are thus defined at different radial positions and $\Delta s_{i,hydro} \neq s_{i,a} - s_{i,b}$. To remedy this, the value of $s_{i,a}$ at the new position, must be interpolated back to the old radius r_i. Because the quantities involved span many orders of magnitude, I interpolate on a logarithmic scale to minimize numerical effects. Nevertheless, small interpolation errors are introduced. If these errors exceed the actual entropy change, they can overshadow the true change of the entropy and lead to a false estimate of Δs_{hydro}, resulting in inaccurate time steps.

3.4. Adding DM spike by hand

Numerically simulating SIDM halos with central BHs proves to be computationally expensive. Depending on the halo parameters used, simulations can take weeks to complete.
Consequently, a common approach found in the literature is to simulate SIDM-only halos and then add the expected DM spikes by hand [51, 52]. Using this method, the known power-law solution of the density (derived in section 2.7) is simply added on top of the evolving halo. To do this, the spike radius r_{sp} introduced in section 2.4 is used to define the transition point. The DM distribution is then modified, such that inside of the spike radius the density follows the power-law solution and outside it reduces to the density of

the isolated SIDM (or CDM) halo, ρ_{DM}:

$$\rho_{DM}(r) = \begin{cases} \rho_{DM}\left(r_{sp}\right)\left(\frac{r}{r_{sp}}\right)^{-\alpha} & \text{if } r < r_{sp}, \\ \rho_{DM}(r, & \text{if } r \geq r_{sp}. \end{cases} \tag{62}$$

As shown in section 4.5 the resulting density profiles do not necessarily match with the ones obtained from halo simulations including a central BH. The expression used for the spike radius to stitch the profiles together, plays a significant role here.

4. Results

In this section, I present the final results of my simulations of DM halos. The halo parameters utilized are based on [28, 35, 51] with slight changes for the purposes of this work. A summary of the parameters can be found in table 2.
Note that in [28], the initial density profile is only given in dimensionless units; the dimensional values I used in my thesis chosen for convenience.
For the number of shells, I used $N = 400$ for simulations with a central BH and $N = 201$ for SIDM-only simulations. Other parameters such as the time step size, the velocity-dependence of the cross-section, and a change of the BH mass are specified when relevant. Additionally, only the LMFP regime is considered.

run name	`test1_old`	`shapiro`	`alonso_bh_lmfp`	`shapiro_static`
initial profile	(spiked) NFW	spiked NFW	(spiked) NFW	Plummer
M_{bh} [$M_\odot$]	100	$42 \cdot 10^6$	$6 \cdot 10^9$	$9.42 \cdot 10^5$
r_s [kpc]	2.586	2.586	$2 \cdot 10^3$	$\sqrt{2}$
ρ_s [$M_\odot$/pc^3]	0.0194	0.0194	$3 \cdot 10^{-4}$	$1/(4\pi\sqrt{2}^3)$
σ_0 [cm^2/g]	0.05	5	5	5
v_0 [km/s]	84	84	8050	55

Table 2: Halo parameters used and corresponding run names. Scale radius and density are based on [28, 35, 51]. A BH was added to the halo parameters from [35].

4.1. Results for $\sigma \propto v^{-4}$

Because the case with $\sigma \propto v^{-4}$ leads to the theoretical prediction $\alpha = 7/4$, commonly found in the literature, it serves as a natural benchmark and is therefore presented first. The halo parameters are listed in table 2, and all numerical studies in this work are initially based on these values.
The key goal of this thesis is to numerically simulate the evolution of a DM halo with a central BH and verify the convergence of the central spike index to its theoretical value. Figure 13a shows the slope index as a function of the radius for various time steps. Initially, as expected for an effectively CDM halo (no time has passed), the slope index is close to the theoretical solution $\alpha = 7/3$ after the central BH has grown adiabatically. For $r \geq 10^{-3}$kpc the NFW profile is recovered. As the halo begins to evolve, the inner points move inwards and the slope index starts to decrease to the equilibrium solution, reaching a good agreement by $t = 2.9 \cdot 10^{-9}$Gyr. In the intermediate region, the slope index has slightly relaxed; however, it still mostly follows the NFW profile here ($r \geq 10^{-3}$kpc). As time progresses, the slope index continues to relax in the region $r \approx 10^{-5}$kpc – 10^{-1}kpc, gradually forming a core and reaching $\alpha \approx 0$ by $t = 10$Gyr. At this point changes are only visible for $r < 10$kpc, while the slope index remains very close to the theoretical value in the inner region ($r \lesssim 10^{-7}$kpc). Even during gravothermal collapse ($t = 91$Gyr), this remains the case and changes only occur in the outer regions of the halo.

Because of the approach described in section 3.2, numerical artifacts remain. They appear at the edge of where the interpolation is applied. With time, these artifacts disappear and are barely visible for the later time steps ($t \geq 0.7$Gyr).
The resulting density profile (fig. 13b) shows the evolution from a spiked NFW profile towards a cored profile with a SIDM spike. While the convergence towards the equilibrium spike index is more difficult to judge, the halo clearly forms a core; at $t = 10$Gyr the core spans five orders of magnitude from $r \approx 10^{-5}$kpc to 1kpc. Additionally, the increase of the halo's density during the gravothermal collapse is also readily seen. It is interesting to see, that in the central region the density profiles for $t = 2.7 \cdot 10^{-1}$Gyr and $t = 91$Gyr are virtually indistinguishable. This degeneracy could complicate the inference of DM properties from observational data.
Initially, the internal energy shows a combination of the profile for a SIDM-only halo (fig. 5a) and the expected scaling $u \propto r^{-1}$ in the inner region (fig. 13c). This results in a positive luminosity in the inner region, followed by a negative luminosity in an intermediate region (fig. 13d). For the first three time steps shown, the internal energy profiles are nearly identical. For later time steps ($t \geq 1.1 \cdot 10^{-7}$Gyr), the formation of an isothermal core can be seen, until by 91Gyr, the energy has increased to a point where no minimum is visible anymore. The velocity dispersion ($\nu = \sqrt{2/3u}$) reaches relativistic values of around $\nu/c \approx 0.3$, once the physical accretion radius is reached.
The effects of this are also seen in the evolution of the luminosity (fig. 13d). As the equilibrium solution is approached in the inner region, the luminosity flattens out. Finally, during the gravothermal collapse, the luminosity is positive, with the sole exception at around $r \approx 10^{-5}$kpc. It is not entirely clear if this is a physical property of the halo, or a numerical artifact, causing the luminosity to remain negative in a small area.

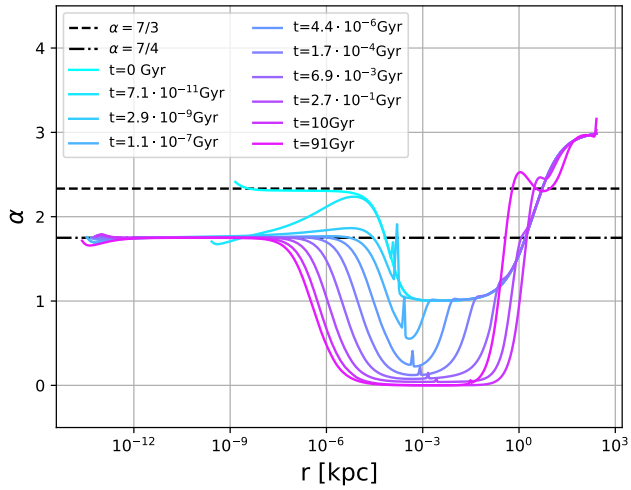

(a) Slope index. Initially, $\alpha \approx 7/3$ (dashed black) at the center. Convergence to the theoretical value, $\alpha = 7/4$ (dashed-dotted black) occurs within 2.9yr. Numerical artifacts between 10^{-4}kpc and 10^{-3}kpc are a numerical artifact from interpolation (see section 3.2).

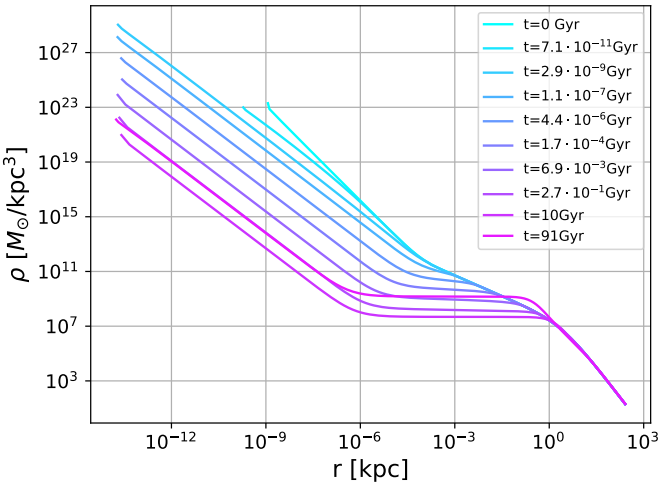

(b) Density profile. Initially, density follows a spiked NFW profile. Over time, a core develops in the intermediate region of the halo. At late times ($t = 91$Gyr), the density is increasing again, indicating an ongoing gravothermal collapse.

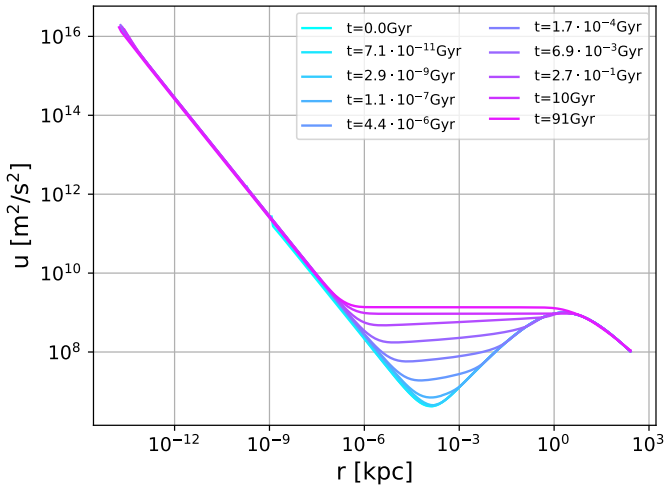

(c) Internal energy. Initially, $u \propto r^{-1}$ at the center. For $r < 10^{-7}$kpc, the energy remains almost constant with time. As the halo evolves, an isothermal core forms. By $t = 91$Gyr the energy has increased to a point where no minimum is visible.

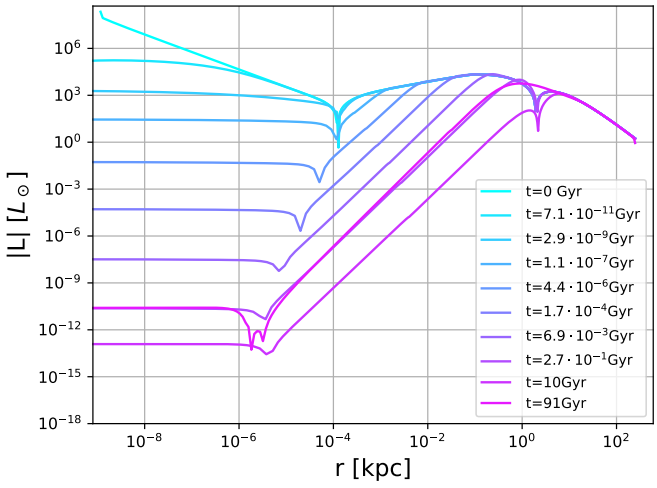

(d) Absolute value of the luminosity. Initially, luminosity increases towards center. Once accretion sets in, the central luminosity flattens ($t \geq 7.1 \cdot 10^{-11}$Gyr) and gradually approaches a constant value. In the intermediate region of the halo, the luminosity is generally negative. During gravothermal collapse (shown at $t = 91$Gyr), luminosity is positive, except in a small area near $r \approx 10^{-5}$kpc, possibly due to a numerical artifact.

Figure 13: Results for a halo evolved using the `test1_old` parameters from table 2 with $\beta = 4$. The central region converges to the expected theoretical solution, while the intermediate and outer halo follow the evolution expected for a SIDM-only halo. At $t = 91$Gyr, gravothermal collapse is clearly observed.

4.2. Mean free path

In section 2.1 the mean free path is given by the jeans length in the LMFP regime. Shapiro argues that in the presence of a BH, this gravitational scale is modified and that "it proves sufficient then to set $H = \min(r, r_J)$" [28]. Figure 14 shows the ratio of r_J and the radial position, r. Looking at this graph, it can be clearly seen that the approach by Shapiro modifies the interaction scale of the particles far outside the area one would assume. Physically, it would be expected (and desired) that this modification is relevant, i.e., $r_J/r \gtrsim 1$, only when $M_{DM}/M_{bh} \lesssim 1$. Surprisingly, depending on the specific parameters used, $r_J/r > 1$ even for M_{DM}/M_{bh} as large as 10^5 and increases over time. Despite this, the impact on the halo is much smaller, with the mean free path increased by about a factor of 50 at most, slightly below $M_{DM} < M_{bh}$.
Nevertheless, this shows that this approach might not be suitable for correctly modeling the impact of the BH on the gravitational scale height. Halo evolution is modified far outside the radius of influence of the BH and even more importantly, the modification is completely independent of the mass of the BH.
As a possible modification of this approach, a function that smoothly interpolates between r and r_J depending on the ratio of the BH mass and the enclosed DM halo mass, M_{bh}/M_{DM}, could be introduced. An example of such a function that explicitly depends on the BH mass is

$$H^2 = r^2 e^{-M/M_{bh}} + r_J^2 e^{-M_{bh}/M}. \tag{63}$$

Using this function ensures that the undesired term is quickly suppressed, i.e., if $M \gg M_{bh}$, $e^{-M/M_{bh}}$ vanishes and $H^2 \approx r_J^2$ and vice versa.

To isolate the effect of this modification on the luminosity of the halo, two cases of a SIDM halo without a BH are considered: One, where the scale height remains unmodified, i.e., $H = r_J$, and the other where the modified scale is used, i.e., $H = \min(r_J, r)$. As can be seen from the result in fig. 15, the halo with the modified luminosity shows a slower evolution of the core. For all time steps shown, the halo with the unmodified evolution (blue) shows a lower slope in the inner regions compared to the modified version (green). This is not unexpected, since decreasing the scale height in eq. (11) results in a smaller luminosity, thus decreasing the speed of evolution.
Therefore, when trying to compare the evolution of a halo with a central BH to a SIDM-only halo, the change due to the different potential, i.e., due to the added gravity of the BH, is accurately captured by a SIDM halo with the modified scale height. Making the comparison to the SIDM halo without this alteration, results in a slower evolution of the halo with a central BH.

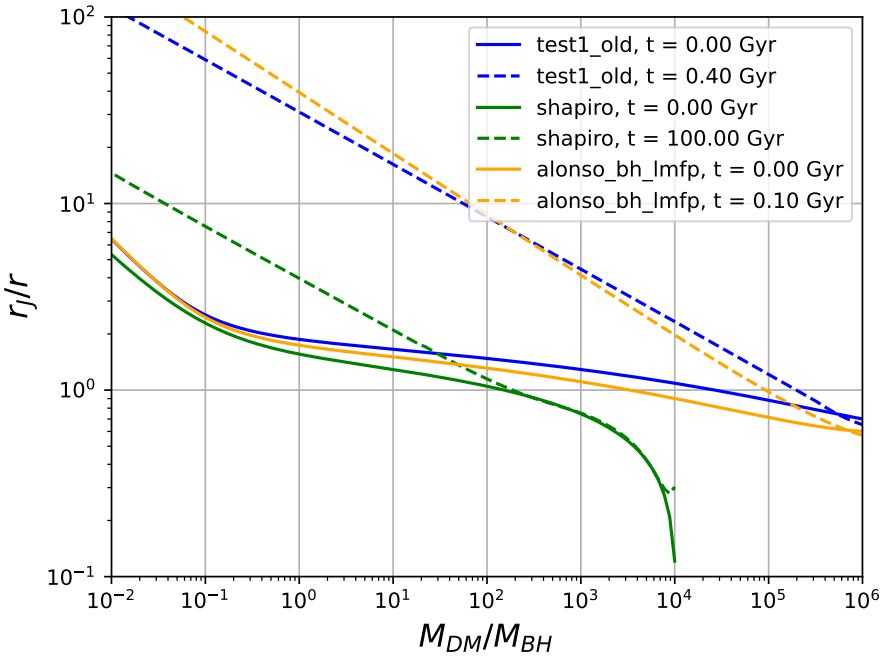

Figure 14: Ratio of the Jean's length r_J and radial position r as a function of the ratio between DM mass and BH mass. Initially profiles (solid) and profiles at later times (dashed) are shown, with halo parameters from table 2. $H = \min(r, r_J)$ can result in $H > r_J$ even for $M_{DM} >> M_{bh}$.

Surprisingly, modifying the scale height does not leave a lasting imprint on the DM halo when a central BH is present.
Figure 16 compares the approach from [28], $H^2 = \min(r^2, r_J^2)$, with the modification of the scale height as a function of BH mass defined by eq. (63).
Initially, a BH is grown adiabatically, producing a spiked NFW density profile with $\alpha \approx 7/3$. Modifying the scale height in the two ways, causes initially differences in the luminosity between $4 \cdot 10^{-4}$kpc and 10^{-1}kpc , as shown in fig. 16a. The inner boundary of this region roughly coincides with the radius where $M(r) = 0.5 M_{bh}$, while the outer boundary extends up to $M(r) = 10^5 M_{bh}$ (see fig. 14 for $t = 0$ and `test1_old`). With the equation proposed by me, the scale height is increased compared to the approach by Shapiro, which results in an increase by about a factor of two in this range. The stars indicate the where the luminosities match again at the center.
However, these differences vanish with time. After the initial phase, the luminosities equalize throughout the whole halo. The notable exception here being the BH mass dependent approach. Here, minuscule fluctuations in the internal energy cause large oscillations of the luminosity between positive and negative values. This fluctuations appears near $M(r) \approx M_{\mathrm{bh}}$, where the function defined by eq. (63) changes behavior, which may be the origin of these fluctuations. Physically, the only difference between both profile for $t > 0$ appears near the center; the luminosity for $H^2 = \min(r^2, r_J^2)$ is slightly higher. Although this might seem counterintuitive (a smaller scale height should lead to a *smaller* luminosity), this can simply be explained by the system evolving more slowly initially. Because

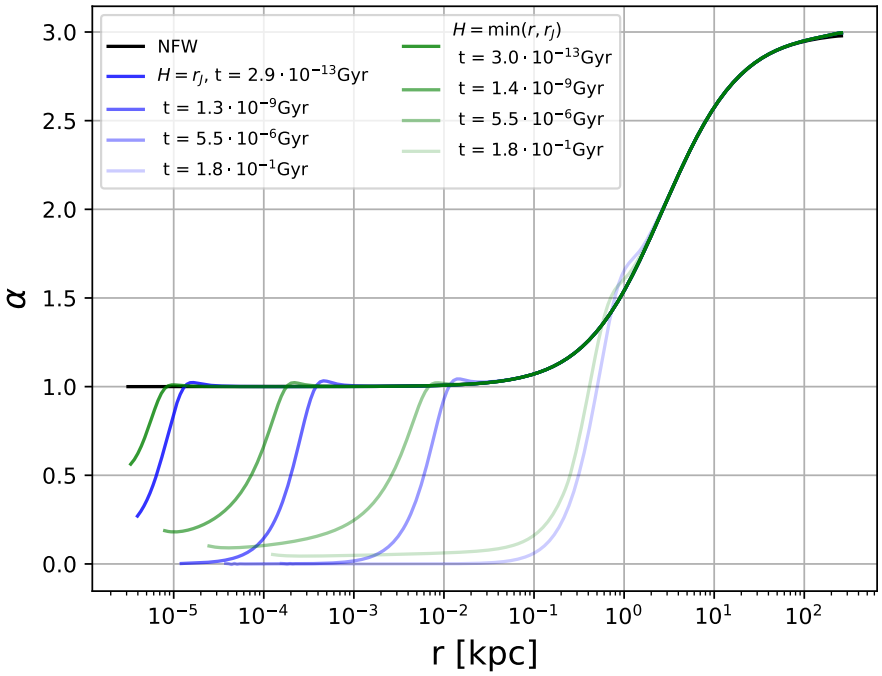

Figure 15: Spike index parameter α as a function of radius for a SIDM halo (blue) and a SIDM halo with a modified luminosity (green). Later times are shown in a lighter shading with a shift towards higher radii for later time steps. The evolution of the unmodified halo progresses quicker. Halo parameters correspond to `test1_old` with $M_{bh} = 0$.

luminosity tends to decrease over time, a slower evolution implies a higher luminosity at a given moment.
The impact of these changes on the density is illustrated by fig. 16b. As seen for SIDM-only halos (fig. 15), the halo with the BH-mass dependent scale height develops a core more quickly; it is both flatter and less dense. Further towards the center, both approaches follow a similar, yet offset profile, indicating a convergence to the same slope index. Again, the stars indicate the position where $M = 0.5M_{bh}$. While the density shows a clear difference for $t = 2 \cdot 10^{-6}$Gyr and $t = 5 \cdot 10^{-3}$Gyr, by $t = 10$Gyr both halos have converged to identical density profiles.

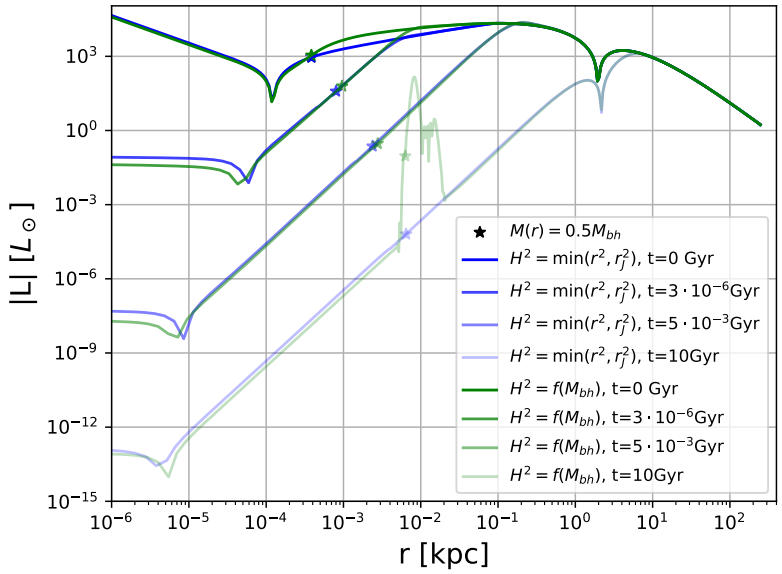

(a) Absolute value of the luminosity. At the radius marked by the stars both luminosities are nearly identical. The large increase for $t = 10$Gyr at $r \approx 10^{-2}$kpc is due to slight numerical errors in the internal energy. Luminosity oscillates between positive and negative values here.

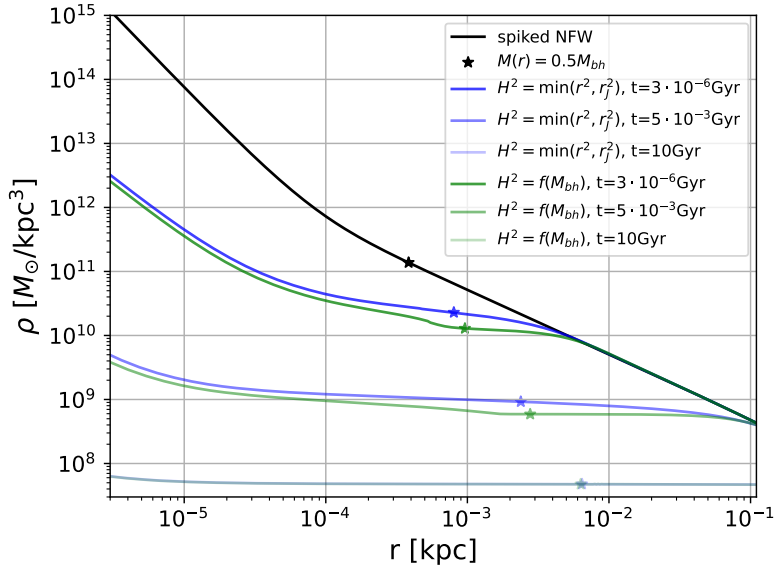

(b) Density profile. Evolution with $H^2 = \min(r^2, r_J^2)$ is slower initially; the density is larger. Differences are generally largest at the radius marked by the star. However, by $t = 10$Gyr, both halos converge to the same profile.

Figure 16: Comparison between setting the scale height to $H^2 = \min(r^2, r_J^2)$ (blue) and using the function described in eq. (63) (green). Both simulations start from the same spiked NFW halo, with parameters given in table 2. Despite the luminosity being different initially, the final profiles converge. Star indicates position where $M(r^\star) = 0.5M_{bh}$ (star). Lighter shadings indicate later time steps.

4.3. Different initial conditions

To test the stability of the code and asses whether the expected spike index can also be produced by starting from different initial profiles, I examine alternative initial conditions. First, conditions based on Section II.A.4 from [28] are used. The corresponding halo parameters are listed in table 2, in the column labeled `shapiro_static`. Unlike in the previous cases, the evolution does not start with a NFW profile that has undergone adiabatic BH growth resulting in the CDM spike with $\alpha = 7/3$. Instead, a Plummer density profile,

$$\rho_P = \frac{3\rho_s}{\left(1 + (r/r_s)^2\right)^{5/2}}, \tag{64}$$

is used, and the outer edge of the halo is kept fixed throughout the evolution. The main feature of the Plummer model is a flat central density with $\alpha = 0$. In theory, the halo should evolve towards the expected solution of $\alpha = 7/4$ in the inner regions, despite different initial conditions.
Figure 17 shows the evolution of the halo through the example of density (fig. 17a) and spike-index (fig. 17b) profiles.
The initially flat profile quickly evolves to higher density in the inner region. The slope parameter makes this evolution clearer and shows that the significant increase in density, respectively the spike parameter, only occurs once accretion sets in, i.e., when inner shells move significantly inwards at around $t = 0.01$Gyr. The spike index in the inner region only flattens out and finally converges to the theoretical solution at this point. The equilibrium solution of the inner region is first achieved at around $t = 0.032$Gyr. Once this occurs, the evolution of the halo is effectively stopped and between this point and $t = 0.99$Gyr no visible changes occur.
One thing to note is that the density of the halo is increasing everywhere with progress in time despite the assumption that the halo mass is kept constant. Thus, eq. (7) is fulfilled progressively worse which can prove to be an issue in predicting the correct density of the halo. However, I have not observed this behavior in any other runs.

To further test the stability of the equilibrium solution, I consider a NFW halo once again. Instead of growing the BH adiabatically, resulting in the CDM slope $\alpha = 7/3$ at $t = 0$, the total BH mass is now included from the beginning, and the pressure is modified to fulfill the corresponding hydrostatic equilibrium equation.
The initial halo parameters used correspond to the `test1_old` run name from table 2. Compared to previous simulations using the same parameters, these initial conditions yield similar thermodynamic variables in the outer regions of the halo, while the inner region is altered.
The results of this simulation are shown in fig. 18. Examining the spike index (fig. 18c) clearly shows the initial difference between both halos. The halo with the adiabatically grown BH (hereafter referred to as *adiabatic BH*) exhibits the CDM spike slope with $\alpha = 7/3$, while the other halo (hereafter *NFW+BH*) simply follows a NFW profile with $\alpha = 1$ at the center. As a result, the densities for radii smaller than $r \approx 10^{-4}$kpc (fig. 18b) also show clear differences. Despite these, the internal energy is very similar for both halos, scaling like $r^{-1/2}$ at the center (fig. 18a). The *adiabatic BH* halo shows a slightly lower

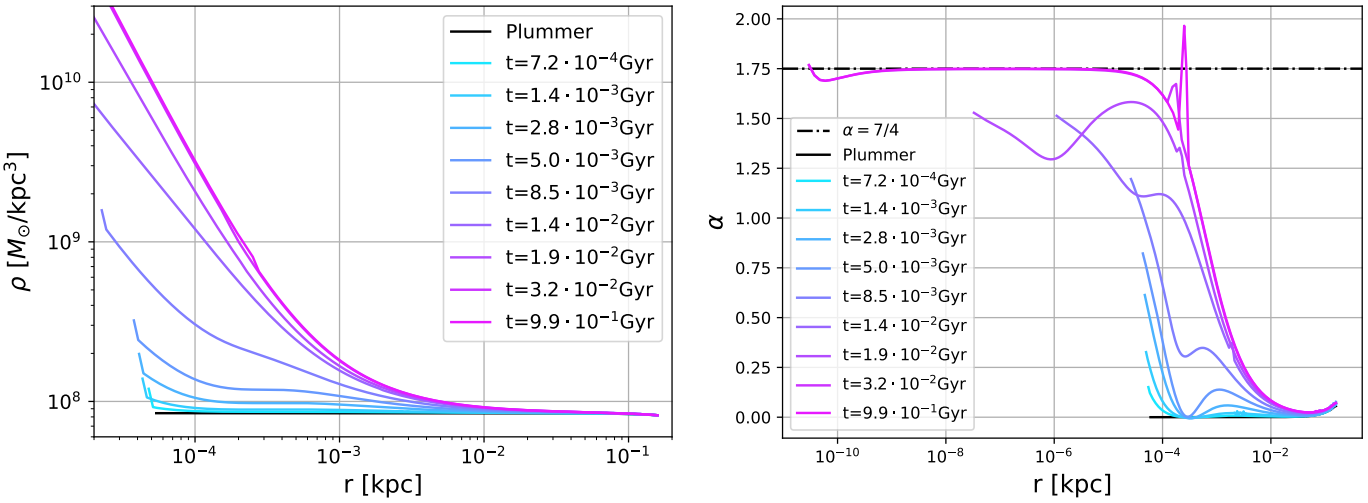

(a) Density profile. A zoom on the outer regions is shown. (b) Spike index profile. Horizontal, dash-dotted line represents the theoretical equilibrium solution $\alpha = 7/4$.

Figure 17: Evolution of a halo from a flat Plummer profile (black) towards a spiked halo with $\alpha = 7/4$. Halo parameters are taken from table 2

minimum internal energy at a slightly smaller radius.
Fairly quickly, after only about a decade (at $t = 1.4 \cdot 10^{-8}$Gyr), both halos can be seen to converge. The spike index falls in a similar range for radii larger than 10^{-5}kpc and only shows significant differences for smaller radii. The density profile also shows increasingly good agreement in this range (fig. 18b), though still diverging for smaller radii. At this points the most notable distinction is that the halo with the *adiabatic BH* extends to much smaller radii, and the convergence towards the equilibrium solution with $\alpha = 7/4$ (fig. 18c) is faster. Here, the spike index reaches the equilibrium solution $\alpha = 7/4$ already at the earliest shown time step (after less than a year), while the *NFW+BH* halo still resembles its initial profile.
By the final time step depicted (at $t \approx 190$yr), both halos exhibit a high degree of similarity, rendering them virtually indistinguishable. For all subsequent time steps, all relevant quantities demonstrate a perfect agreement with between each other. Consequently, the conclusion can be drawn that the halo's equilibrium state is independent of the initial conditions in the inner region. While the outer parts are identical from the beginning, the inner parts ultimately converge to the same solution.
In practice, when simulating SIDM halos, the more practical starting conditions can thus be chosen.

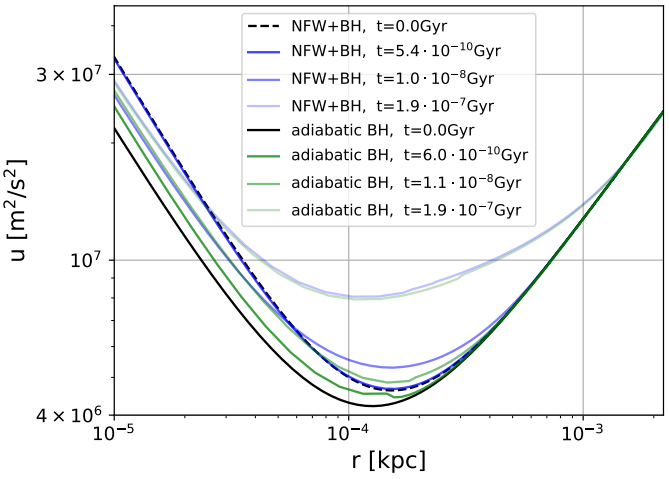

(a) Zoom into internal energy profile

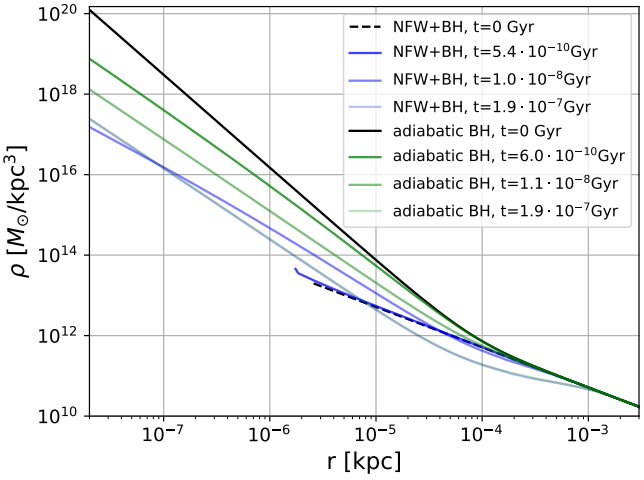

(b) Zoom into density profile

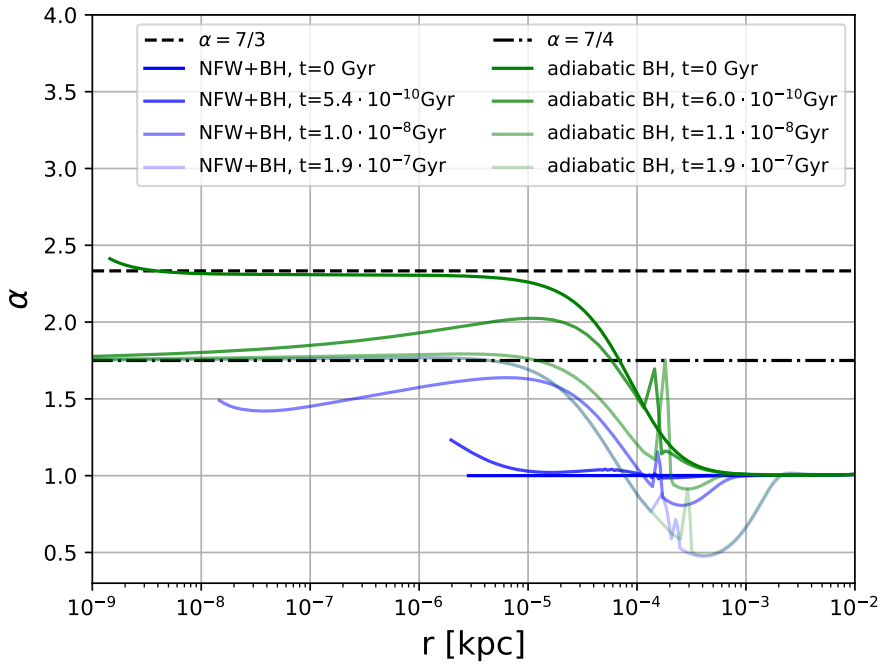

(c) Spike index profile in intermediate region of the halo. CDM spike index ($\alpha = 7/3$, dashed) and equilibrium spike index ($\alpha = 7/4$, dashed-dotted) are also shown.

Figure 18: Evolution of a halo with an adiabatically grown BH (green) in comparison to a BH without growth, i.e., with the initial halo following a NFW profile (blue). For better clarity, initial profiles for energy and density are shown in black. Halo parameters are `test1_old` from table 2. Lighter shadings indicate later times. After about 190 years both initial conditions yield the same result.

4.4. Varying the velocity-dependence of the cross-section

In the previous sections, the velocity-dependence β of the cross-section was fixed at a constant value of four, i.e., $\sigma \propto v^{-4}$.
In this section, β is varied and the resulting spike index is compared to the expected equilibrium solutions (table 1).
For velocity-dependencies of the cross-section with $\beta = 0, 1, 2, 3, 4, 5, 6$, the expected slope indices are $\alpha = 3/4, 4/4, 5/4, 6/4, 7/4, 8/4, 9/4$, respectively.
Figure 19a shows the resulting slope indices of the halos at late times. All simulation start with a spiked NFW profile with an initial slope index close to the CDM slope, $\alpha = 7/3$. Once the evolution sets in and the equilibrium is reached at the center, the resulting profiles show a good agreement with the theoretical predictions.
For the three lowest velocity-dependencies ($\beta = 0, 1, 2$), the simulation have not yet reached $t = 10$Gyr. [29] Despite this, a partial convergence towards the expected solutions ($\alpha = 3/4, 4/4, 5/4$) is still observed. For $\beta = 2$, the halo has only relaxed in the inner region, causing the slope index to increase with radius in the intermediate region of the halo. For $\beta = 3, 4, 5$ the slope indices follow similar profiles in the outer regions but diverge at the point where the halo transitions to the BH dominated regime ($r \lesssim 10^{-6}$kpc) to follow the corresponding equilibrium solutions, $\alpha = 6/4, 7/4, 8/4$. The highest velocity-dependence ($\beta = 6$) leads to a gravothermal collapse of the halo by $t \approx 9.4$Gyr. As a result the profile of the slope index shifts to smaller radii and exhibits a much higher value in the outer regions ($10^{-5} - 1$kpc). Despite the collapse, the halo still converges to the equilibrium solution $\alpha = 9/4$ in the inner region.
It is notable that, even though the expected values for α only differ by about 10-20% between adjacent solutions, a clear distinction can be made between all results. This is particularly impressive given that much larger errors were observed (e.g., in fig. 11).
It is important to note that in the very central region ($r < 10^{-12}$kpc), the slope index diverges from the equilibrium solution and the profiles tend towards $\alpha = 3/2$. This is a direct result of the "numerical equilibrium" described in section 3.3.
The most notable feature seen in the density profiles in fig. 19b is the strong increase in the density of the simulation with $\beta = 6$, where the halo is undergoing gravothermal collapse. Compared to other profiles at a similar time, the density is increased by 10 orders of magnitude. For the smallest velocity-dependencies ($\beta = 0, 1, 2$), the halo remains close to the initial NFW profile up to the spike radius ($r \approx 10^{-4}$kpc). At smaller radii, a clear distinction can be made between all profiles, with convergence towards the expected power-law solutions. For $\beta = 3, 4, 5$, a core is visible between 10^{-6}kpc and 1kpc, and the density follows the respective power-law at smaller radii.

The relative error in the slope index, defined as

$$\langle|\Delta\alpha|\rangle/\alpha = \langle|\alpha - \alpha_0|\rangle/\alpha, \tag{65}$$

is shown as a function of time in fig. 19c. Here, α_0 is the analytic equilibrium value obtained

[29] The luminosity for small β grows particularly quickly with smaller radii, leading to increasingly small time steps.

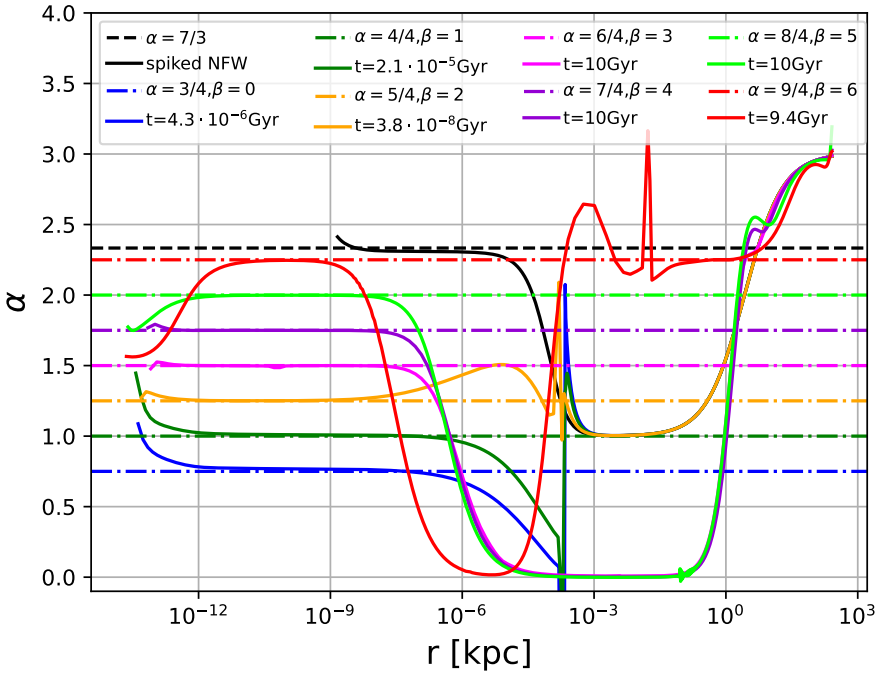

(a) Slope index. Horizontal lines give analytic equilibrium solutions.

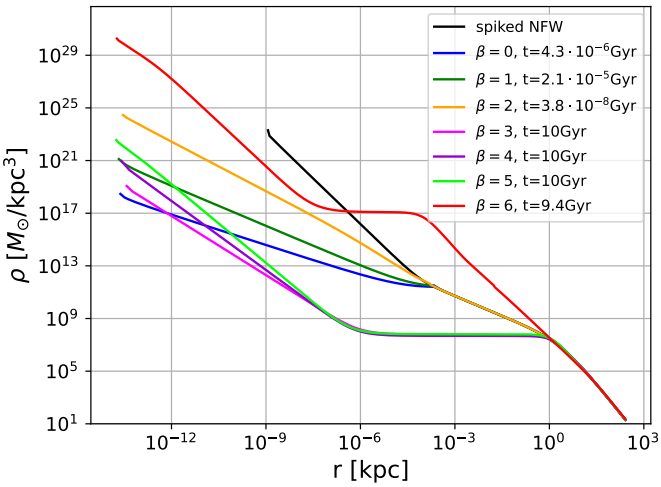

(b) Density profile.

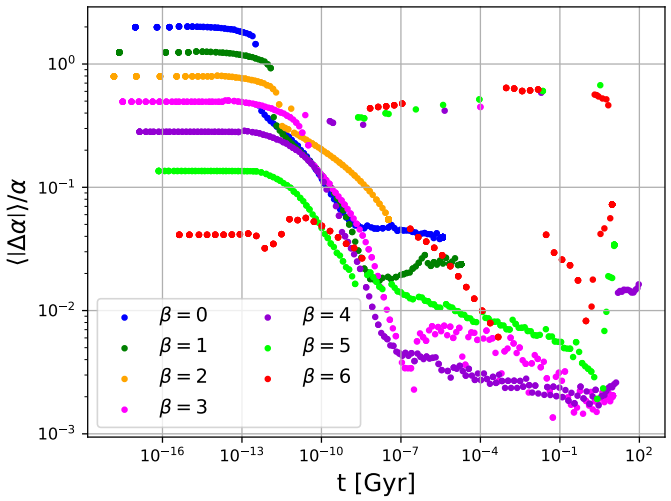

(c) Convergence towards the theoretical solution as a function of time. Initially, $\alpha \approx 7/3$, which leads to different relative errors. In the end, $\Delta\alpha/\alpha \approx 1 - 10\%$.

Figure 19: Based on the run parameters `test1_old` the velocity dependence of the cross-section, β, is varied: $\sigma \propto v^{-\beta}$. Initial spiked NFW profile is given in black. For $\beta = 6$ a collapse of the halo can be seen at 9.4Gyr where the density of the core is strongly increased (red). A convergence to the equilibrium solution can be seen nonetheless.

from section 2.7 and the average is taken within the transition region. [30]
Initially, this relative deviation differs greatly between different choices for β, ranging from a few percent for $\beta = 6$ and nearly 200% for $\beta = 0$. [31] This is because of the difference between the initial slope $\alpha = 7/3$ and the eventual equilibrium value α_0. Nonetheless, the halos reach equilibrium on fairly short timescales ($t < 10^{-10}$Gyr) and after this the relative errors are consistently only a few percent. Some outliers are present where $\langle|\Delta\alpha|\rangle/\alpha$ is in the range around 50%. This is most likely caused either by discontinuities in the profile or a preceding correction step, which can alter the slope index (see fig. 9c).

4.5. Comparison to artificial spiking

In this work, SIDM halos are simulated explicitly with a central BH, allowing the impact on halo evolution to be directly captured. In contrast, the more common approach described in section 3.4, simulated only the SIDM halo and then includes the effects of a central BH on the density by adding a DM spike. The goal of this final section is to investigate whether these two methods yield the same results.
A useful quantity for comparison is the slope index α, which clearly shows the intersection point of both power-laws.
Figure 20a shows the slope index at $t = 0$, after a BH was grown adiabatically (orange). As a comparison, a spiked SIDM halo is shown, with the spike radius chosen in terms of mass (eq. (17), blue dashed) and in terms of internal energy (eq. (18), blue). This yields spike radii of $r_{sp} \approx 0.15$pc and $r_{h,\nu} \approx 0.2$pc, respectively. Although both methods result in a similar spike radius, they overestimate the point of transition ($r_{sp,true}$) when comparing this to the simulated profile. Defining this point at the steepest descent of the slope index [32], I find $r_{sp,true} \approx 0.08$pc.
While both analytic estimates of the spike radius are off by a factor of 2, this is nonetheless an acceptable result as the order of magnitude is correctly determined.
The effect of this is also reflected in the density profile (fig. 20b). The full simulation with the BH yields a lower density than predicted by adding the spike artificially. At $r = 10^{-5}$kpc, the density is $\rho = 8 \cdot 10^{13} M_\odot/\text{kpc}^3$ for the full simulation. In comparison, the added spikes show a density of $\rho = 2 \cdot 10^{14} M_\odot/\text{kpc}^3$ for $r_{sp} = 0.2 r_{h,m}$ and $\rho = 3 \cdot 10^{14} M_\odot/\text{kpc}^3$ for $r_{sp} = r_{h,\nu}$. Again, while the precise values differ, the results of these methods are broadly in the same range.

This changes drastically as the evolution continues.
As time progresses, the internal energy in the inner region increases. Since $v^2 \propto u$, and the mass of the BH remains roughly constant, eq. (18) implies that the radius of influence $r_{h,\nu}$ decreases over time.
Most of the halo evolves similarly to a SIDM-only halo, where the density of the halo generally decreases as a core begins to form. As heat flows inwards during this stage, an

[30] The outer boundary of this region is set by $r_{h,\nu}$ (eq. (18)). To reduce boundary effects, the 10 innermost and outermost grid points are then excluded.
[31] $\alpha_0 = 2.25$ for $\beta = 6 \Rightarrow \langle|\Delta\alpha|\rangle/\alpha \approx 4\%$, whereas $\alpha_0 = 0.75$ for $\beta = 0 \Rightarrow \langle|\Delta\alpha|\rangle/\alpha \approx 200\%$.
[32] This method works well for smooth functions. Numerical errors can make the slope index non-differentiable, which makes it more challenging to use this method.

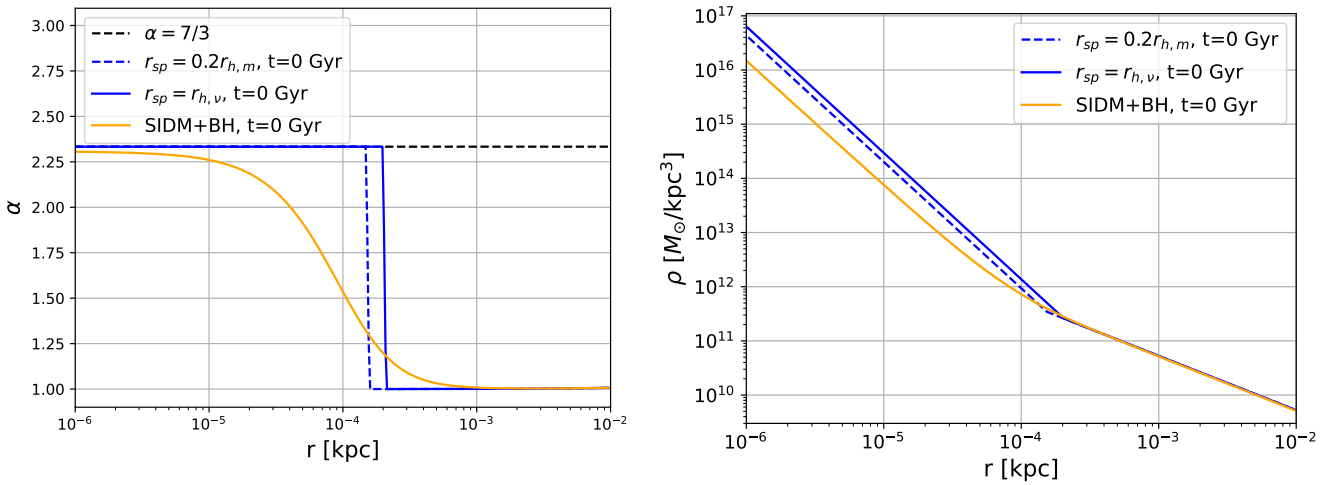

(a) Slope index. Vertical lines indicate the position of the spike radii.

(b) Density

Figure 20: Comparison between a simulation with an explicitly modeled BH (orange), and SIDM-only simulations with added spike ($\alpha = 7/3$) at $r_{h,\nu}$ (blue solid) and at $0.2r_{h,m}$ (blue dashed) at $t = 0$. Initial parameters are `test_old` from table 2.

outward flow of matter is established. Because the $2M_{bh}$ shell lies in this region of the halo, it shifts outwards over time, pulling $r_{h,m}$ along with it. Thus, the spike radius increases over time time.

To determine which of these two expressions more accurately reflects the true spike radius, fig. 21 shows the evolution of the ratio between $r_{sp,true}$ and both of the analytic expressions, for multiple simulations. For simulations based on `test1_old`, only the relevant change is used as the label, e.g., for $\beta = 6$, the label is $\sigma \propto v^{-6}$. For `test1_old_initial_bh`, the initial conditions of the *NFW+BH* halo (section 4.3) are used.

Examining first the ratio $r_{sp,true}/r_{h,\nu}$, the results follow a pattern, with most of the points falling within a range of 0.4-0.8, and no clear distinction between runs is visible (fig. 21a). In contrast, using $r_{h,m}$ from eq. (17) results in poorer match to the actual transition point (fig. 21b). Initially, the ratio stays relatively constant between 0.1 and 0.2, [33] indicating that $r_{h,m}$ may be used as an approximation for the intersection point early on. However, as time progresses (after roughly 10^{-10}Gyr) the halo expands and $r_{h,m}$ increases, causing $r_{sp,true}/r_{h,m}$ to decrease. Once the halo undergoes a gravothermal collapse ($t > 60$Gyr), this ratio increases slightly again. Hence, $r_{sp,true}/r_{h,m}$ is time dependent, and $r_{h,m}$ proves to be a poor measure of the transition region.

Additionally, there is a clear difference between the different models for this choice of the radius of influence. When increasing the BH mass from $100M_\odot$ to $1000M_\odot$ or $10000M_\odot$, $r_{sp,true}/r_{h,m}$ is also increased for larger BH masses. Changing the velocity-dependence of the cross-section also has an influence on the evolution of the ratio - larger β lead to an earlier formation of the core and thus an earlier decrease in the ratio (e.g., compare the profiles for $\sigma \propto v^{-6}$ to $\sigma \propto v^{-3}$).

These results suggest that the position of the intersection point of the power-laws is best

[33] According to [37] this value should be 0.19-0.22.

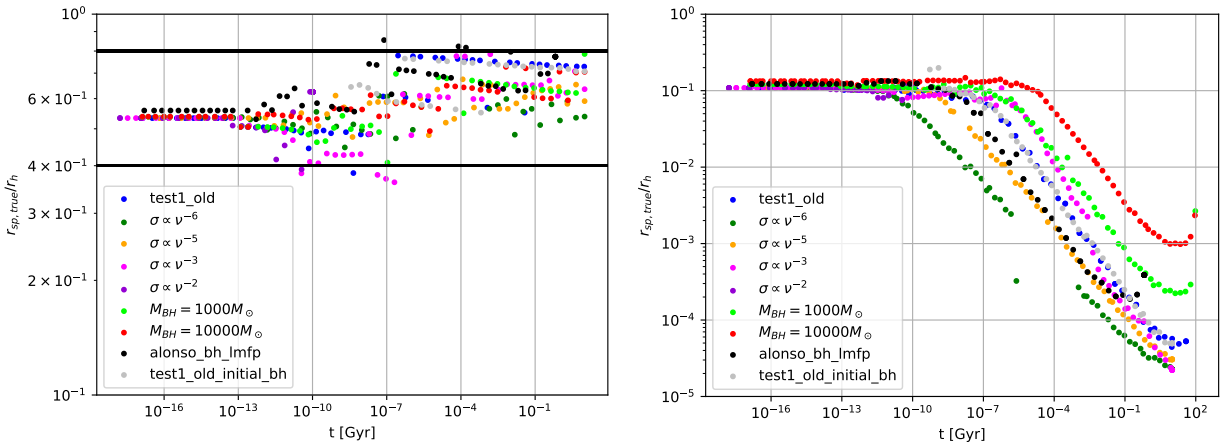

(a) $r_h = r_{h,\nu}$ from eq. (18). Majority of results are in a band between 0.4 and 0.8 (black solid lines), indicating this definition accurately captures the transition between the power-laws.

(b) $r_h = r_{h,m}$ from eq. (17). Ratio decreases over time due to expansion of the halo. At late times ($t \lesssim 60$Gyr) a reverse trend can be seen when the halo collapses. Additionally a distinction between models can be seen, e.g., higher BH masses increase the ratio.

Figure 21: The ratio between the BH radius of influence and the numerically determined intersection point of the two power-laws ($r_{sp,true}$) as a function of time. Simulations based on `test1_old` are labeled by the specific change, e.g., for $\sigma \propto \nu^{-6}$, $\beta = 6$.

captured by the radius of influence when defined in terms of the velocity dispersion as in eq. (18). Therefore, when simulating a SIDM halo without a central BH and later adding a DM spike, using $r_{h,\nu}$ as the spike radius is the optimal approach.

The choice of spike radius has a direct impact on the resulting density profiles. Figure 22 compares both choices of the spike radius ($r_{sp} = r_{h,\nu}$ and $r_{sp} = 0.2 r_{h,m}$) to the full simulation with a central BH (*SIDM+BH*) for $t > 0$.

In all time steps shown, placing the spike radius at $0.2 r_{h,m}$ leads to a gross overestimation of the density (fig. 22a). As predicted, the spike radius increases with time, so that the discrepancy is largest at the last time step shown ($t = 10$Gyr). The density is overestimated by six orders of magnitude and the spike radius by over three orders of magnitude, compared to the full simulation.

On the other hand, setting the spike radius at $r_{h,\nu}$ results in a density profile that very closely follows the result of the full simulation at the center. The largest deviation here occurs at the first time step shown ($t = 1.6 \cdot 10^{-5}$Gyr), where adding the spike results in an overestimation of the density by about 60%. this difference decreases over time, so that at $t = 10$Gyr the difference is only 6% and not visible by eye. This choice of the spike radius also correctly reproduces the transition point in the slope index α (fig. 22b). The other expression of the spike radius, $r_{sp} = 0.2 r_{h,m}$, does not capture this transition accurately, because in this case the spike radius grows over time rather than shrinking.

However, when comparing the halos in an intermediate region, it proves that the SIDM-only halo evolves slightly slower; the density is slightly raised compared to the full simulation.

This difference is most likely caused by the choice of the scale height H, since it influences the luminosity even outside the BH dominated region.

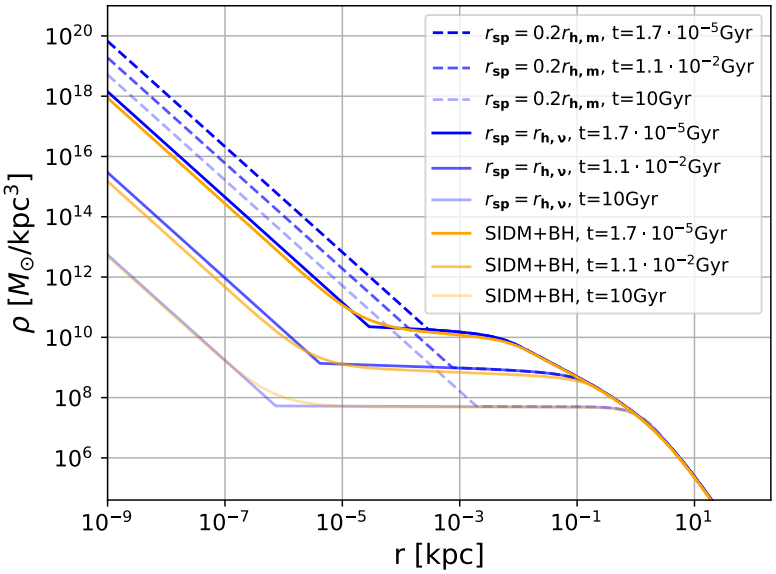

(a) Density

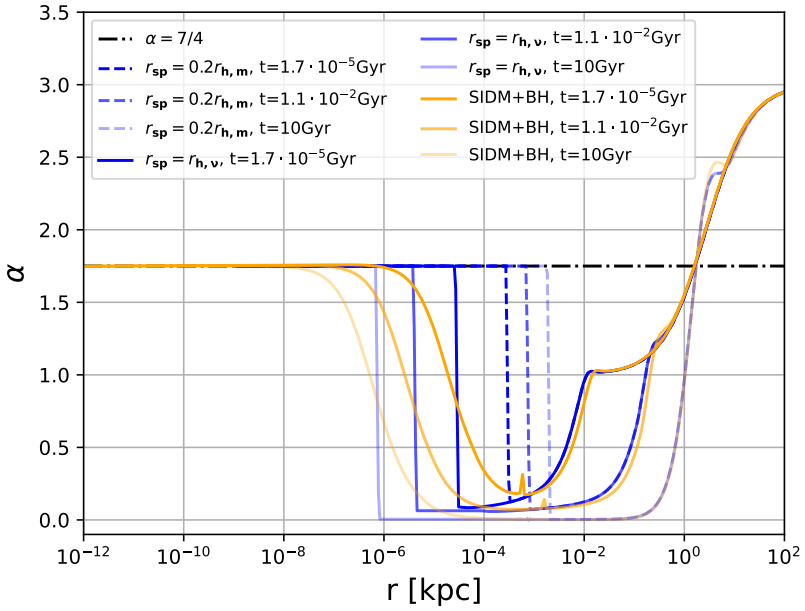

(b) Slope index

Figure 22: Comparison of full simulation with BH (orange), to SIDM only simulation with added spikes ($\alpha = 7/4$) at $r_{h,\nu}$ (blue solid) and at $0.2r_{h,m}$ (blue dashed). Lighter shadings indicate later times. Vertical lines indicate position of the respective spike radii. Initial parameters follow `test_old` from table 2.

5. Conclusion

The goal of this work was to simulate the evolution of a SIDM halo with a central BH using the gravothermal fluid model.
During the implementation, it became evident that the numerical simulation is sensitive to certain purely numerical parameters and the specific approach used to incorporate the added effects of the BH (sections 3.2 and 3.3). These challenges were successfully addressed, and the simulations were shown to reproduce the theoretical results for the DM distribution in equilibrium (fig. 19).
While the modification of the scale height as proposed in [28] seems to be too simplistic at first glance, affecting the luminosity far outside the BH's radius of influence, the resulting deviations disappear during the evolution fig. 16.
Additionally, it was demonstrated that the steady state solution of the halo's density is independent of the initial conditions, provided that the density profile at large radii is identical (fig. 18).
Finally, the commonly used method of adding a DM spike to a SIDM-only simulation was shown to yield a good approximation of the central density obtained from the full simulation (fig. 22). In the intermediate region, slight deviations were observed, likely due to the choice of the scale height. Recognizing that the correct radius of influence of the BH is best described in terms of internal energy rather than mass, I propose that the best agreement with a SIDM-only halo using the Jeans length as the scale height is achieved when the transition of the scale height ($r_J \to r$) occurs around $r_{h,\nu}$.

Despite these successes, there remains much for future work.
The current implementation uses a Newtonian description of gravity. Given that the simulation of the halo extends very close to the BH and particles reach relativistic speeds, a general relativistic description of the system, as studied in [28, 40], is more suited to model the halo.
The accretion model used in this work is very simple; a more sophisticated model for accretion could be introduced and the accretion of DM studied more extensively in future work.
In this work cross-sections with power-law dependencies on the velocity dispersion were studied. Future works could consider more general models (such as studied in [45]), possibly resulting in different equilibrium solutions.
By comparing simulation results with observational data, constraints on the cross-section and velocity-dependence could be derived. Additional interactions, such as inelastic DM scattering [53], could affect the luminosity in a complicated manner, altering both halo evolution and the equilibrium solutions of the halo.
In this work, BHs were either assumed to grow adiabatically or to be present from the beginning. Allowing the BH to grow with time may lead to observable imprints on the evolution of the halo.
A systematic comparison between full simulations and artificially spiked SIDM-only halos would help asses the quality of the approximations commonly used in the literature [51, 52]. Additionally, a comparison to N-body simulations (such as those in [54]) could further consolidate the robustness of the methods employed in this work.

Finally, all effects caused by the presence of baryonic matter in the system were neglected in this work. Baryonic matter can have a large impact on the evolution of DM halos; the presence of a baryonic potential can cause an accelerated core collapse of the DM halo [55] and an outflow of matter from active galactic nuclei can lead to a transfer of energy from baryonic to DM particles resulting in the flattening of a CDM core [56]. Both these effects could drastically alter the DM distribution and lead to different results compared to this work.

A. Full set of hydrostatic equilibrium equations

The full expressions for the terms appearing in the matrix in eq. (52) that is used to solve for hydrostatic equilibrium, with $M_{tot} = M_i + M_{bh}$, $\Delta M_i = M_i - M_{i-1}$ and $s_i = \nu_i^3/\rho_i$, are given below. To reduce floating point errors, these expressions should be factored as much as possible when converted to code.

$$
\begin{aligned}
b_i = \Big(&9M_{tot}\Delta M_{i+1} r_i^2 r_{i+1} - 9M_{tot}\Delta M_{i+1} r_i^2 r_{i-1} + 6M_{tot}\Delta M_{i+1} r_i r_{i+1} r_{i-1} - 6M_{tot}\Delta M_{i+1} r_i r_{i-1}^2 \\
&- 3M_{tot}\Delta M_{i+1} r_{i+1} r_{i-1}^2 + 3M_{tot}\Delta M_{i+1} r_{i-1}^3 - 3M_{tot}\Delta M_i r_i^2 r_{i+1} + 3M_{tot}\Delta M_i r_i^2 r_{i-1} \\
&- 6M_{tot}\Delta M_i r_i r_{i+1}^2 + 6M_{tot}\Delta M_i r_i r_{i+1} r_{i-1} - 3M_{tot}\Delta M_i r_{i+1}^3 + 3M_{tot}\Delta M_i r_{i+1}^2 r_{i-1} \\
&+ 100\Delta M_{i+1}\rho_{i+1}^{\frac{2}{3}} r_i^4 s_{i+1}^{\frac{2}{3}} + 80\Delta M_{i+1}\rho_{i+1}^{\frac{2}{3}} r_i^3 r_{i-1} s_{i+1}^{\frac{2}{3}} - 60\Delta M_{i+1}\rho_{i+1}^{\frac{2}{3}} r_i^2 r_{i-1}^2 s_{i+1}^{\frac{2}{3}} \\
&- 40\Delta M_{i+1}\rho_{i+1}^{\frac{2}{3}} r_i r_{i-1}^3 s_{i+1}^{\frac{2}{3}} + 60\Delta M_i \rho_i^{\frac{2}{3}} r_i^4 s_i^{\frac{2}{3}} + 80\Delta M_i \rho_i^{\frac{2}{3}} r_i^3 r_{i+1} s_i^{\frac{2}{3}} - 20\Delta M_i \rho_i^{\frac{2}{3}} r_i^2 r_{i+1}^2 s_i^{\frac{2}{3}} \\
&- 40\Delta M_i \rho_i^{\frac{2}{3}} r_i r_{i+1}^3 s_i^{\frac{2}{3}} - 24\rho_i^{\frac{5}{3}} r_i^7 s_i^{\frac{2}{3}} - 28\rho_i^{\frac{5}{3}} r_i^6 r_{i+1} s_i^{\frac{2}{3}} - 20\rho_i^{\frac{5}{3}} r_i^6 r_{i-1} s_i^{\frac{2}{3}} + 16\rho_i^{\frac{5}{3}} r_i^5 r_{i+1}^2 s_i^{\frac{2}{3}} \\
&- 24\rho_i^{\frac{5}{3}} r_i^5 r_{i+1} r_{i-1} s_i^{\frac{2}{3}} + 16\rho_i^{\frac{5}{3}} r_i^5 r_{i-1}^2 s_i^{\frac{2}{3}} + 20\rho_i^{\frac{5}{3}} r_i^4 r_{i+1}^3 s_i^{\frac{2}{3}} + 12\rho_i^{\frac{5}{3}} r_i^4 r_{i+1}^2 r_{i-1} s_i^{\frac{2}{3}} \\
&+ 20\rho_i^{\frac{5}{3}} r_i^4 r_{i+1} r_{i-1}^2 s_i^{\frac{2}{3}} + 12\rho_i^{\frac{5}{3}} r_i^4 r_{i-1}^3 s_i^{\frac{2}{3}} + 16\rho_i^{\frac{5}{3}} r_i^3 r_{i+1}^3 r_{i-1} s_i^{\frac{2}{3}} - 8\rho_i^{\frac{5}{3}} r_i^3 r_{i+1}^2 r_{i-1}^2 s_i^{\frac{2}{3}} \\
&+ 16\rho_i^{\frac{5}{3}} r_i^3 r_{i+1} r_{i-1}^3 s_i^{\frac{2}{3}} - 12\rho_i^{\frac{5}{3}} r_i^2 r_{i+1}^3 r_{i-1}^2 s_i^{\frac{2}{3}} - 4\rho_i^{\frac{5}{3}} r_i^2 r_{i+1}^2 r_{i-1}^3 s_i^{\frac{2}{3}} - 8\rho_i^{\frac{5}{3}} r_i r_{i+1}^3 r_{i-1}^3 s_i^{\frac{2}{3}} \\
&+ 24\rho_{i+1}^{\frac{5}{3}} r_i^7 s_{i+1}^{\frac{2}{3}} + 28\rho_{i+1}^{\frac{5}{3}} r_i^6 r_{i+1} s_{i+1}^{\frac{2}{3}} + 20\rho_{i+1}^{\frac{5}{3}} r_i^6 r_{i-1} s_{i+1}^{\frac{2}{3}} - 16\rho_{i+1}^{\frac{5}{3}} r_i^5 r_{i+1}^2 s_{i+1}^{\frac{2}{3}} \\
&+ 24\rho_{i+1}^{\frac{5}{3}} r_i^5 r_{i+1} r_{i-1} s_{i+1}^{\frac{2}{3}} - 16\rho_{i+1}^{\frac{5}{3}} r_i^5 r_{i-1}^2 s_{i+1}^{\frac{2}{3}} - 20\rho_{i+1}^{\frac{5}{3}} r_i^4 r_{i+1}^3 s_{i+1}^{\frac{2}{3}} - 12\rho_{i+1}^{\frac{5}{3}} r_i^4 r_{i+1}^2 r_{i-1} s_{i+1}^{\frac{2}{3}} \\
&- 20\rho_{i+1}^{\frac{5}{3}} r_i^4 r_{i+1} r_{i-1}^2 s_{i+1}^{\frac{2}{3}} - 12\rho_{i+1}^{\frac{5}{3}} r_i^4 r_{i-1}^3 s_{i+1}^{\frac{2}{3}} - 16\rho_{i+1}^{\frac{5}{3}} r_i^3 r_{i+1}^3 r_{i-1} s_{i+1}^{\frac{2}{3}} + 8\rho_{i+1}^{\frac{5}{3}} r_i^3 r_{i+1}^2 r_{i-1}^2 s_{i+1}^{\frac{2}{3}} \\
&- 16\rho_{i+1}^{\frac{5}{3}} r_i^3 r_{i+1} r_{i-1}^3 s_{i+1}^{\frac{2}{3}} + 12\rho_{i+1}^{\frac{5}{3}} r_i^2 r_{i+1}^3 r_{i-1}^2 s_{i+1}^{\frac{2}{3}} + 4\rho_{i+1}^{\frac{5}{3}} r_i^2 r_{i+1}^2 r_{i-1}^3 s_{i+1}^{\frac{2}{3}} \\
&+ 8\rho_{i+1}^{\frac{5}{3}} r_i r_{i+1}^3 r_{i-1}^3 s_{i+1}^{\frac{2}{3}}\Big)
\end{aligned}
\tag{A.1}
$$

$$
\begin{aligned}
c_i = \Big(&3M_{tot}\Delta M_{i+1}r_i^3 + 3M_{tot}\Delta M_{i+1}r_i^2 r_{i-1} - 3M_{tot}\Delta M_{i+1}r_i r_{i-1}^2 - 3M_{tot}\Delta M_{i+1}r_{i-1}^3 \\
&- 3M_{tot}\Delta M_i r_i^3 - 12M_{tot}\Delta M_i r_i^2 r_{i+1} + 9M_{tot}\Delta M_i r_i^2 r_{i-1} + 9M_{tot}\Delta M_i r_i r_{i+1}^2 \\
&- 6M_{tot}\Delta M_i r_i r_{i+1} r_{i-1} + 18M_{tot}\Delta M_i r_{i+1}^3 - 15M_{tot}\Delta M_i r_{i+1}^2 r_{i-1} + 60\Delta M_i \rho_i^{\frac{2}{3}} r_i^4 s_i^{\frac{2}{3}} \\
&- 40\Delta M_i \rho_i^{\frac{2}{3}} r_i^3 r_{i+1} s_i^{\frac{2}{3}} - 100\Delta M_i \rho_i^{\frac{2}{3}} r_i^2 r_{i+1}^2 s_i^{\frac{2}{3}} - 12\rho_i^{\frac{5}{3}} r_i^7 s_i^{\frac{2}{3}} + 8\rho_i^{\frac{5}{3}} r_i^6 r_{i+1} s_i^{\frac{2}{3}} - 12\rho_i^{\frac{5}{3}} r_i^6 r_{i-1} s_i^{\frac{2}{3}} \\
&+ 20\rho_i^{\frac{5}{3}} r_i^5 r_{i+1}^2 s_i^{\frac{2}{3}} + 8\rho_i^{\frac{5}{3}} r_i^5 r_{i+1} r_{i-1} s_i^{\frac{2}{3}} + 12\rho_i^{\frac{5}{3}} r_i^5 r_{i-1}^2 s_i^{\frac{2}{3}} + 20\rho_i^{\frac{5}{3}} r_i^4 r_{i+1}^2 r_{i-1} s_i^{\frac{2}{3}} - 8\rho_i^{\frac{5}{3}} r_i^4 r_{i+1} r_{i-1}^2 s_i^{\frac{2}{3}} \\
&+ 12\rho_i^{\frac{5}{3}} r_i^4 r_{i-1}^3 s_i^{\frac{2}{3}} - 20\rho_i^{\frac{5}{3}} r_i^3 r_{i+1}^2 r_{i-1}^2 s_i^{\frac{2}{3}} - 8\rho_i^{\frac{5}{3}} r_i^3 r_{i+1} r_{i-1}^3 s_i^{\frac{2}{3}} - 20\rho_i^{\frac{5}{3}} r_i^2 r_{i+1}^2 r_{i-1}^3 s_i^{\frac{2}{3}} \\
&+ 12\rho_{i+1}^{\frac{5}{3}} r_i^7 s_{i+1}^{\frac{2}{3}} - 8\rho_{i+1}^{\frac{5}{3}} r_i^6 r_{i+1} s_{i+1}^{\frac{2}{3}} + 12\rho_{i+1}^{\frac{5}{3}} r_i^6 r_{i-1} s_{i+1}^{\frac{2}{3}} - 20\rho_{i+1}^{\frac{5}{3}} r_i^5 r_{i+1}^2 s_{i+1}^{\frac{2}{3}} \\
&- 8\rho_{i+1}^{\frac{5}{3}} r_i^5 r_{i+1} r_{i-1} s_{i+1}^{\frac{2}{3}} - 12\rho_{i+1}^{\frac{5}{3}} r_i^5 r_{i-1}^2 s_{i+1}^{\frac{2}{3}} - 20\rho_{i+1}^{\frac{5}{3}} r_i^4 r_{i+1}^2 r_{i-1} s_{i+1}^{\frac{2}{3}} + 8\rho_{i+1}^{\frac{5}{3}} r_i^4 r_{i+1} r_{i-1}^2 s_{i+1}^{\frac{2}{3}} \\
&- 12\rho_{i+1}^{\frac{5}{3}} r_i^4 r_{i-1}^3 s_{i+1}^{\frac{2}{3}} + 20\rho_{i+1}^{\frac{5}{3}} r_i^3 r_{i+1}^2 r_{i-1}^2 s_{i+1}^{\frac{2}{3}} + 8\rho_{i+1}^{\frac{5}{3}} r_i^3 r_{i+1} r_{i-1}^3 s_{i+1}^{\frac{2}{3}} + 20\rho_{i+1}^{\frac{5}{3}} r_i^2 r_{i+1}^2 r_{i-1}^3 s_{i+1}^{\frac{2}{3}}\Big)
\end{aligned}
\tag{A.2}
$$

$$
\begin{aligned}
a_i = \Big(&-3M_{tot}\Delta M_{i+1}r_i^3 + 3M_{tot}\Delta M_{i+1}r_i^2 r_{i+1} - 6M_{tot}\Delta M_{i+1}r_i^2 r_{i-1} - 6M_{tot}\Delta M_{i+1}r_i r_{i+1} r_{i-1} \\
&+ 9M_{tot}\Delta M_{i+1}r_i r_{i-1}^2 - 9M_{tot}\Delta M_{i+1}r_{i+1} r_{i-1}^2 + 12M_{tot}\Delta M_{i+1}r_{i-1}^3 + 3M_{tot}\Delta M_i r_i^3 \\
&+ 3M_{tot}\Delta M_i r_i^2 r_{i+1} - 3M_{tot}\Delta M_i r_i r_{i+1}^2 - 3M_{tot}\Delta M_i r_{i+1}^3 + 20\Delta M_{i+1}\rho_{i+1}^{\frac{2}{3}} r_i^4 s_{i+1}^{\frac{2}{3}} \\
&- 40\Delta M_{i+1}\rho_{i+1}^{\frac{2}{3}} r_i^3 r_{i-1} s_{i+1}^{\frac{2}{3}} - 60\Delta M_{i+1}\rho_{i+1}^{\frac{2}{3}} r_i^2 r_{i-1}^2 s_{i+1}^{\frac{2}{3}} - 4\rho_i^{\frac{5}{3}} r_i^7 s_i^{\frac{2}{3}} - 4\rho_i^{\frac{5}{3}} r_i^6 r_{i+1} s_i^{\frac{2}{3}} \\
&+ 8\rho_i^{\frac{5}{3}} r_i^6 r_{i-1} s_i^{\frac{2}{3}} + 4\rho_i^{\frac{5}{3}} r_i^5 r_{i+1}^2 s_i^{\frac{2}{3}} + 8\rho_i^{\frac{5}{3}} r_i^5 r_{i+1} r_{i-1} s_i^{\frac{2}{3}} + 12\rho_i^{\frac{5}{3}} r_i^5 r_{i-1}^2 s_i^{\frac{2}{3}} + 4\rho_i^{\frac{5}{3}} r_i^4 r_{i+1}^3 s_i^{\frac{2}{3}} \\
&- 8\rho_i^{\frac{5}{3}} r_i^4 r_{i+1}^2 r_{i-1} s_i^{\frac{2}{3}} + 12\rho_i^{\frac{5}{3}} r_i^4 r_{i+1} r_{i-1}^2 s_i^{\frac{2}{3}} - 8\rho_i^{\frac{5}{3}} r_i^3 r_{i+1}^3 r_{i-1} s_i^{\frac{2}{3}} - 12\rho_i^{\frac{5}{3}} r_i^3 r_{i+1}^2 r_{i-1}^2 s_i^{\frac{2}{3}} \\
&- 12\rho_i^{\frac{5}{3}} r_i^2 r_{i+1}^3 r_{i-1}^2 s_i^{\frac{2}{3}} + 4\rho_{i+1}^{\frac{5}{3}} r_i^7 s_{i+1}^{\frac{2}{3}} + 4\rho_{i+1}^{\frac{5}{3}} r_i^6 r_{i+1} s_{i+1}^{\frac{2}{3}} - 8\rho_{i+1}^{\frac{5}{3}} r_i^6 r_{i-1} s_{i+1}^{\frac{2}{3}} \\
&- 4\rho_{i+1}^{\frac{5}{3}} r_i^5 r_{i+1}^2 s_{i+1}^{\frac{2}{3}} - 8\rho_{i+1}^{\frac{5}{3}} r_i^5 r_{i+1} r_{i-1} s_{i+1}^{\frac{2}{3}} - 12\rho_{i+1}^{\frac{5}{3}} r_i^5 r_{i-1}^2 s_{i+1}^{\frac{2}{3}} - 4\rho_{i+1}^{\frac{5}{3}} r_i^4 r_{i+1}^3 s_{i+1}^{\frac{2}{3}} \\
&+ 8\rho_{i+1}^{\frac{5}{3}} r_i^4 r_{i+1}^2 r_{i-1} s_{i+1}^{\frac{2}{3}} - 12\rho_{i+1}^{\frac{5}{3}} r_i^4 r_{i+1} r_{i-1}^2 s_{i+1}^{\frac{2}{3}} + 8\rho_{i+1}^{\frac{5}{3}} r_i^3 r_{i+1}^3 r_{i-1} s_{i+1}^{\frac{2}{3}} \\
&+ 12\rho_{i+1}^{\frac{5}{3}} r_i^3 r_{i+1}^2 r_{i-1}^2 s_{i+1}^{\frac{2}{3}} + 12\rho_{i+1}^{\frac{5}{3}} r_i^2 r_{i+1}^3 r_{i-1}^2 s_{i+1}^{\frac{2}{3}}\Big)
\end{aligned}
\tag{A.3}
$$

$$
\begin{aligned}
d_i = {} & 3M_{tot}\Delta M_{i+1}r_i^3 r_{i+1} - 3M_{tot}\Delta M_{i+1}r_i^3 r_{i-1} + 3M_{tot}\Delta M_{i+1}r_i^2 r_{i+1} r_{i-1} - 3M_{tot}\Delta M_{i+1}r_i^2 r_{i-1}^2 \\
& - 3M_{tot}\Delta M_{i+1}r_i r_{i+1} r_{i-1}^2 + 3M_{tot}\Delta M_{i+1}r_i r_{i-1}^3 - 3M_{tot}\Delta M_{i+1}r_{i+1} r_{i-1}^3 + 3M_{tot}\Delta M_{i+1}r_{i-1}^4 \\
& - 3M_{tot}\Delta M_i r_i^3 r_{i+1} + 3M_{tot}\Delta M_i r_i^3 r_{i-1} - 3M_{tot}\Delta M_i r_i^2 r_{i+1}^2 + 3M_{tot}\Delta M_i r_i^2 r_{i+1} r_{i-1} \\
& + 3M_{tot}\Delta M_i r_i r_{i+1}^3 - 3M_{tot}\Delta M_i r_i r_{i+1}^2 r_{i-1} + 3M_{tot}\Delta M_i r_{i+1}^4 - 3M_{tot}\Delta M_i r_{i+1}^3 r_{i-1} \\
& + 20\Delta M_{i+1}\rho_{i+1}^{\frac{2}{3}} r_i^5 s_{i+1}^{\frac{2}{3}} + 20\Delta M_{i+1}\rho_{i+1}^{\frac{2}{3}} r_i^4 r_{i-1} s_{i+1}^{\frac{2}{3}} - 20\Delta M_{i+1}\rho_{i+1}^{\frac{2}{3}} r_i^3 r_{i-1}^2 s_{i+1}^{\frac{2}{3}} \\
& - 20\Delta M_{i+1}\rho_{i+1}^{\frac{2}{3}} r_i^2 r_{i-1}^3 s_{i+1}^{\frac{2}{3}} + 20\Delta M_i \rho_i^{\frac{2}{3}} r_i^5 s_i^{\frac{2}{3}} + 20\Delta M_i \rho_i^{\frac{2}{3}} r_i^4 r_{i+1} s_i^{\frac{2}{3}} - 20\Delta M_i \rho_i^{\frac{2}{3}} r_i^3 r_{i+1}^2 s_i^{\frac{2}{3}} \\
& - 20\Delta M_i \rho_i^{\frac{2}{3}} r_i^2 r_{i+1}^3 s_i^{\frac{2}{3}} - 4\rho_i^{\frac{5}{3}} r_i^8 s_i^{\frac{2}{3}} - 4\rho_i^{\frac{5}{3}} r_i^7 r_{i+1} s_i^{\frac{2}{3}} - 4\rho_i^{\frac{5}{3}} r_i^7 r_{i-1} s_i^{\frac{2}{3}} + 4\rho_i^{\frac{5}{3}} r_i^6 r_{i+1}^2 s_i^{\frac{2}{3}} \\
& - 4\rho_i^{\frac{5}{3}} r_i^6 r_{i+1} r_{i-1} s_i^{\frac{2}{3}} + 4\rho_i^{\frac{5}{3}} r_i^6 r_{i-1}^2 s_i^{\frac{2}{3}} + 4\rho_i^{\frac{5}{3}} r_i^5 r_{i+1}^3 s_i^{\frac{2}{3}} + 4\rho_i^{\frac{5}{3}} r_i^5 r_{i+1}^2 r_{i-1} s_i^{\frac{2}{3}} \\
& + 4\rho_i^{\frac{5}{3}} r_i^5 r_{i+1} r_{i-1}^2 s_i^{\frac{2}{3}} + 4\rho_i^{\frac{5}{3}} r_i^5 r_{i-1}^3 s_i^{\frac{2}{3}} + 4\rho_i^{\frac{5}{3}} r_i^4 r_{i+1}^3 r_{i-1} s_i^{\frac{2}{3}} - 4\rho_i^{\frac{5}{3}} r_i^4 r_{i+1}^2 r_{i-1}^2 s_i^{\frac{2}{3}} \\
& + 4\rho_i^{\frac{5}{3}} r_i^4 r_{i+1} r_{i-1}^3 s_i^{\frac{2}{3}} - 4\rho_i^{\frac{5}{3}} r_i^3 r_{i+1}^3 r_{i-1}^2 s_i^{\frac{2}{3}} - 4\rho_i^{\frac{5}{3}} r_i^3 r_{i+1}^2 r_{i-1}^3 s_i^{\frac{2}{3}} - 4\rho_i^{\frac{5}{3}} r_i^2 r_{i+1}^3 r_{i-1}^3 s_i^{\frac{2}{3}} \\
& + 4\rho_{i+1}^{\frac{5}{3}} r_i^8 s_{i+1}^{\frac{2}{3}} + 4\rho_{i+1}^{\frac{5}{3}} r_i^7 r_{i+1} s_{i+1}^{\frac{2}{3}} + 4\rho_{i+1}^{\frac{5}{3}} r_i^7 r_{i-1} s_{i+1}^{\frac{2}{3}} - 4\rho_{i+1}^{\frac{5}{3}} r_i^6 r_{i+1}^2 s_{i+1}^{\frac{2}{3}} \\
& + 4\rho_{i+1}^{\frac{5}{3}} r_i^6 r_{i+1} r_{i-1} s_{i+1}^{\frac{2}{3}} - 4\rho_{i+1}^{\frac{5}{3}} r_i^6 r_{i-1}^2 s_{i+1}^{\frac{2}{3}} - 4\rho_{i+1}^{\frac{5}{3}} r_i^5 r_{i+1}^3 s_{i+1}^{\frac{2}{3}} - 4\rho_{i+1}^{\frac{5}{3}} r_i^5 r_{i+1}^2 r_{i-1} s_{i+1}^{\frac{2}{3}} \\
& - 4\rho_{i+1}^{\frac{5}{3}} r_i^5 r_{i+1} r_{i-1}^2 s_{i+1}^{\frac{2}{3}} - 4\rho_{i+1}^{\frac{5}{3}} r_i^5 r_{i-1}^3 s_{i+1}^{\frac{2}{3}} - 4\rho_{i+1}^{\frac{5}{3}} r_i^4 r_{i+1}^3 r_{i-1} s_{i+1}^{\frac{2}{3}} + 4\rho_{i+1}^{\frac{5}{3}} r_i^4 r_{i+1}^2 r_{i-1}^2 s_{i+1}^{\frac{2}{3}} \\
& - 4\rho_{i+1}^{\frac{5}{3}} r_i^4 r_{i+1} r_{i-1}^3 s_{i+1}^{\frac{2}{3}} + 4\rho_{i+1}^{\frac{5}{3}} r_i^3 r_{i+1}^3 r_{i-1}^2 s_{i+1}^{\frac{2}{3}} + 4\rho_{i+1}^{\frac{5}{3}} r_i^3 r_{i+1}^2 r_{i-1}^3 s_{i+1}^{\frac{2}{3}} + 4\rho_{i+1}^{\frac{5}{3}} r_i^2 r_{i+1}^3 r_{i-1}^3 s_{i+1}^{\frac{2}{3}}
\end{aligned}
\tag{A.4}
$$

References

[1] F. Zwicky. Die Rotverschiebung von extragalaktischen Nebeln. *Helvetica Physica Acta*, 6:110–127, January 1933.

[2] Ewa L. Lokas and Gary A. Mamon. Dark matter distribution in the coma cluster from galaxy kinematics: breaking the mass-anisotropy degeneracy. *Monthly Notices of the Royal Astronomical Society*, 343(2):401–412, 08 2003. ISSN 0035-8711. doi: 10.1046/j.1365-8711.2003.06684.x. URL https://doi.org/10.1046/j.1365-8711.2003.06684.x.

[3] Gianfranco Bertone and Dan Hooper. History of dark matter. *Reviews of Modern Physics*, 90(4), October 2018. ISSN 1539-0756. doi: 10.1103/revmodphys.90.045002. URL http://dx.doi.org/10.1103/RevModPhys.90.045002.

[4] Vera C. Rubin and W. Kent Ford, Jr. Rotation of the Andromeda Nebula from a Spectroscopic Survey of Emission Regions. *The Astrophysical Journal*, 159:379, February 1970. doi: 10.1086/150317.

[5] M. Milgrom. A modification of the Newtonian dynamics as a possible alternative to the hidden mass hypothesis. *apj*, 270:365–370, July 1983. doi: 10.1086/161130. URL https://ui.adsabs.harvard.edu/abs/1983ApJ...270..365M.

[6] Stacy S. McGaugh. A tale of two paradigms: the mutual incommensurability of ΛCDM and MOND. *Canadian Journal of Physics*, 93(2):250–259, February 2015. ISSN 1208-6045. doi: 10.1139/cjp-2014-0203. URL http://dx.doi.org/10.1139/cjp-2014-0203.

[7] Austin Joyce, Bhuvnesh Jain, Justin Khoury, and Mark Trodden. Beyond the cosmological standard model. *Physics Reports*, 568:1–98, March 2015. ISSN 0370-1573. doi: 10.1016/j.physrep.2014.12.002. URL http://dx.doi.org/10.1016/j.physrep.2014.12.002.

[8] E. Corbelli and P. Salucci. The extended rotation curve and the dark matter halo of m33. *Monthly Notices of the Royal Astronomical Society*, 311(2):441–447, jan 2000. doi: 10.1046/j.1365-8711.2000.03075.x. URL https://doi.org/10.1046%2Fj.1365-8711.2000.03075.x.

[9] Sean Tulin and Hai-Bo Yu. Dark matter self-interactions and small scale structure. *Physics Reports*, 730:1–57, February 2018. ISSN 0370-1573. doi: 10.1016/j.physrep.2017.11.004. URL http://dx.doi.org/10.1016/j.physrep.2017.11.004.

[10] J. R. Brownstein and J. W. Moffat. The bullet cluster 1e0657-558 evidence shows modified gravity in the absence of dark matter. *Monthly Notices of the Royal Astronomical Society*, 382(1):29–47, 10 2007. ISSN 0035-8711. doi: 10.1111/j.1365-2966.2007.12275.x. URL https://doi.org/10.1111/j.1365-2966.2007.12275.x.

[11] M. Markevitch and D. Clowe. Apod: 2017 january 15 - the matter of the bullet cluster. URL https://apod.nasa.gov/apod/ap170115.html.

[12] Douglas Clowe, Maruš a Bradač, Anthony H. Gonzalez, Maxim Markevitch, Scott W. Randall, Christine Jones, and Dennis Zaritsky. A direct empirical proof of the existence of dark matter. *The Astrophysical Journal*, 648(2):L109–L113, aug 2006. doi: 10.1086/508162. URL https://doi.org/10.1086%2F508162.

[13] L. Perivolaropoulos and F. Skara. Challenges for cdm: An update. *New Astronomy Reviews*, 95:101659, December 2022. ISSN 1387-6473. doi: 10.1016/j.newar.2022.101659. URL http://dx.doi.org/10.1016/j.newar.2022.101659.

[14] T. C. Abbott et al. First cosmology results using type ia supernovae from the dark energy survey: Constraints on cosmological parameters. *The Astrophysical Journal Letters*, 872(2):L30, feb 2019. doi: 10.3847/2041-8213/ab04fa. URL https://dx.doi.org/10.3847/2041-8213/ab04fa.

[15] N. Aghanim et al. Planck 2018 results. *Astronomy & Astrophysics*, 641:A6, sep 2020. doi: 10.1051/0004-6361/201833910. URL https://doi.org/10.1051%2F0004-6361%2F201833910.

[16] Julio F. Navarro, Carlos S. Frenk, and Simon D. M. White. The Structure of Cold Dark Matter Halos. *apj*, 462:563, May 1996. doi: 10.1086/177173. URL https://ui.adsabs.harvard.edu/abs/1996ApJ...462..563N.

[17] Nobuhiro Okabe, Graham P. Smith, Keiichi Umetsu, Masahiro Takada, and Toshifumi Futamase. Locuss: The mass density profile of massive galaxy clusters at z = 0.2. *The Astrophysical Journal Letters*, 769(2):L35, may 2013. doi: 10.1088/2041-8205/769/2/L35. URL https://dx.doi.org/10.1088/2041-8205/769/2/L35.

[18] Se-Heon Oh, Deidre A. Hunter, Elias Brinks, Bruce G. Elmegreen, Andreas Schruba, Fabian Walter, Michael P. Rupen, Lisa M. Young, Caroline E. Simpson, Megan C. Johnson, Kimberly A. Herrmann, Dana Ficut-Vicas, Phil Cigan, Volker Heesen, Trisha Ashley, and Hong-Xin Zhang. High-resolution mass models of dwarf galaxies from little things. *The Astronomical Journal*, 149(6):180, may 2015. doi: 10.1088/0004-6256/149/6/180. URL https://dx.doi.org/10.1088/0004-6256/149/6/180.

[19] Ricardo A. Flores and Joel R. Primack. Observational and theoretical constraints on singular dark matter halos. *The Astrophysical Journal*, 427:L1, May 1994. ISSN 1538-4357. doi: 10.1086/187350. URL http://dx.doi.org/10.1086/187350.

[20] Jun Koda and Paul R. Shapiro. Gravothermal collapse of isolated self-interacting dark matter haloes: N-body simulation versus the fluid model. *Monthly Notices of the Royal Astronomical Society*, 415(2):1125–1137, 07 2011. ISSN 0035-8711. doi: 10.1111/j.1365-2966.2011.18684.x. URL https://doi.org/10.1111/j.1365-2966.2011.18684.x.

[21] Shmuel Balberg, Stuart L. Shapiro, and Shogo Inagaki. Self-interacting dark matter halos and the gravothermal catastrophe. *The Astrophysical Journal*, 568(2):475, apr 2002. doi: 10.1086/339038. URL https://dx.doi.org/10.1086/339038.

[22] Jason Pollack. Supermassive Black Holes from Gravothermal Collapse of Fractional Self-Interacting Dark Matter halos. Bachelor thesis, Princeton U., 2012. URL https://inspirehep.net/literature/1343449.

[23] Manoj Kaplinghat, Sean Tulin, and Hai-Bo Yu. Dark matter halos as particle colliders: Unified solution to small-scale structure puzzles from dwarfs to clusters. *Physical Review Letters*, 116(4), January 2016. ISSN 1079-7114. doi: 10.1103/physrevlett.116.041302. URL http://dx.doi.org/10.1103/PhysRevLett.116.041302.

[24] Moritz Fischer. SIDM constraints. URL https://www.darkium.org/.

[25] John Kormendy and Douglas Richstone. Inward bound,Äîthe search for supermassive black holes in galactic nuclei. *Annual Review of Astronomy and Astrophysics*, 33(1):581–624, 1995. doi: 10.1146/annurev.aa.33.090195.003053. URL https://doi.org/10.1146/annurev.aa.33.090195.003053.

[26] John Kormendy and Luis C. Ho. Coevolution (or not) of supermassive black holes and host galaxies. *Annual Review of Astronomy and Astrophysics*, 51(1):511–653, 2013. doi: 10.1146/annurev-astro-082708-101811. URL https://doi.org/10.1146/annurev-astro-082708-101811.

[27] Paolo Gondolo and Joseph Silk. Dark matter annihilation at the galactic center. *Physical Review Letters*, 83(9):1719–1722, aug 1999. doi: 10.1103/physrevlett.83.1719. URL https://doi.org/10.1103%2Fphysrevlett.83.1719.

[28] Stuart L. Shapiro. Star clusters, self-interacting dark matter halos, and black hole cusps: The fluid conduction model and its extension to general relativity. *Phys. Rev. D*, 98:023021, Jul 2018. doi: 10.1103/PhysRevD.98.023021. URL https://link.aps.org/doi/10.1103/PhysRevD.98.023021.

[29] Mark Vogelsberger, Jesus Zavala, and Abraham Loeb. Subhaloes in self-interacting galactic dark matter haloes: Self-interacting galactic dark matter haloes. *Monthly Notices of the Royal Astronomical Society*, 423(4):3740–3752, May 2012. ISSN 0035-8711. doi: 10.1111/j.1365-2966.2012.21182.x. URL http://dx.doi.org/10.1111/j.1365-2966.2012.21182.x.

[30] Laura Sagunski, Sophia Gad-Nasr, Brian Colquhoun, Andrew Robertson, and Sean Tulin. Velocity-dependent self-interacting dark matter from groups and clusters of galaxies. *Journal of Cosmology and Astroparticle Physics*, 2021(01):024–024, jan 2021. doi: 10.1088/1475-7516/2021/01/024. URL https://doi.org/10.1088%2F1475-7516%2F2021%2F01%2F024.

[31] D. Lynden-Bell and P. P. Eggleton. On the consequences of the gravothermal catas-

trophe. *Monthly Notices of the Royal Astronomical Society*, 191(3):483–498, 07 1980. ISSN 0035-8711. doi: 10.1093/mnras/191.3.483. URL https://doi.org/10.1093/mnras/191.3.483.

[32] Alexander Dreichner. Probing self-interacting dark matter halos around black holes with gravitational waves. Jan 2023. URL https://cloud.itp.uni-frankfurt.de/s/EEtLfgqc78gWQrL.

[33] James Hopwood Jeans. The stability of a spherical nebula. *Philosophical Transactions of the Royal Society of London. Series A, Containing Papers of a Mathematical or Physical Character*, 199(312-320):1–53, Jan 1902. doi: 10.1098/rsta.1902.0012.

[34] Lyman S. Spitzer. *Dynamical Evolution of Globular Clusters*. Princeton University Press, 1987. URL http://www.jstor.org/stable/j.ctt7ztvx4.

[35] Hiroya Nishikawa, Kimberly K. Boddy, and Manoj Kaplinghat. Accelerated core collapse in tidally stripped self-interacting dark matter halos. *Phys. Rev. D*, 101: 063009, Mar 2020. doi: 10.1103/PhysRevD.101.063009. URL https://link.aps.org/doi/10.1103/PhysRevD.101.063009.

[36] Kaushala Bandara, David Crampton, and Luc Simard. A relationship between supermassive black hole mass and the total gravitational mass of the host galaxy. *The Astrophysical Journal*, 704(2):1135, sep 2009. doi: 10.1088/0004-637X/704/2/1135. URL https://dx.doi.org/10.1088/0004-637X/704/2/1135.

[37] David Merritt. Single and binary black holes and their influence on nuclear structure, 2003. URL https://arxiv.org/abs/astro-ph/0301257.

[38] Luciano Rezzolla. *An Introduction to Astrophysical Black Holes and Their Dynamical Production*, pages 1–44. Springer International Publishing, Cham, 2016. ISBN 978-3-319-19416-5. doi: 10.1007/978-3-319-19416-5_1. URL https://doi.org/10.1007/978-3-319-19416-5_1.

[39] Laleh Sadeghian, Francesc Ferrer, and Clifford M. Will. Dark-matter distributions around massive black holes: A general relativistic analysis. *Physical Review D*, 88 (6), September 2013. ISSN 1550-2368. doi: 10.1103/physrevd.88.063522. URL http://dx.doi.org/10.1103/PhysRevD.88.063522.

[40] Stuart L. Shapiro and Vasileios Paschalidis. Self-interacting dark matter cusps around massive black holes. *Physical Review D*, 89(2), jan 2014. doi: 10.1103/physrevd.89.023506. URL https://doi.org/10.1103%2Fphysrevd.89.023506.

[41] Marc Kamionkowski, Kris Sigurdson, and Oren Slone. Numerical evolution of self-gravitating halos of self-interacting dark matter. 2025. URL https://arxiv.org/abs/2506.04334.

[42] Scott W. Randall, Maxim Markevitch, Douglas Clowe, Anthony H. Gonzalez, and

Marusa Bradafç. Constraints on the self,Äêinteraction cross section of dark matter from numerical simulations of the merging galaxy cluster 1e0657,àí56. *The Astrophysical Journal*, 679(2):1173–1180, June 2008. ISSN 1538-4357. doi: 10.1086/587859. URL http://dx.doi.org/10.1086/587859.

[43] Vassily Zakharov, Mikhail Zhukovskiy, Sergey Zakharov, and Mikhail Markov. Electron scattering cross-sections for particle transport modeling in a weakly ionized air plasma. *Mathematica Montisnigri*, 51:96–111, 08 2021. doi: 10.20948/mathmontis-2021-51-7.

[44] Wolfram|Alpha, 2025. URL https://www.wolframalpha.com/input?i=%28radius+milkyway%29%5E2%2Fmass+milkyway+%2A4%2A3.1415. visited on 2025-07-12.

[45] Camila A Correa. Constraining velocity-dependent self-interacting dark matter with the milky way's dwarf spheroidal galaxies. *Monthly Notices of the Royal Astronomical Society*, 503(1):920–937, 02 2021. ISSN 0035-8711. doi: 10.1093/mnras/stab506. URL https://doi.org/10.1093/mnras/stab506.

[46] Jonathan L. Feng, Manoj Kaplinghat, Huitzu Tu, and Hai-Bo Yu. Hidden Charged Dark Matter. *JCAP*, 07:004, 2009. doi: 10.1088/1475-7516/2009/07/004.

[47] Lotty Ackerman, Matthew R. Buckley, Sean M. Carroll, and Marc Kamionkowski. Dark matter and dark radiation. *Physical Review D*, 79(2), January 2009. ISSN 1550-2368. doi: 10.1103/physrevd.79.023519. URL http://dx.doi.org/10.1103/PhysRevD.79.023519.

[48] J. N. Bahcall and R. A. Wolf. Star distribution around a massive black hole in a globular cluster. *The Astrophysical Journal*, 209:214–232, October 1976. doi: 10.1086/154711.

[49] Nadav Joseph Outmezguine, Kimberly K Boddy, Sophia Gad-Nasr, Manoj Kaplinghat, and Laura Sagunski. Universal gravothermal evolution of isolated self-interacting dark matter halos for velocity-dependent cross-sections. *Monthly Notices of the Royal Astronomical Society*, 523(3):4786,Äì4800, June 2023. ISSN 1365-2966. doi: 10.1093/mnras/stad1705. URL http://dx.doi.org/10.1093/mnras/stad1705.

[50] Sophia Gad-Nasr, Kimberly K. Boddy, Manoj Kaplinghat, Nadav Joseph Outmezguine, and Laura Sagunski. On the late-time evolution of velocity-dependent self-interacting dark matter halos, 2023. URL https://arxiv.org/abs/2312.09296.

[51] Gonzalo Alonso-Álvarez, James M. Cline, and Caitlyn Dewar. Self-interacting dark matter solves the final parsec problem of supermassive black hole mergers. *Phys. Rev. Lett.*, 133:021401, Jul 2024. doi: 10.1103/PhysRevLett.133.021401. URL https://link.aps.org/doi/10.1103/PhysRevLett.133.021401.

[52] Gerardo Alvarez and Hai-Bo Yu. Density spikes near black holes in self-interacting dark matter halos and indirect detection constraints. *Physical Review D*, 104(4),

aug 2021. doi: 10.1103/physrevd.104.043013. URL https://doi.org/10.1103%2Fphysrevd.104.043013.

[53] Rouven Essig, Samuel D. McDermott, Hai-Bo Yu, and Yi-Ming Zhong. Constraining dissipative dark matter self-interactions. *Phys. Rev. Lett.*, 123:121102, Sep 2019. doi: 10.1103/PhysRevLett.123.121102. URL https://link.aps.org/doi/10.1103/PhysRevLett.123.121102.

[54] V. M. Sabarish, Marcus Brüggen, Kai Schmidt-Hoberg, and Moritz S. Fischer. Accretion of self-interacting dark matter onto supermassive black holes, 2025. URL https://arxiv.org/abs/2505.14779.

[55] Wei-Xiang Feng, Hai-Bo Yu, and Yi-Ming Zhong. Seeding supermassive black holes with self-interacting dark matter: A unified scenario with baryons. *The Astrophysical Journal Letters*, 914(2):L26, June 2021. ISSN 2041-8213. doi: 10.3847/2041-8213/ac04b0. URL http://dx.doi.org/10.3847/2041-8213/ac04b0.

[56] Andrew Pontzen and Fabio Governato. How supernova feedback turns dark matter cusps into cores. *Monthly Notices of the Royal Astronomical Society*, 421(4):3464–3471, 04 2012. doi: 10.1111/j.1365-2966.2012.20571.x. URL https://doi.org/10.1111%2Fj.1365-2966.2012.20571.x.